

TACKLING RADIO POLARIZATION DATA OF HIGH ENERGY
PULSARS

A DISSERTATION
SUBMITTED TO THE DEPARTMENT OF APPLIED PHYSICS
AND THE COMMITTEE ON GRADUATE STUDIES
OF STANFORD UNIVERSITY
IN PARTIAL FULFILLMENT OF THE REQUIREMENTS
FOR THE DEGREE OF
DOCTOR OF PHILOSOPHY

Helen Alta Craig
July 2015

Abstract

The focus of this thesis is on understanding the pulsar magnetosphere particularly with the exploitation of radio polarization. The rotating vector model (the standard pulsar polarization model) can be modified to estimate emission altitude. However, more realistic treatment of relativistic and sweep-back effects show that such augmentations break down relatively quickly. This break-down is quantified and fitting functions are provided that preserve accuracy to higher altitude. The rotating vector model has proven particularly poor for modeling energetic pulsars. We remedy this by including the effects of orthogonal mode jumps, multiple emission altitudes, open zone growth via y-point lowering, and interstellar scattering. A large number of discrepancies can be understood while retaining the geometric picture. The model is systematically applied to six *Fermi*-detected pulsars (PSR J0023+0923, PSR J1024–0719, PSR J1744–1134, PSR J1057–5226, PSR J1420–6048, and PSR J2124–3358). Several other examples of utilizing polarization modeling to understand pulsar geometry and emission characteristics are also presented. Finally, a bidirectional emission model is applied to the polarization data of PSR J1057–5226 and PSR J1705–1906. Overall, we push the limit of what can be learned from a geometrically based model and emphasize the importance of tying such models to data.

*For my mom who has always been there for me, never judging and always loving.
When I was feeling down, she reminded me very practically, “life’s a bitch”.*

Acknowledgement

This thesis and indeed this degree is an accumulation of a lifetime of work. Physics has been my passion and love for many, many years but I could not have done any of this without the wonderful support of my network of mentors, peers, and family.

First, I would like to thank my undergraduate research mentors Richard Hennig, Richard Scalettar, Tristan Ursell, Linton Corruccini, and Rob Phillips. I truly would never have gone this far without your encouragement.

I would like to acknowledge my community college teachers Gary Emmery, Irene McGary, William Simpson, Kathy Monaghan, Forrest Newman, Timothy Wei, Charlie Bennett, Jim Collins, Michael Maddox, Binh Truong, and Thomas Logan. You gave me the foundations of my education.

I recognize my many friends and homework buddies from undergraduate at the University of California, Davis: Nasim Eibagi, Hilary Brunner, Ingrid Neumann, Alex Spears, Jerome Latona, Matt Clint, Aru Rattanachata, Christopher Varney, Lucy Zuniga, Amara Miller, Mark Triplett, Colin McEnroe, Jim Lin, and Max Shchemelinin. I enjoyed working and studying with all of you.

My professors from the University of California, Davis solidified my understanding of physics and gave me the courage and confidence I needed for graduate school. I thank Manuel Calderon de la Barca Sanchez, Nicholas Curro, Rena Zieve, Daniel Cebra, David Webb, John Rundle, Warren Pickett, Nicholas Curro, and Daniel Ferenc.

I thank my many peers, colleagues, classmates, and roommates who have made my experience at Stanford rich. I acknowledge Victoria Martin, Ruby Lai, Jaehwan Kang, Richard Anantua, Adam Wright, Ondrej Urban, Terry Reyes, Rachel Meyer, Yuanyuan Su, Meredith Trotter, Caitlin O'Brien, Steven Ehlert, Rebecca Hernandez,

Renee Lizcano-Roales, Kruttika Vijay, Ted Sanders, Patrick Kelly, Ariel Mendez, Mollie Jacobs, Kara Scheu, Sofia Izmailov, Karen Tkach, Stacy Lewis, Matt Stadnik, Sasha Brownsberger, Kiel Howe, Rebecca Nie, Phil Marshall, Masha Baryakhtar, Yao-Yuan Mao, Jane Dai, Paul Simeon, Yvonne Kung, Alice Allafort, Jonathan Maltz, Andrew Keller, Nicole Ackerman, Eric Spanton, Ning Bao, Matt Noll, Ryan Hamerly, Yu He, Tony Li, Eric Eason, Georges Ndabashimiye, Mandeep Gill, JJ Lee, Kunal Sahasrabuddhe, Sho Uemura, Tim Kovachy, Menyoung Lee, Gabe Billings, Alex Countryman, Kristi Schneck, Kimmy Wu, Rachel Reddick, Matthew Cahill-Rowley, Doug Applegate, Mike Kozina, Warit Mitthumsiri, Chihway Chang, Max Swiatlowski, Sonya Mollinger, Alexis Charles, and Crystal Bray. I know I am missing others but you have all been wonderful companions over the last several years and I thank you for being in my life.

I thank Song Wang in particular for being my best buddy. Thank you for the many talks over lunch and the many tennis lessons. I thank Kurt Barry for being my best gym buddy.

I would like to recognize my adviser Roger Romani for feedback on my projects and resources. For additional feedback on my thesis, I thank Hongjun An. I would like to acknowledge Peter Michelson and the Vice Provost of Graduate Education for my funding. I would like to thank my committee for their time and expertise: Roger Blandford, Phil Bucksbaum, Stephen Cooper, and Vahe Petrosian.

For my data (and interest in my work) I thank Dick Manchester, Simon Johnston, Matthew Kerr, Peter den Hartog, and Tyrel Johnson.

A very special thank you to my office mates Michael Shaw and Adam van Etten for keeping me entertained and delighted everyday. I acknowledge Kyle Watters for helping me get started on my project in the very beginning.

For keeping the computers up and running I am grateful to Glenn Morris, Stuart Marshall, and SLAC Computing.

For all sorts of other support I thank David Stricker, Christine Aguilar, Ziba Mahdavi, Martha Siegel, Anika Green, and Chris Golde.

Finally, I thank my family for everything else. I thank my mom for always being there when I needed to talk and my sister for being my best friend. I thank my

partner Joshua Lande for his love and support and for the many adventures we have gone on together, big and small.

Contents

Abstract	iv
	v
Acknowledgement	vi
List of Tables	xiii
List of Figures	xiv
1 Roadmap	1
2 Pulsar Anatomy	4
2.1 The Origin of Pulsars and Supernova Remnants	4
2.2 Pulsar Wind Nebula	7
2.3 Pulsar Magnetosphere	8
2.4 Neutron Star and Equation of State	10
2.5 Pulsar Populations and Age	11
3 Introduction: Radio and Pulsars	13
3.1 Polarization	13
3.2 Effects of Interstellar Medium	15
3.3 Beaming Geometry	17
3.4 Rotating Vector Model	19

4 Numerical Models of Pulsar Magnetosphere	21
4.1 Magnetic Field Line Calculation	21
4.1.1 A Point in the Magnetosphere	22
4.1.2 Velocity and Motion of a Charged Particle	23
4.1.3 Projection onto the ζ - ϕ Viewing Plane	24
4.2 Polarization Calculation	24
4.3 Numerical (Geometrically-Based) Modeling in Other Wavelengths . .	26
4.3.1 Pulsar X-Ray Wind Tori Model	26
4.3.2 Pulsar γ -Ray Light Curve Model	28
5 Phenomenological Altitude Limits of RVM	30
5.1 Introduction	30
5.2 Simulation Model Assumptions	33
5.2.1 Estimating $\phi = 0$	34
5.2.2 ‘Fitting’ an RVM curve	36
5.3 Correcting for Bias in the RVM Height Estimates	37
5.4 Height Calculation from Shift in ψ	44
5.5 Pulse Width Dependence on Emission Height	46
5.6 Conclusions; Examples from Literature	47
6 Energetic Pulsars	50
6.1 Introduction	51
6.2 Rotating Vector Model and Beyond	53
6.3 Adding Physical Ingredients	57
6.3.1 Multiple Altitudes	57
6.3.2 Interstellar Scattering	59
6.3.3 Orthogonal Mode Jumps in the Context of Multiple Altitudes and Interstellar Scattering	59
6.4 Fitting Methodology	61
6.4.1 Y-Point Considerations	61
6.5 Application (and Illustration) with Individual Pulsars	63
6.5.1 PSR J0023+0923: Nonorthogonal Jumps with Multiple Altitudes	63

6.5.2	PSR J1024–0719: Kinks with Multiple Altitudes	69
6.5.3	PSR J1057–5226: Y-Point and Finite Altitude	70
6.5.4	PSR J1744–1134: Multiple Altitudes with Single Versus Double Pole	76
6.5.5	PSR J1420–6048: Multiple Altitudes and Interstellar Scattering	78
6.5.6	PSR J2124–3358: A Complex Example	85
6.6	Conclusion	88
7	Characterization	91
7.1	PSR J0248+6021 and PSR J2240+5832: Characterizing Young Pulsars with RVM	92
7.2	PSR J1119–6127: Characterization a High Magnetic Field Pulsar with Single-Altitude Model	96
7.3	PSR J1513–5908: Characterizing a Soft γ -ray Pulsar with Single-Altitude Model	99
7.4	PSR J0737–3039A: Characterizing a Double Pulsar System with Finite-Altitude Model	105
7.5	Population Study: Characterizing Sub-luminous γ -Ray Pulsars Using Polarization	109
7.6	Conclusions	114
8	Inward-Directed Photons	116
8.1	Exploring Inward-Directed Photon Emission Using Radio Polarization Data of PSR J1057–5226	116
8.1.1	Introduction	116
8.1.2	Previous Work with PSR J1057–5226	118
8.1.3	Previous Work in Bidirectional Emission	120
8.1.4	Modeling Data of PSR J1057–5226	122
8.1.5	Combining γ -Ray Fitting with Radio Polarization Model . . .	131
8.1.6	Discussion and Conclusions	136
8.2	Exploring Inward-Directed Photon Emission Using Radio Polarization Data of PSR J1705–1906	140

8.2.1	Past Studies	140
8.2.2	Polarization Analysis	141
9	Outlook and Perspective	146
9.1	Next Steps	146
9.2	Summary of Conclusions	149
	Bibliography	151

List of Tables

6.1	Property Parameters of the Pulsars	53
6.2	Fit Parameters for PSR J0023+0923	63
6.3	Fit Parameters for PSR J1024–0719	68
6.4	Fit Parameters for PSR J1057–5226	72
6.5	Fit Parameters for PSR J1744–1134	74
6.6	Fit Parameters for PSR J1420–6048	83
6.7	Fit Parameters for PSR J2124–3358	85
7.1	Polarization Fit Parameters for PSR J0737 – 3039A	105
8.1	Fit parameters for PSR J1057–5226 (Bidirectional Emission)	125
8.2	Measured Parameters for PSR J1057–5226 (Bidirectional Emission)	129

List of Figures

2.1	Figure of the pulsar anatomy	5
2.2	Typical pulsar wind nebula energy spectrum	8
2.3	Period-period derivative schematic plot	12
3.1	Visualization of Stokes parameters	15
5.1	Pulse phase estimates for $\alpha = 45^\circ$, $\phi(\zeta) = 0$ for two different altitudes, $r = 0.1R_{LC}$ and $r = 0.3R_{LC}$	35
5.2	Altitude limits for effective RVM fits	37
5.3	Maximum useful r_f altitude (color bar) in the (α_f, ζ_f) plane for four assumptions about the pulse intensity beam shape.	40
5.4	Altitude limits for effective RVM fits	42
5.5	Maximum altitude for accurate height estimates (color bar) in the (α_f, ζ_f) plane, after applying Equation 5.5	43
5.6	Altitude limits for effective RVM fits using the shift in ψ	45
5.7	Altitude limits for effective pulse width	46
6.1	Plot of model pulsar intensity and polarization sweep showing the effects of single and multiple altitudes with a small scattering constant	55
6.2	Pulsar magnetic field lines at various viewing angles and a typical model polarization sweep with $\alpha = 145^\circ$	56
6.3	Intensity and polarization data for PSR J0023+0923 overlaid with model	64
6.4	Map of (unreduced) χ^2 for PSR J0023+0923 in the $\alpha-\zeta$ plane	65
6.5	Intensity and polarization data for PSR J1024–0719 overlaid with model	67

6.6	Map of (unreduced) χ^2 for PSR J1024–0719 in the α – ζ plane for Regions A and B	68
6.7	Intensity and polarization data for PSR J1057–5226 overlaid with model	71
6.8	Map of (unreduced) χ^2 for PSR J1057–5226 in the α – ζ plane	73
6.9	Intensity and polarization data for PSR J1744–1134 overlaid with model	75
6.10	Map of (unreduced) χ^2 for PSR J1744–1134 in the α – ζ plane	76
6.11	Intensity and polarization data for PSR J1420–6048 overlaid with model	79
6.12	Contours of the joint (unreduced) χ^2 set to 3σ in the α – ζ plane for modeling of the polarization data in 10 cm and 20 cm of PSR J1420–6048	80
6.13	Map of the joint (unreduced) χ^2 for polarization data in 10 cm and 20 cm of PSR J1420–6048 in the α – ζ plane	81
6.14	X-ray pulsar wind nebula of PSR J1420–6048	83
6.15	Intensity and polarization data for PSR J2124–3358 overlaid with model	86
6.16	Map of (unreduced) χ^2 for PSR J2124–3358 in the α – ζ plane	87
7.1	Phase-aligned γ -ray and radio light curves for PSR J0248+6021 and PSR J2240+5832 obtained with the <i>Fermi</i> Large Area Telescope and the Nançay Radio Telescope	93
7.2	Expanded view of the radio polarization position angle sweep near the peak in radio intensity	94
7.3	Pulsar geometry and emission modeling fit map for PSR J0248+6021 and PSR J2240+5832 in the α – ζ plane	95
7.4	Pulsar geometry and emission modeling fit map for PSR J1119–6127 with the outer gap (left panel) and the two-pole caustic (right panel) models in the α – ζ plane	97
7.5	Light curves and radio polarization of PSR J1119–6127 overlaid with models	98
7.6	Intensity and polarization data for PSR J1513–5908 overlaid with model	100
7.7	Map of χ^2 for PSR J1513–5908 fit to radio polarization in the α – ζ plane	101

7.8	Pulsar geometry and emission modeling fit map of an outer gap model and radio polarization model for PSR J1513–5908 in the α – ζ plane of the pulsar	102
7.9	Radio and γ -ray light curves of PSR J1513–5908 with model light curve for $\alpha = 153^\circ$, $\zeta = 133^\circ$	103
7.10	Polarimetric profile for PSR J0737 – 3039A as observed at 1.4 GHz with the Parkes radio telescope	106
7.11	Map of χ^2 surface of the RVM fit to the radio polarization data (central components) for PSR J0737 – 3039A in the α – ζ plane	107
7.12	Light curves for PSR J0737 – 3039A at the α and ζ angles determined from the radio polarization study	108
7.13	The γ -ray fit map for Vela in the α – ζ plane with radio polarization, X-ray torus, and pulse width constraints	110
7.14	The γ -ray fit map for sub-luminous pulsars with parallax distances in the α – ζ plane with radio polarization and pulse width constraints .	111
7.15	The γ -ray fit map for sub-luminous pulsars without parallax distances in the α – ζ plane with radio polarization and pulse width constraints .	112
8.1	Sketch of a pulsar magnetosphere illustrating the use of inward-directed photon emission to explain unusual polarization of PSR J1057–5226 .	119
8.2	Visualization of the pulsar model at parameters for which χ^2 is minimized assuming a single altitude of bidirectional emission for PSR J1057–5226	123
8.3	Intensity and polarization data for PSR J1057–5226 overlaid with bidirectional model	126
8.4	Map of (unreduced) χ^2 in the α – ζ plane for a three-altitude bidirectional fit to the polarization data of PSR J1057–5226	127
8.5	Map of (unreduced) χ^2 in the α – ζ plane for a three-altitude fit to the polarization data of PSR J1057–5226	128
8.6	Data and best models for γ -ray light curve of PSR J1057–5226 . . .	133
8.7	Data and variable w model for γ -ray light curve of PSR J1057–5226	134

8.8	The χ^2 map in the α - ζ plane for fitting polarization sweep data from PSR J1705–1906 to a model with only outward-directed photon emission from two poles	143
8.9	The χ^2 map in the α - ζ plane for fitting polarization sweep data from PSR J1705–1906 to a model with only outward-directed photon emission from a single pole	144
8.10	The χ^2 map in the α - ζ plane for fitting polarization sweep data from PSR J1705–1906 to a model with bidirectional photons from a single pole	145

Chapter 1

Roadmap

The main theme of this thesis is the study of pulsar polarization. More in depth, we are interested in modeling complex polarization of pulsars which thus far has not been well explained by current models. This model is strongly tied to available data. In general, we cover pulsar physics in the broader context related to the polarization. We will begin by giving an overview of the chapters.

Chapter 2 covers high-level information about pulsars. This is quick overview of our understanding of pulsars. In Section 2.1, we review the origin of pulsars through supernovae explosions and consider the resulting pulsar spin and pulsar magnetic fields. We also naturally talk about the resulting supernova remnant which can sometimes be seen around newer pulsars. In Section 2.2, we describe some general properties of the pulsar wind nebula which will occasionally be visible around pulsars. We discuss the pulsar magnetospheres in Section 2.3. This section is particularly relevant because most of the modeling work later in this thesis is magnetospheric. We consider briefly the neutron star interior in Section 2.4. We review in Section 2.5 the range of populations of pulsars and properties of pulsars based on age.

In Chapter 3, we detail classical modeling of radio pulsars. Section 3.1 covers the basics of polarization and Stokes parameters in general context. Next we define interstellar scattering as it relates to polarization in Section 3.2. Interstellar scattering is important in several contexts and will be examined again in the application of models to data. Sections 3.3 and 3.4 derive the two standard formulas for radio

modeling. Section 3.3 obtains the width of the pulsar conical beam related to the phase width of the radio pulse and Section 3.4 obtains the rotating vector formula for polarization position angle versus phase.

Having discussed the analytically based models, Chapter 4 then describes how to obtain the numerically implemented models which we heavily rely upon in this thesis. Section 4.1 outlines the underlying procedure for calculating the field line structure of the pulsar. Section 4.2 elucidates the derivation of the polarization from the previous calculation. Section 4.3 describes the numerically calculated X-ray torus and γ -ray light curve which are often used in conjunction with the polarization model fitting.

In Chapter 5 we formally report the shortcomings of using the analytical finite-altitude polarization model with corrections for the neutron star motion. Section 5.3 offers correction formulas derived from the numerical calculations for better estimation of the emission height via the shift between the peak light curve intensity and the maximum curvature in the polarization sweep. Sections 5.4 and 5.5 compare two other analytical methods for estimating emission altitude to numerical results.

Chapter 6 essays the difficulty of modeling energetic pulsar radio polarization position angle data. Our model ingredients and fitting methodology are defined and justified in Sections 6.3 and 6.4. In Section 6.5 we apply the model to a number of pulsars, each highlighting a different set of aspects of the model.

In Chapter 7, we illustrate the use of polarization modeling in collaboration with other studies. The individual pulsars are analyzed using the rotating vector model and finite numerical modeling although overall, we are studying much simpler data than that seen in Chapter 6. These applications illustrate the use of polarization in the context of multi-wavelength studies.

We were unable to fully understand the polarization of the pulsar PSR J1057–5226 in Chapter 5. In Chapter 8, we revisit the data of PSR J1057–5226 with an amended model which includes inward-directed photon emission. We also examine the γ -ray emission in connection to this model. We also analyze PSR J1705–1906, another pulsar which has been suggested to have inward-directed photon emission from other studies.

In Chapter 9, we summarize conclusions from previous chapters in Section 9.2.

We also discuss in Section 9.1 further improvements and considerations that can be included in future work as well and past shortcomings.

Chapter 2

Pulsar Anatomy

In this chapter we give a quick and clear overview of pulsars as a whole. Pulsars are rich with science and each dissected part of the pulsar has had entire theses and careers devoted to unraveling its story. Admittedly, the following sections do not give justice to the plethora of research done with pulsars. Further, pulsars are particularly interesting because they are objects of extremes. They probe phases and conditions that can never be reached in a typical laboratory.

2.1 The Origin of Pulsars and Supernova Remnants

A star will eventually collapse under its own gravity once it has exhausted its energy source. If the star is massive enough, such a transition will come about violently in a supernova explosion where most of the mass is expelled in a shell around the position the star once was. This glowing mass is known as a supernova remnant which we can continue to observe for 100 to 1000 years after the initial explosion. The remainder of the star collapses further either into a black hole or a neutron star depending on the original mass of the star. Since most of the angular momentum is conserved, the much smaller, denser neutron star has a very small rotational period. Additionally, magnetic flux is also conserved resulting in large magnetic fields.

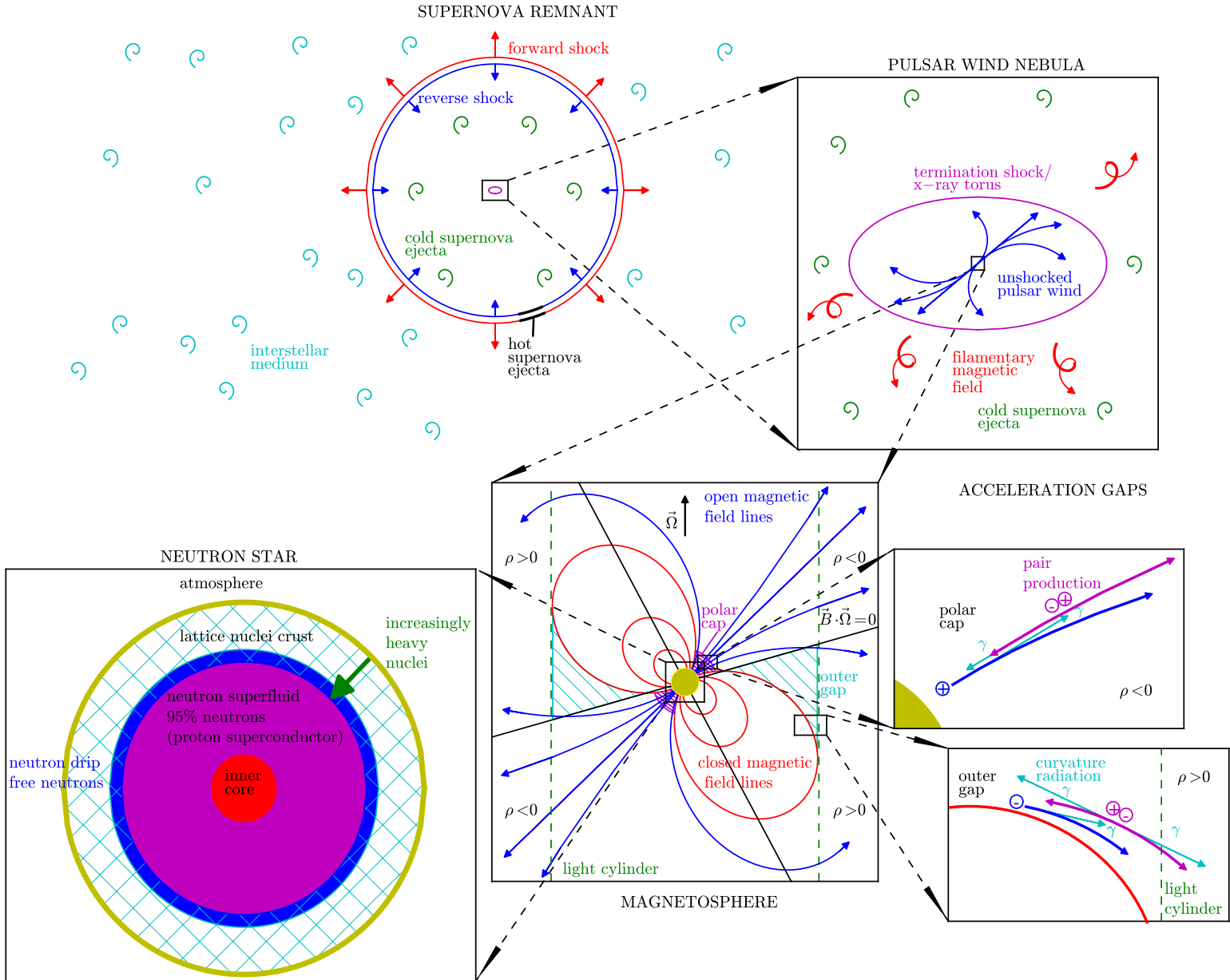


Figure 2.1: Figure of the pulsar anatomy. In Section 2.1 we discuss the supernova remnant and in Section 2.2 we discuss the pulsar wind nebula. In Section 2.3 we explore the basics of the pulsar magnetosphere and review the two acceleration gap locations. We also briefly summarize the neutron star interior in Section 2.4.

For a normal star, the radius R_0 is 10^5 to 10^8 km and the rotational period P_0 is a month to several years. Equations for conservation of angular momentum and magnetic flux are

$$MR_0^2\Omega_0 = MR^2\Omega \quad (2.1)$$

and

$$R_0^2B_0 = R^2B. \quad (2.2)$$

With some physical considerations (e.g. a very small period would result in the star falling apart) it follows that

$$P \sim (R/R_0)^2 P_0 \sim .001 - 1 \text{ seconds} \quad (2.3)$$

and

$$B \sim (R_0/R)^2 B_0 \sim 10^{10} - 10^{12} \text{ Gauss.} \quad (2.4)$$

The rotational period of pulsars range from a couple of milliseconds to several seconds. For instance, PSR J1748 – 2446ad has one of the shortest periods known at 1.395 ms (Hessels et al., 2006). The magnetic fields of pulsars are around 10^{10} to 10^{12} Gauss. Magnetars, neutron stars with extremely strong magnetic fields, are said to have magnetic fields of up to 10^{15} Gauss. (The magnetic field of the Earth is around ~ 0.4 Gauss and the magnetic field of the sun is around ~ 1 Gauss, for reference.)

One of the most massive pulsars is PSR J1311 – 3430 which has a mass of 2.15 to $2.7M_\odot$ (solar mass) from spectroscopic measurements (Romani et al., 2012). But the radius of neutron stars are tiny compared to solar radius at around $1.4 \times 10^{-5}R_\odot = 10$ km. (The circumference is approximately the distance from San Francisco to San Jose.)

Neutron stars were first predicted as a result of supernovae by Baade & Zwicky (1934) many years before they were observed. Although the first supernovae was observed thousands of years ago, the first pulsations (in radio) from pulsars were not observed (or more accurately, *recognized*) until relatively recently in 1967 to 1968. The first correct and complete explanation of pulsars and their connection to neutron

stars followed rapidly by Gold and Pacini (Pacini, 1967; Gold, 1968; Pacini, 1968). Today, the number of radio detected pulsars is in the low thousands and the number of energetic γ -ray detected pulsars is in the low hundreds. The number of galactic neutron stars is estimated at $\sim 10^9$ although how many are actually visible from Earth depends on a number of caveats (Colpi et al., 1998).

2.2 Pulsar Wind Nebula

Unlike supernova remnants, the pulsar wind nebulae are continuously renewed in energy and are visible for much longer than supernova remnants.

Energy from the pulsar rotation is dissipated into the pulsar wind. This dissipated spin down energy is given as

$$\dot{E} = I\Omega\dot{\Omega} \quad (2.5)$$

where I is the moment of inertia of the spinning neutron star and Ω is the angular frequency of the rotation.

The angular frequency and change in the angular frequency are assumed to be related to each other as

$$\dot{\Omega} \propto \Omega^n \quad (2.6)$$

where n is the braking index. Using this relationship, one can solve for the age of the pulsar.

Interaction of this outflow with surrounding medium creates emission. Particles interact with magnetic fields and photons to produce synchrotron (very relativistic and ultra-relativistic electrons gyrating in a magnetic field) and inverse Compton (scattering of low energy photons to high energy by ultra-relativistic electrons) emission. For younger pulsars, this medium includes the cold supernova ejecta beyond the termination shock. Termination shock forms where the ram pressure of the wind balances the pressure of the surrounding medium. Figure 2.2 shows a typical energy spectrum of a pulsar wind nebula.

Of particular interests to polarization and geometric modeling (the main theme of this thesis) is the X-ray torus of pulsar wind nebulae which is further discussed in

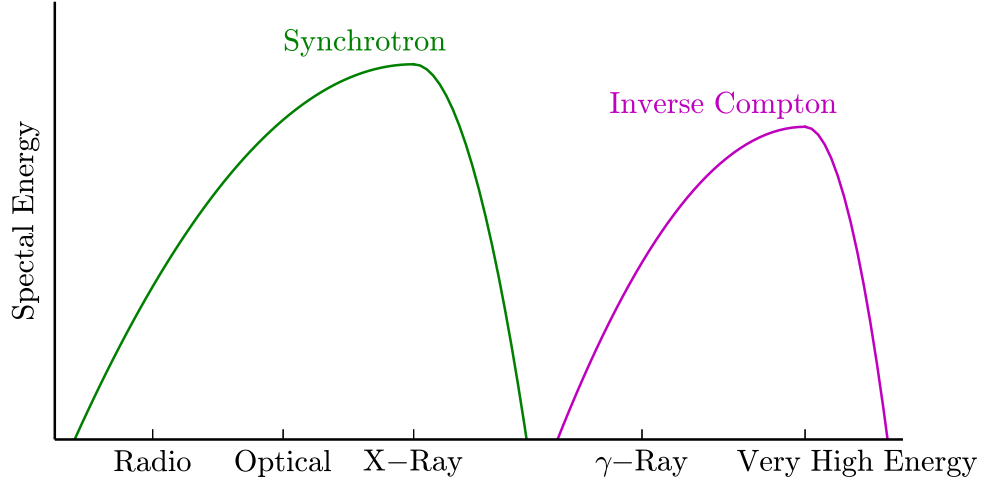


Figure 2.2: Typical pulsar wind nebula energy spectrum. Inspired by Figure 1.1 of Van Etten (2012).

Section 4.3.1. For more detailed overview of pulsar wind nebula see Van Etten (2012) and Gaensler & Slane (2006).

2.3 Pulsar Magnetosphere

The simplest model of the pulsar magnetosphere is a very large magnetic (static) dipole in space. Many of the well-used analytic formulations for analysis of pulsar data are based on this simplistic assumption. We will discuss some of the models in later chapters.

The magnetic field of a *rotating* vacuum dipole are given as

$$\mathbf{B} = -\frac{\mathbf{m}(t_r) + r\dot{\mathbf{m}}(t_r) + r^2\ddot{\mathbf{m}}(t_r)}{r^3} + \left[\frac{3\mathbf{m}(t_r) + 3r\dot{\mathbf{m}}(t_r) + r^2\ddot{\mathbf{m}}(t_r)}{r^3} \cdot \hat{\mathbf{r}} \right] \hat{\mathbf{r}} \quad (2.7)$$

with $\mathbf{m}(t_r) = m [\sin(\alpha) \cos(t_r\omega)\hat{\mathbf{x}} + \sin(\alpha) \sin(t_r\omega)\hat{\mathbf{y}} + \cos(\alpha)\hat{\mathbf{z}}]$ (Kaburaki, 1980). Here retarded time is $t_r = t - r/c$ and m is dipole magnetic moment. This magnetic field contains information about relativistic effects as well as a sweep-back form

from the spin of the neutron star, making it much more realistic than the classical dipole. Conversely, it is much more difficult to use in analytical closed-form formulations without approximations. We use this form of the magnetic field extensively in modeling of both the radio and γ -ray emission in our computational models.

In the pulsar magnetosphere, two primary regions emit photons: the polar gap and the outer gap. The polar gap is located near the magnetic pole of the pulsar and relatively low in the magnetosphere near the surface of the neutron star. Here the magnetic field is the strongest. Emission is produced by curvature radiation. Further, interaction of photons within the strong magnetic field produce electron-position pair that then cause a cascade effect. The polar gap is the classical location of radio emission.

The outer gap is located further out in the magnetosphere in comparison to the polar gap and is also in a wider range of altitudes as it is said to follow particular field lines. The existence of the outer gap is based on the Goldreich-Julian density:

$$\rho = \frac{\nabla \cdot \mathbf{E}}{4\pi} = -\frac{\boldsymbol{\Omega} \cdot \mathbf{B}}{2\pi}. \quad (2.8)$$

The Goldreich-Julian density is formulated from Gauss' Law applied to a force free model:

$$\mathbf{F} = \mathbf{E} + (\boldsymbol{\Omega} \times \mathbf{r}) \times \mathbf{B}/c = 0. \quad (2.9)$$

This density arises from the spin of the neutron star (a spherical electric conductor) in its own magnetic field. Such spinning causes a *nonzero* force but free charges from the neutron star rearrange according to the Goldreich-Julian density to cancel this rotation-induced electromotive force.

The outer gap is located on the outer side of the null charge surface, a cone-like surface originating from the polar cap (and within the region of open field lines). The open field lines are those that extend beyond the pulsar light cylinder never to return to the other magnetic pole. The light cylinder radius, R_{LC} , is the distance from the center of the neutron star at which co-rotating particles would be traveling at the speed of light. The null charge surface is located at $\mathbf{B} \cdot \boldsymbol{\Omega} = 0$ in the magnetosphere. This surface is then defined by the location of the curvature of the magnetic field lines

changing direction in relation to the spin axis but is also the location where $\rho = 0$. One side of the surface is of one charge and the other side of the surface is of the opposite charge.

Further, if the charged particles are located in the region of open field lines, the charged particles are not simply locked in the magnetosphere but can escape along the open field lines out of the magnetosphere and into space. This exodus of charged particles is favorable near the null charge surface because of the proximity of charged particles of opposite sign.

This outflow creates a gap in the charge density (the outer gap) where free charges can accelerate to relativistic energies and emit in the γ -rays. Further, this charge-starved region is the location of cascade processes of pair-production.

Charged particles in the magnetosphere are argued to co-rotate with field lines while traveling along the field lines. In particular, we can note that gyrating motion of the particles around field lines will dissipate quickly through synchrotron radiation. Synchrotron lifetime of electron is $T_s = (5.1 \times 10^8 / B^2) \sqrt{1 - v^2/c^2}$ s, where B is in Gauss (Lyne, 2006). This timescale is much smaller than the travel time of a particle following a field line thus any gyration will be dissipated.

A third gap has been argued to exist that bridges the outer gap region and the polar cap gap and is called the slot gap. This gap is thin and extends from the polar cap to the light cylinder following the last closed field lines. The γ -ray model with emission from this gap is called the two-pole caustic model (Dyks & Rudak, 2003). This model will be mentioned again in Chapter 7 in the work of γ -ray modeling in connection to polarization modeling.

2.4 Neutron Star and Equation of State

The surface of the neutron star is a rigid crystalline surface of iron nuclei. With increasing depth this lattice crust is made up of increasingly heavy nuclei. For a sufficiently large depth, free electrons penetrate the lattice. At further depths, neutrons are free in the lattice in the “neutron drip” region (Kraus, 1986).

Beyond this crust is an outer core made of neutron super-fluid and proton super-conductor. The material is around 95% neutrons. During rotation, the crust and the core can decouple due to slippage, causing star quakes. The quakes are seen as glitches in the pulsar phase data.

The neutron star interior is made up of ultra-dense nuclear material beyond any known substance obtainable in a laboratory. Neutron stars are therefore valuable probes of the fundamental nature of matter. Numerous theoretical equations of state for the stellar core exist in the literature although only one can be the correct and true equation. Accurate measurements of neutron stars with extreme mass are often used to rule out several of these formulations. The exact composition of this inner core is still an area of active research (see e.g. for overviews Becker, 2009).

2.5 Pulsar Populations and Age

As pulsars age, their rotational period slows due to the loss of energy into the pulsar wind. Integration of Equation 2.6 gives the characteristic age of the pulsar as $t = P/2\dot{P}$ where $n = 3$ or equivalently, $P\dot{P}$ is the constant that relates Ω and $\dot{\Omega}$. This relation is based on the assumption that the magnetic field remains constant over time.

Figure 2.3 shows a schematic of various pulsar populations. Most pulsars start their life in the upper left corner of the $P-\dot{P}$ diagram and move diagonally downward along lines of constant magnetic field strength. Eventually, pulsars enter the “death zone” where they are not energetic enough to be observed.

In this thesis work, we focus on young pulsars that are energetic enough to emit in both radio and γ -ray wavelengths, allowing for possible multi-wavelength studies. Another population of pulsars that are energetic enough to emit in the γ -rays are the millisecond pulsars located in lower left corner of Figure 2.3.

While young pulsars are rotation-powered, rotating through the loss of rotational energy, millisecond pulsars are accretion powered. They are “spun up” by their companion star. When the companion star of the neutron star overflows the Roche lobe, it imparts material and angular momentum onto the pulsar. As a result, millisecond

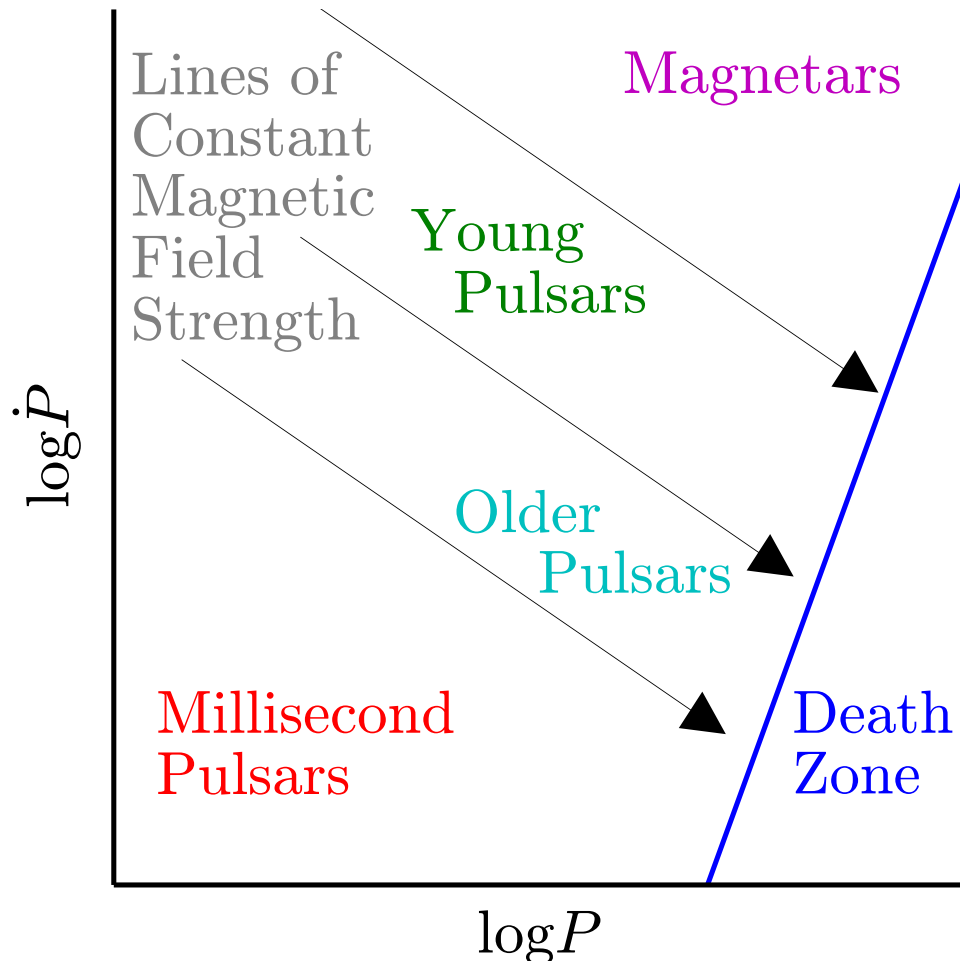


Figure 2.3: Period-period derivative schematic plot.

pulsar periods are much faster and more precise compared to normal pulsar periods.

Chapter 3

Introduction to Radio Wavelength Emission Physics and Modeling of Pulsar Magnetospheres

In this chapter we will explore in more depth the physical models of the pulsar magnetosphere and physical phenomena highly relevant to fully understanding the observed emission. The focus here is on analytic models derived elsewhere and standard to the current understanding of pulsar magnetospheres. We will discuss further the numerical models of pulsars utilized in this thesis in Chapter 4.

3.1 Polarization

William Hiltner and John Hall first observed polarization of starlight in 1949 (Hiltner, 1949; Hall, 1949). Polarization was soon linked to magnetic fields of the galaxy by Leverrett Davis, Jr. and Jesse Greenstein (Davis Jr & Greenstein, 1951).

Pulsars have strong magnetic fields which gives rise to not only their extremely focused beam of emission but also coherent light with defined polarization. Polarization is a means of observing the magnetic field lines of these incredibly small, far away objects. That we can make such a bold measurement speaks to the extremes of the pulsar.

Polarization is most often reported in terms of Stokes parameters, I , Q , U , and V . Stokes parameters are a standard way of representing polarization. At a radio telescope with polarization measurement capabilities, the incoming electromagnetic wave is converted to electric voltage in two independent feeds. Linear feeds will measure polarization aligned along x and y Cartesian coordinates while circular feeds will measure polarization as right-handed or left-handed.

Components of the linear and circular feeds can be converted to Stokes parameters

$$\begin{aligned} I &= \langle E_X^2 \rangle + \langle E_Y^2 \rangle && \text{and } I = \langle E_R^2 \rangle + \langle E_L^2 \rangle, \\ Q &= \langle E_X^2 \rangle - \langle E_Y^2 \rangle && \text{and } Q = 2\langle E_R^2 E_L^2 \cos(\kappa_{RL}) \rangle, \\ U &= 2\langle E_R^2 E_L^2 \cos(\kappa_{XY}) \rangle && \text{and } U = 2\langle E_R^2 E_L^2 \sin(\kappa_{RL}) \rangle, \\ V &= 2\langle E_R^2 E_L^2 \sin(\kappa_{XY}) \rangle && \text{and } V = \langle E_R^2 \rangle - \langle E_L^2 \rangle, \end{aligned} \quad (3.1)$$

where κ_{AB} is the phase difference. With a little manipulation, we can see that $I^2 = Q^2 + U^2 + V^2$ if the incoming signal is totally polarized. Typically, $(Ip)^2 = Q^2 + U^2 + V^2$, where p is the degree of polarization.

Stokes parameters are a convenient way of expressing polarization and is particularly useful for describing partially polarized light using p . The Stokes parameters occupy the so-called Poincaré sphere of optics where Q , U , and V are the axes and pI is the radius of the sphere (Figure 3.1). The polarization angle (ψ) and linear polarization (L) relate to the polar coordinates of Q and U :

$$|L| = \sqrt{U^2 + Q^2} \quad (3.2)$$

and

$$\psi = \frac{1}{2} \arctan \left(\frac{U}{Q} \right). \quad (3.3)$$

Polarization data that we received from collaborators is in the form of Q , U , V , I versus pulsar rotation period phase and we calculate polarization using Q and U .

Further error bars for the polarization are calculated using the following formula (standard error propagation):

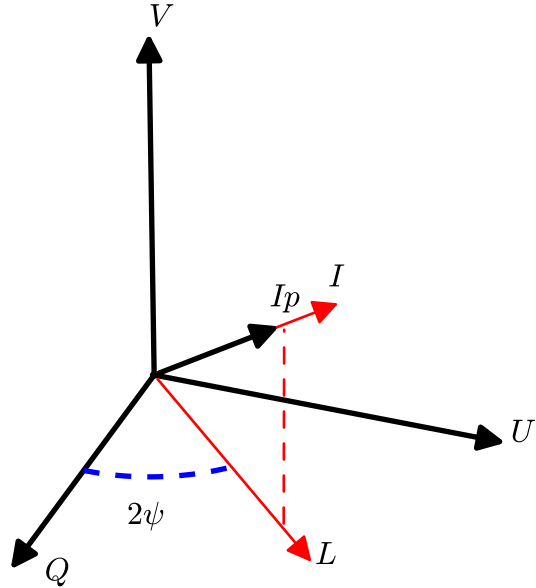


Figure 3.1: Visualization of Stokes parameters. The absolute value of linear polarization ($|L| = \sqrt{U^2 + Q^2}$) occupies the U - Q plane while circular polarization V is the third Cartesian axis. The total polarized intensity is labeled pI and the total intensity which extends beyond the polarized intensity is labeled I .

$$\sigma_\psi(\phi) = \frac{1}{2} \frac{\sqrt{\langle \sigma_{U\text{off}} * Q(\phi) \rangle^2 + \langle \sigma_{Q\text{off}} * U(\phi) \rangle^2}}{\langle Q(\phi) \rangle^2 + \langle U(\phi) \rangle^2}. \quad (3.4)$$

The values $\sigma_{Q\text{off}}$ and $\sigma_{U\text{off}}$ are the standard deviation in the off-pulse phases of Q and U . Note that Q , U , and σ_ψ are all functions of the pulsar rotation period phase, ϕ .

3.2 Effects of Interstellar Medium

The space between us and pulsars is not empty but is full of ionized medium that effects electromagnetic waves. Such medium modifies the signal in several ways which we can quantify.

The dispersion measure is the total density of free electrons ($N(l)$) over the intervening space that the signal from the pulsar travels:

$$DM = \int_0^L N(l)dl. \quad (3.5)$$

The dispersion measure is related to the frequency of the emission (ν) and the time delay of the emission (t):

$$DM_{[\text{cm}^{-3}\text{pc}]} = 2.410 \times 10^{-4} t_{[\text{s}]} \nu_{[\text{MHz}]}^2. \quad (3.6)$$

This formula is useful for calculating the expected time delay between frequencies:

$$\Delta t_{[\text{s}]} = \frac{DM_{[\text{cm}^{-3}\text{pc}]} }{2.410 \times 10^{-4}} \left\{ \frac{1}{\nu_{2[\text{MHz}]}^2} - \frac{1}{\nu_{1[\text{MHz}]}^2} \right\}. \quad (3.7)$$

In particular, we wished to quantify the time delay in PSR J1420–6048 because the fit was simultaneous in two frequencies, 10cm and 20cm (Section 6.5.5). In the end, we found that any time delay due to dispersion was overpowered by our uncertainty in phase. (See Rohlfs & Wilson (2000) for a particularly well formulated presentation of the dispersion measurement calculation.)

Another effect of interstellar medium on measurements is interstellar scattering. The scattering of emission in the medium results in multipath propagation. The effects of interstellar scattering manifest themselves in pulsar data as a broadening of the trailing end of the intensity pulse and a flattening of the polarization data versus phase.

This scattering effect is mathematically described as a convolution of the unscattered Stokes parameters with a scattering kernel:

$$\begin{aligned} I^{\text{scat}} &= \int I(\phi(t'))g(t-t')dt, \\ Q^{\text{scat}} &= \int Q(\phi(t'))g(t-t')dt, \\ U^{\text{scat}} &= \int U(\phi(t'))g(t-t')dt, \\ V^{\text{scat}} &= \int V(\phi(t'))g(t-t')dt. \end{aligned} \quad (3.8)$$

This relation is used for model Q and U in Chapter 6.

Analytical scattering kernels exist assuming various distributions of interstellar medium. The scattering kernel assuming a thin scattering screen halfway between source and observer is given by

$$g_{ts}(t - t') = \begin{cases} 0, & t - t' < 0 \\ e^{-(t-t')/\tau_s}, & t - t' > 0 \end{cases} \quad (3.9)$$

(Williamson, 1972, 1973). The scattering kernel assuming a thick screen near the source is given by

$$g_{ths}(t - t') = \begin{cases} 0, & t - t' < 0 \\ \sqrt{\frac{\pi\tau_s}{4t^3}} e^{-\pi^2\tau_s/16t}, & t - t' > 0. \end{cases} \quad (3.10)$$

The scattering kernel assuming uniform medium is given by

$$g_{um}(t - t') = \begin{cases} 0, & t - t' < 0 \\ \sqrt{\frac{\pi^5\tau_s^3}{8t^5}} e^{-\pi^2\tau_s/4t}, & t - t' > 0. \end{cases} \quad (3.11)$$

The variable τ_s is a characteristic scattering time. The simplest kernel g_{ts} is used in Chapter 6 in modeling scattering.

Finally, pulsar polarization data is Faraday rotated by interstellar medium. Faraday rotation is a powerful tool for probing interstellar scattering but for us it is a nuisance to be removed from the data. The degree of Faraday rotation is related to frequency and can be removed by comparing data from multiple frequencies. Considering that $\Delta\psi$ is often treated as a nuisance parameter, the accuracy of this removal is not very important.

3.3 Beaming Geometry

Assuming a beam of emission centered on the magnetic axis, the relationship between pulse width in phase and the opening angle of the cone structure where emission originates can be derived in closed form. The cone is centered on the magnetic axis defined by

$$\hat{\mathbf{m}} = \cos(\phi) \sin(\alpha) \hat{\mathbf{x}} + \sin(\phi) \sin(\alpha) \hat{\mathbf{y}} + \cos(\alpha) \hat{\mathbf{z}} \quad (3.12)$$

where ϕ is the phase of the pulsar as it rotates about $\hat{\Omega} = \hat{\mathbf{z}}$. The pulse width is W and thus for a symmetric cone, the pulse is seen between $\phi = -W/2$ and $\phi = W/2$ in phase. The angle between $\hat{\mathbf{m}}$ and the line of sight at the maximums ($\phi = -W/2$ and $\phi = W/2$) will also be the opening angle. The line of sight is given by

$$\hat{\mathbf{n}} = \sin \zeta \hat{\mathbf{x}} + \cos \zeta \hat{\mathbf{z}} \quad (3.13)$$

and the relation between opening angle and pulse width is

$$\hat{\mathbf{n}} \cdot \hat{\mathbf{m}} = \cos \Gamma = \sin \zeta \cos W/2 \sin \alpha + \cos \zeta \cos \alpha. \quad (3.14)$$

This equation makes no assumptions about the form of the magnetic field lines. The angle α is between the spin axis and the magnetic axis and the angle ζ is between the spin axis and the line of sight.

We can further relate the pulse width to emission height for a dipole magnetic field. The last closed field lines which define the emission cone for a simple dipole have the form

$$\mathbf{r} = \sin^3 \theta \hat{\mathbf{x}} + \sin^2 \theta \cos \theta \hat{\mathbf{z}} \quad (3.15)$$

and

$$R = |\mathbf{r}| = \sin^2 \theta \quad (3.16)$$

in polar coordinates where R is the emission altitude measured in R_{LC} , light cylinder radius. In this coordinate system, $\hat{\mathbf{m}} = \hat{\mathbf{z}}$.

The angle Γ between $\hat{\mathbf{n}}$ and $\hat{\mathbf{m}}$ will be approximately the angle between

$$\hat{\mathbf{T}} = \frac{d\mathbf{r}/d\theta}{|d\mathbf{r}/d\theta|} \quad (3.17)$$

(the curvature of \mathbf{r}) and $\hat{\mathbf{m}}$. This is actually a far field approximation but is appropriate because the observer is very far from the pulsar.

We can then relate the opening angle to the altitude using Equation 3.15. Again using $\hat{\mathbf{m}} = \hat{\mathbf{z}}$, Equation 3.15 and Equation 3.12:

$$\hat{\mathbf{T}} \cdot \hat{\mathbf{m}} = \frac{2 - 3 \sin^2 \theta}{\sqrt{4 - 3 \sin^2 \theta}}. \quad (3.18)$$

Using $R = \sin^2 \theta$ and approximating R as small,

$$\hat{\mathbf{T}} \cdot \hat{\mathbf{m}} = 1 - 9R/8. \quad (3.19)$$

Further using $\hat{\mathbf{T}} \cdot \hat{\mathbf{m}} \approx \cos \Gamma \approx 1 - \Gamma^2/2$ and Equation 3.14, we get:

$$R = \frac{4}{9} \arccos^2 \left[\sin \zeta \cos \frac{W}{2} \sin \alpha + \cos \zeta \cos \alpha \right]. \quad (3.20)$$

This equation then relates the width of the intensity pulse to the altitude of emission.

3.4 Rotating Vector Model

The rotating vector model (RVM) relates the geometrical angles α (the angle between the spin axis and the magnetic axis) and ζ (the angle between the spin axis and the line of sight) to the polarization position angle ψ for a given phase angle ϕ .

We start with a fixed magnetic axis given by

$$\hat{\mathbf{m}} = \sin \alpha \hat{\mathbf{x}} + \cos \alpha \hat{\mathbf{z}} \quad (3.21)$$

and a viewing direction given by

$$\hat{\mathbf{n}} = \sin \zeta \cos \phi \hat{\mathbf{x}} + \sin \zeta \sin \phi \hat{\mathbf{y}} + \cos \zeta \hat{\mathbf{z}}. \quad (3.22)$$

The polarization angle with respect to $\hat{\mathbf{z}} = \boldsymbol{\Omega}$ is the difference in angle between the projection of $\hat{\mathbf{z}}$ onto the viewing plain and the projection of the vector $\hat{\mathbf{n}} - \hat{\mathbf{m}} / |\hat{\mathbf{n}} - \hat{\mathbf{m}}|$. The viewing plane is defined as orthogonal to $\hat{\mathbf{n}}$. These projections can then be given

by the vector rejections:

$$\mathbf{P}_\Omega = \hat{\mathbf{z}} - (\hat{\mathbf{z}} \cdot \hat{\mathbf{n}})\hat{\mathbf{n}} \quad (3.23)$$

and

$$\mathbf{P}_{m-n} = \frac{\hat{\mathbf{n}} - \hat{\mathbf{m}}}{|\hat{\mathbf{n}} - \hat{\mathbf{m}}|} - \left(\frac{\hat{\mathbf{n}} - \hat{\mathbf{m}}}{|\hat{\mathbf{n}} - \hat{\mathbf{m}}|} \cdot \hat{\mathbf{n}} \right) \hat{\mathbf{n}}. \quad (3.24)$$

The polarization angle can be calculated as

$$\tan \psi = \frac{|\mathbf{P}_{m-n} \times \mathbf{P}_\Omega|}{\mathbf{P}_{m-n} \cdot \mathbf{P}_\Omega}. \quad (3.25)$$

Plugging in the above formulas and simplifying gives us the familiar rotating vector model equation:

$$\tan \psi = \frac{-\sin \alpha \sin \phi}{\cos \alpha \sin \zeta - \cos \phi \cos \zeta \sin \alpha}. \quad (3.26)$$

Chapter 4

Numerical Models of Pulsar Magnetosphere

This chapter focuses on numerically derived pulsar models. We concentrate on the geometrically based modeling of pulsar magnetic field lines. From this formulation, we derive the γ -ray light curves and the radio polarization position angle sweeps. We also discuss the X-ray pulsar wind tori model which is often used in conjunction with the γ -ray and radio modeling.

4.1 Magnetic Field Line Calculation

In this section we discuss how to calculate ζ , the viewing angle, and ϕ , the pulsar phase from a photon at a given point in the magnetosphere of a pulsar with α , the angle between rotation axis and magnetic axis. First we describe the magnetosphere in mathematical terms. Next we calculate the velocity of a charged particle within the magnetosphere which dictates the motion of the particle. Finally, we describe the projection of photons produced by curvature radiation from the charged particles onto the field of view. These photons are the observables from earth.

4.1.1 A Point in the Magnetosphere

In the frame where the magnetic axis is along the z axis, $\theta_B(\phi_B)$ defines the polar cap edge. The polar cap is defined by the last closed field lines on the surface of the pulsar. Field lines originating from within the cap are open and extend beyond the light cylinder never to return to the surface of the pulsar. The light cylinder is the region where co-rotating particles are traveling at the speed of light. The fractional distance from the cap edge is given by the parameter w , where $w = 1$ is the center of the cap at the magnetic pole and $w = 0$ is the edge of the cap. The angle from the magnetic axis is $\theta_w = \theta_B(1 - w)$. A field line traced from the neutron star surface can be defined by a point using the cap parameters:

$$\begin{aligned} x &= \sin(\theta_w) \cos(\phi_B), \\ y &= \sin(\theta_w) \sin(\phi_B), \\ z &= \cos(\theta_w). \end{aligned} \quad (4.1)$$

This point is in the frame where the magnetic axis is along $\hat{\mathbf{z}}$. This point in the frame where the axis of rotation is along $\hat{\mathbf{z}}$ is obtained by applying a rotation matrix as follows:

$$R_y(\alpha) \begin{pmatrix} x \\ y \\ z \end{pmatrix} = \begin{bmatrix} \cos \alpha & 0 & \sin \alpha \\ 0 & 1 & 0 \\ -\sin \alpha & 0 & \cos \alpha \end{bmatrix} \begin{pmatrix} \sin \theta_w \cos \phi_B \\ \sin \theta_w \sin \phi_B \\ \cos \theta_w \end{pmatrix}. \quad (4.2)$$

In the new coordinates the starting point of a given magnetic field line is given by:

$$\begin{aligned} x &= \cos \phi_B \sin \theta_w \cos \alpha + \cos \theta_w \sin \alpha, \\ y &= \sin \phi_B \sin \theta_w, \\ z &= -\cos \phi_B \sin \theta_w \sin \alpha + \cos \theta_w \cos \alpha. \end{aligned} \quad (4.3)$$

This can be translated into the more useful spherical coordinates as follows:

$$\begin{aligned} r &= R_{\text{NS}}, \\ \theta &= \arctan(\sqrt{(x^2 + y^2)/z_w}), \\ \phi &= \arctan(y/x). \end{aligned} \quad (4.4)$$

4.1.2 Velocity and Motion of a Charged Particle

The velocity (\mathbf{v}_{tot}) of a charged particle within the magnetosphere can be calculated in order to obtain the direction of travel. We can calculate the magnetic field strength at this point (r, θ, ϕ) using Equation 2.7. The field at this location points in the direction $\hat{\mathbf{v}}_B$. Charged particles will travel in this direction along the magnetic field. Additionally, the velocity due to co-rotation with the star is given by $\mathbf{v}_t = \langle -y, x, 0 \rangle$.

We need the *magnitude* of \mathbf{v}_B to find $\mathbf{v}_{\text{tot}} = \mathbf{v}_B + \mathbf{v}_t$; only the direction is obtained by Equation 2.7. We estimate $|\mathbf{v}_B + \mathbf{v}_t| = c = 1$ and manipulate this to

$$\mathbf{v}_B^2 + 2\mathbf{v}_B \cdot \mathbf{v}_t + \mathbf{v}_t^2 = 1. \quad (4.5)$$

By simply expanding out, the equation becomes

$$v_B^2 + (\mathbf{v}_t \cdot \hat{\mathbf{v}}_B)^2 + 2\sqrt{v_B^2} \hat{\mathbf{v}}_B \cdot \mathbf{v}_t - (\mathbf{v}_t \cdot \hat{\mathbf{v}}_B)^2 + v_t^2 = 1. \quad (4.6)$$

The above equation can be further manipulated to

$$|\mathbf{v}_B| = -\mathbf{v}_t \cdot \hat{\mathbf{v}}_B + \sqrt{(\mathbf{v}_t \cdot \hat{\mathbf{v}}_B)^2 - v_t^2 + 1} \quad (4.7)$$

thus solving for the magnitude of the velocity on a charged particle from the magnetic field and $\mathbf{v}_{\text{tot}} = \mathbf{v}_B + \mathbf{v}_t$ is obtained.

Further, a charged particle moving along the field line will be located after one

time step at approximately:

$$\begin{aligned}x' &= x + |v_B| \frac{B_x}{\sqrt{B_x^2 + B_y^2 + B_z^2}} \Delta t, \\y' &= y + |v_B| \frac{B_y}{\sqrt{B_x^2 + B_y^2 + B_z^2}} \Delta t, \\z' &= z + |v_B| \frac{B_z}{\sqrt{B_x^2 + B_y^2 + B_z^2}} \Delta t.\end{aligned}\quad (4.8)$$

ignoring higher order terms. We set $\Delta t = 1/2500$ for all calculations.

4.1.3 Projection onto the ζ - ϕ Viewing Plane

The total velocity can be expressed in spherical coordinates, (ϕ_v, θ_v) . This velocity of a charged particle in the magnetosphere is in the same direction as the direction of a photon emitted tangent to the field line at the given point. In order to project this photon onto the plane of the sky, the viewing angle is simply given as $\zeta = \theta_v$.

The phase at which the photon arrives at an observer is given as $\phi = \phi_v + \Delta\phi_{\text{travel-time}}$. The extra piece $\Delta\phi_{\text{travel-time}}$ is needed because photons emitted at different locations in the magnetosphere will arrive at the observer at different times even if they are aimed in the same direction. This change in phase is known as the travel time correction. The phase difference is related to the speed of light and the spin of the pulsar: $\Delta\phi_{\text{travel-time}} = \Omega\Delta t_{\text{travel-time}} = \Omega\Delta d_{\text{travel-time}}/c$. The variable $\Delta d_{\text{travel-time}}$ is then the distance along the line of sight to the observer which is $\Delta d_{\text{travel-time}} = \mathbf{v}_{\text{tot}} \cdot \langle x, y, z \rangle$. Since $\Omega = 1$ and $c = 1$, the phase is simply given as $\phi = \phi_v + \mathbf{v}_{\text{tot}} \cdot \langle x, y, z \rangle$.

4.2 Polarization Calculation

Following a particle along a field line is important for tracking emission from a particular zone on the cap usually expressed as a function of w , the fractional distance between the magnetic pole and the edge of the open-zone cap. It is also important for calculating the polarization position angle (ψ) of a photon emitted at a given location. The position angle is the angle between the spin axis and the acceleration

vector projected onto viewing plane. In order to calculate the position angle of the emission, the acceleration of the particle which emitted the curvature radiation must be calculated. We must calculate the properties of the charged particle one time step forward.

After a time step, the new magnetic field at the new location is \mathbf{B}' (calculated from Equation 2.7). But in the mean time, our reference frame (the pulsar) has rotated by $\Delta\theta$. $\Omega = \Delta\theta/\Delta t = 1$ so $\Delta\theta = 1/25000$ Because of this rotation, the point is actually located at:

$$\begin{pmatrix} x'' \\ y'' \\ z'' \end{pmatrix} = \begin{pmatrix} \cos \Delta\theta & -\sin \Delta\theta & 0 \\ \sin \Delta\theta & \cos \Delta\theta & 0 \\ 0 & 0 & 1 \end{pmatrix} \begin{pmatrix} x' \\ y' \\ z' \end{pmatrix} = \quad (4.9)$$

$$\begin{pmatrix} x' \cos \Delta\theta - y' \sin \Delta\theta \\ x' \sin \Delta\theta - y' \cos \Delta\theta \\ z' \end{pmatrix}. \quad (4.10)$$

Also the magnetic field is now

$$\mathbf{B}'' = \begin{pmatrix} \cos \Delta\theta & -\sin \Delta\theta & 0 \\ \sin \Delta\theta & \cos \Delta\theta & 0 \\ 0 & 0 & 1 \end{pmatrix} \mathbf{B}'. \quad (4.11)$$

Again, the co-rotation velocity is $\mathbf{v}_t'' = -y'', x'', 0$ and the magnitude of the velocity from the magnetic field at this new location is

$$|\mathbf{v}_B''| = -\mathbf{v}_t'' \cdot \hat{\mathbf{v}}_B'' + \sqrt{(\mathbf{v}_B'' \cdot \hat{\mathbf{v}}_B'')^2 - v_t''^2 + 1}. \quad (4.12)$$

As before, we can calculate the total velocity; using this and the previous velocity, we can calculate the acceleration of a particle. The change in the velocity is given by $\Delta t \mathbf{a} = \mathbf{v}_{\text{tot}}'' - \mathbf{v}_{\text{tot}}$.

As stated earlier, the position angle is the angle between the spin axis and the

acceleration vector projected onto a viewing plane. The projection of the acceleration vector onto the viewing plane in the direction of the velocity is given as the vector rejection of \mathbf{a} in direction $\langle v_x, v_y, v_z \rangle$. The vector rejection is given as:

$$\mathbf{p}_a = \mathbf{a} - (\mathbf{a} \cdot \langle v_x, v_y, v_z \rangle) \langle v_x, v_y, v_z \rangle. \quad (4.13)$$

Similarly, the project of $\langle 0, 0, 1 \rangle$, the spin axis Ω , onto viewing plane is given as

$$\mathbf{p}_{001} = \langle 0, 0, 1 \rangle - (\langle 0, 0, 1 \rangle \cdot \langle v_x, v_y, v_z \rangle) \langle v_x, v_y, v_z \rangle = \langle -v_z v_x, -v_z v_y, 1 - v_z v_z \rangle. \quad (4.14)$$

The projection vectors are normalized and the angle between them simply gives the polarization position angle of that photon:

$$\psi = \arccos(\|\mathbf{p}_a\| \cdot \|\mathbf{p}_{001}\|). \quad (4.15)$$

Each position angle is a function of α , ζ , and ϕ . If α and ζ are constant and ψ is plotted versus ϕ , the result is the polarization sweep versus the pulsar phase.

4.3 Numerical (Geometrically-Based) Modeling in Other Wavelengths

Often in studies of pulsar polarization, data in other wavelengths is available and can be used to cross-compare results obtained from modeling of the position angle sweep. In particular, X-ray data of the pulsar wind nebula can be used to derive the viewing angle ζ and modeling of the γ -ray light curve derive independent α and ζ parameters. Here we will briefly describe these relevant models.

4.3.1 Pulsar X-Ray Wind Tori Model

The fitting of the pulsar wind tori model in the X-ray band is described in detail in Ng & Romani (2004) and this section is but a brief overview.

The X-ray pulsar wind nebula is sometimes visible around the central pulsar; the orientation of the pulsar and direction of the spin axis can be quantified using the visible nebula. The boundary of the pulsar wind nebula is marked by the location where the ram pressure of the outflowing material equals the external pressure of the surrounding medium. The radius of this termination shock boundary is

$$r_{\text{termination}} \approx \left(\frac{\dot{E}}{4\pi c P_{\text{ext}}} \right)^{1/2} \quad (4.16)$$

where \dot{E} is the spin down energy and P_{ext} is the external pressure. Ng & Romani (2004) assumed simple equatorial torus with a Gaussian intensity cross section profile to describe the brightness of the nebula tori. The fit parameters for this model are Ψ , the polar axis at a position angle; ζ , the viewing angle measured from the rotation axis; r , the radial distance to the brightest section of the circular tori; δ , a measure of the width of the circular tori; and β , the bulk velocity of the post-shock flow. Additionally, background must also be fit to the image and the point spread function needs to be applied.

The apparent intensity is given as

$$I \propto (1 - \hat{\mathbf{n}} \cdot \beta)^{-(1+\Gamma)} I_0 \quad (4.17)$$

(Pelling et al., 1987) where Γ is the photon spectral index, I_0 is the Synchrotron emission intensity and $\hat{\mathbf{n}}$ is the unit vector along the line of sight. In terms of usable parameters:

$$I(x', y', z') = \frac{N}{(2\pi\delta)^2 r} \times \left(1 - \frac{y' \sin \zeta}{\sqrt{x'^2 + y'^2}} \beta \right)^{-(1+\Gamma)} e^{-[z'^2 + (\sqrt{x'^2 + y'^2} - r)^2]/2\delta^2}. \quad (4.18)$$

The parameters x and y are the coordinates of the CCD frame and z is the line of sight. The parameters x' , y' and z' are the coordinates in the frame of the tori such

that:

$$\begin{aligned} x' &= -x \cos \Psi - y \sin \Psi, \\ y' &= (x \sin \Psi - y \cos \Psi) \cos \zeta + z \sin \zeta, \\ z' &= -(x \sin \Psi - y \cos \Psi) \sin \zeta + z \cos \zeta. \end{aligned} \quad (4.19)$$

The photon spectral index is $\Gamma = 1.5$. For more details and caveats of the model and fitting scheme, see Ng & Romani (2004).

4.3.2 Pulsar γ -Ray Light Curve Model

In Section 4.1 we discussed the formulation necessary to fire photons along magnetic field lines of a rotating pulsar. For modeling in the radio, emission is assumed to come from a single set of magnetic field lines at the same altitude. For modeling in the γ -rays, emission comes from the outer gap region of the magnetosphere as discussed in Section 2.3. Because emission comes from multiple altitudes, caustics, the enveloping of light-rays from multiple locations onto a single location, occur. These caustics give rise to sharp peaks in intensity of the γ -rays.

Similar to Romani & Watters (2010), when modeling γ -ray light curves, we apply a path-length cut-off to the magnetic field lines that are allowed to emit. Only for $s < 2s_{\text{NC},\text{min}} + \rho_{\text{ypt}}$ measured from the center of the pulsar along the arching field line are photons illuminated at full strength. Here s is the path length of the magnetic field line, $s_{\text{NC},\text{min}}$ is the minimum path length of field lines at a given fraction of the polar cap, and ρ_{ypt} is the effective light cylinder radius. Beyond which, illumination is damped according to

$$e^{-[(s-2s_{\text{NC},\text{min}}-\rho_{\text{ypt}})/\sigma_s]^2}. \quad (4.20)$$

This cut-off eliminates field lines that arch over the pulsar and cross the null-charge surface far from the star. These field lines create a secondary gap disjointed from the main gap on the other side of the spin axis that arguably does not exist in most pulsars from a phenomenological stand point; an exception to this argument is the emission from the Crab pulsar (Moffett & Hankins, 1996).

We must also prescribe radiating zones within the outer gap and intensity weightings dependent on the location of the radiating zones. Typically, only field line at

a certain w , the fractional distance from the cap boundary, are considered to emit. The heuristic efficiency law

$$w_0 = \sqrt{10^{-33} \text{ergs}^{-1}/\dot{E}} \quad (4.21)$$

provides an estimation for the choice of w . Theoretical basis for this model is provided in Arons (2006) and observational evidence for this model is provided in Abdo et al. (2010a). A Gaussian spread is applied to the sheet defined by w_0 in the magnetosphere to soften the caustics seen in emission from a single w .

The figure of merit χ_3 defined in Romani & Watters (2010) is often used for analyzing γ -ray light curve data. This minimization formula is given as

$$\chi_3 \propto \sum_i \frac{(M_i - O_i)^2}{O_i} e^{-i/3} \quad (4.22)$$

where i is an index with the value $|M_i - O_i|$ sorted from largest to smallest. Here M_i is the model data point and O_i is the observed data point. Such a scheme will cause models that better match the intensity peaks in the light curve to be favored during minimization of the function.

Chapter 5

Phenomenological Altitude Limits of Rotating Vector Model Fitting

This section is based on work done for “Altitude Limits for Rotating Vector Model Fitting of Pulsar Polarization” (Craig & Romani, 2012)

Traditional pulsar polarization sweep analysis starts from the point dipole rotating vector model (RVM) approximation. If augmented by a measurement of the sweep phase shift, one obtains an estimate of the emission altitude (Blaskiewicz, Cordes, & Wasserman). However, a more realistic treatment of field line sweep-back and finite altitude effects shows that this estimate breaks down at modest altitude $\sim 0.1R_{\text{LC}}$. Such radio emission altitudes turn out to be relevant to the young energetic and millisecond pulsars that dominate the γ -ray population. We quantify the breakdown height as a function of viewing geometry and provide simple fitting formulae that allow observers to correct RVM-based height estimates, preserving reasonable accuracy to $R \sim 0.3R_{\text{LC}}$. We discuss briefly other observables that can check and improve height estimates.

5.1 Introduction

After nearly a half century of pulsar observations, we still do not know the detailed location of the emission zones in the neutron star magnetosphere. However the general

consensus is that the radio emission arises from the ‘open’ field line zone above the magnetic poles at modest altitudes, from a few to a few tens of neutron star radii. In contrast, the γ -ray emission, as measured by *Fermi* (Abdo et al., 2010a), is dominated by high altitudes $> 0.1R_{\text{LC}}$, where the light cylinder radius is $R_{\text{LC}} = cP/2\pi$. Thus the emission zones and light curves for these two bands generally differ. However, recently *Fermi* has detected γ -ray emission from a number of millisecond pulsars where the entire magnetosphere is outside of the neutron star surface $R_{\text{NS}} \approx 0.2/P_{\text{ms}}R_{\text{LC}}$, so that radio emission must be from ‘high altitude’ (Kerr et al., 2012). Further, Karastergiou & Johnston (2007) and Johnston & Weisberg (2006) have found evidence that for young energetic pulsars, the radio emission is dominated by an altitude of ~ 1000 km ($\sim 100R_{\text{NS}}$). This is $\sim 0.2R_{\text{LC}}$ for $P=100$ ms, and it is precisely such young, energetic pulsars which are γ -bright. Thus, if one is interested in γ -emitting pulsars, one must also consider radio emission from an appreciable fraction of the light cylinder radius.

Since the first radio observations, the high linear polarization and rapid position angle sweep of many pulsars at cm wavelength have been used as a clue to the geometry of the emission zone. The foundation for such study is the Radhakrishnan & Cooke (1969) ‘rotating vector model’ (RVM), which follows the sweep of the magnetic field line tangent of a point dipole as projected on the sky. Of course, finite altitude radio emission violates the point source RVM assumption and Blaskiewicz et al. (1991) (hereafter BCW) gave simple approximations for the effects of relativistic aberration at small altitude. In this approximation, the polarization position angle is

$$\psi = \arctan \left[\frac{3r \sin(\zeta) - \sin(\alpha) \sin(\phi + r)}{\sin(\zeta) \cos(\alpha) - \cos(\zeta) \sin(\alpha) \cos(\phi + r)} \right], \quad (5.1)$$

where the inclination angle between rotation axis and magnetic axis is α , the viewing angle is ζ , and the pulse phase is ϕ . The RVM formula is recovered in the limit as the scaled emission height, $r \equiv r_{\text{em}}/R_{\text{LC}}$, goes to zero. Here the principal effect is a lag in the phase of the maximum rate of the polarization sweep $d\psi/d\phi|_{\text{max}}$ of $\Delta\phi \approx 2r$ from the phase of the magnetic axis.

If the absolute position angle of the magnetic axis on the plane of the sky is known (eg. from the position angle of the spin axis), Hirschman & Arons (2001) show that

the observed polarization gives a second height estimate, $\Delta\psi \approx \frac{10}{3}r \cos(\alpha)$, where

$$\psi = \arctan \left[\frac{-\sin(\alpha) \sin(\phi - 2r)}{\sin(\zeta) \cos(\alpha) - \cos(\zeta) \sin(\alpha) \cos(\phi - 2r)} \right] + \Delta\psi \quad (5.2)$$

(Dyks, 2008). In practice it is generally unclear how to measure the magnetic axis polarization angles; most authors treat $\Delta\psi$ as a nuisance parameter.

Of course, both formulae presume knowledge of the phase of closest approach of the magnetic axis $\phi = 0$. The phase of the radio pulse peak is often used, but these pulses can have complex, multi-component morphology. Further, the special relativistic effects shift the intensity peak forward, giving a net observable lag of the polarization sweep from the intensity peak of $\Delta\phi \approx 4r$. The shifts have been clarified and extended to include the effects of field line sweep-back by Dyks & Harding (2004), and Dyks (2008). Nevertheless, observers generally fit to the zero altitude (RVM) limits of the formula to constrain α and ζ and, when possible, estimate the shift of $d\psi/d\phi|_{\max}$ to constrain the altitude, using the linear (BCW) scaling. While this works adequately for many non-recycled pulsars, relatively high altitude emission is inferred for young energetic objects. For millisecond pulsars the basic RVM model often does not fit well.

Thus, recent strong interest in γ -ray emitting pulsars draws our attention to objects where the radio emission may extend to $0.1R_{LC}$ or higher, where the standard RVM treatment is suspect. We seek here to quantify this breakdown: if one applies an RVM/BCW fit and obtains estimates of the magnetic inclination angle α_f , viewing angle ζ_f , and emission height r_f , for what ranges of these parameters are these fits ‘valid’, i.e. when do the fit values and uncertainty ranges include (at some prescribed probability) the real value r_r ? We develop this analysis as a guide to observers wishing to interpret pulsar polarization data and as an indication to situations where detailed fits to numerical models (eg. Parent et al. 2011) are required. In addition, we suggest analytic corrections to allow useful r_f estimates from simple RVM fits to extend to somewhat higher altitude.

5.2 Simulation Model Assumptions

Our approach is to use a specific 3-D magnetosphere model with plausible radio emission zones, to ‘fit’ the resulting light curve and polarization sweep with the point dipole RVM formula and to parametrize the errors. For simplicity the field lines are given by the basic swept-back (retarded) dipole popular in models of high altitude γ -ray emission (Romani & Watters, 2010) and we assume that the radiating particle bunches follow the magnetic field lines. In the spirit of the RVM model, we make a simple geometric construction, projecting the field line tangent at the emission point in the lab frame onto the plane of the sky and assume that the radio emission is polarized parallel to (or perpendicular to) this vector. We do not attempt here to superpose multiple emission heights or to compute intrinsic polarization fractions. Nor do we include other physical effects such as possible cross-field drift of the emitting charge bunches, current-induced departure from the vacuum structure for energetic pulsars (Spitkovsky, 2006) or higher-order multipole/offset dipole effects that may be important in the small magnetospheres of millisecond pulsars (Harding & Muslimov, 2011). While our simple construction ignores these possible effects, we do capture the dominant effect of dipole sweep-back and our computed polarization sweeps pass smoothly to the RVM model curves at low altitude; the other physical effects likely only dominate very close to the light cylinder.

We assume here that the radio emission comes from a single altitude, within the open zone. We then must define the open zone shape and the illumination across it. Of course, there is a formal cap shape for the vacuum retarded dipole solution, where the locus of field lines tangent to the light cylinder trace to a cap on the surface with opening angle $\theta_R(\phi_{\text{cap}})$ varying with azimuth ϕ_{cap} around the magnetic axis. Alternatively, it is common to assume a simple circular cap, with surface angle $\theta_C(\phi_{\text{cap}}) = \text{constant}$. To roughly match the open zone beam sizes at an emission height of $0.1R_{\text{LC}}$ we chose a surface cap angle of $\theta_C = 2^\circ$ for a neutron star of $R_{\text{NS}} = 10^{-3}R_{\text{LC}}$, i.e. a ~ 0.2 s pulsar.

For simplicity and to follow the BCW picture, we illuminate the open zone with

a simple Gaussian profile

$$I \propto e^{(\theta_{\text{cap}}/\theta_0)^2}, \quad \text{with} \quad \theta_0 = 2^\circ / \sqrt{\ln 5} \quad (5.3)$$

so that the intensity falls by $5\times$ at the ‘edge’ of the simple circular cap. The angles are measured at the star surface, although the corresponding radio flux may be emitted at high altitude. We note that there is some evidence that a conal intensity distribution with a patchy illumination may be more typical of many pulsars (Lyne & Manchester, 1988; Karastergiou & Johnston, 2007).

To generate a model polarization sweep we select a magnetic inclination, α_r , and emission height, r_r . We then project the swept-back field lines at this altitude to the plane of sky and record the results on a 2D sky map. Horizontal cuts across this map at a given viewing angle, ζ_r , give the polarization angle sweep, $\psi(\phi)$. We assign ‘measurement’ errors to each value inversely proportional to the pulse flux at its phase. We assume that the observer’s integration achieves a uniform signal-to-noise at pulse maximum, so that the polarization measurement error there is 1° . For pulsars observed far from the magnetic axis at large $|\beta| \equiv |\zeta - \alpha|$ this implies longer integration. As the pulse flux falls toward the edge of the open zone the polarization angle uncertainties increase.

5.2.1 Estimating $\phi = 0$

Use of the simple Gaussian illumination with the pulse phase at the intensity peak (the projected phase of closest approach to the magnetic axis) corresponds to the BCW assumptions. Except for very high altitude emission, where field lines overlap in the sky map and pulse caustics can occur, this gives a simple prescription from which $\phi = 0$ may be estimated via the BCW shift. However, conal emission concentrated to the cap edge significantly complicates the determination of pulse phase. One effect is the variable sweep-back at the leading and trailing edge of the cap. Another is the particular shape of the open zone boundary. We illustrate these effects by marking a ‘peak phase’, the midpoint of the projected open zone boundary, both for a simple circular cap and for the more detailed retarded dipole cap. Figure 5.1 displays the

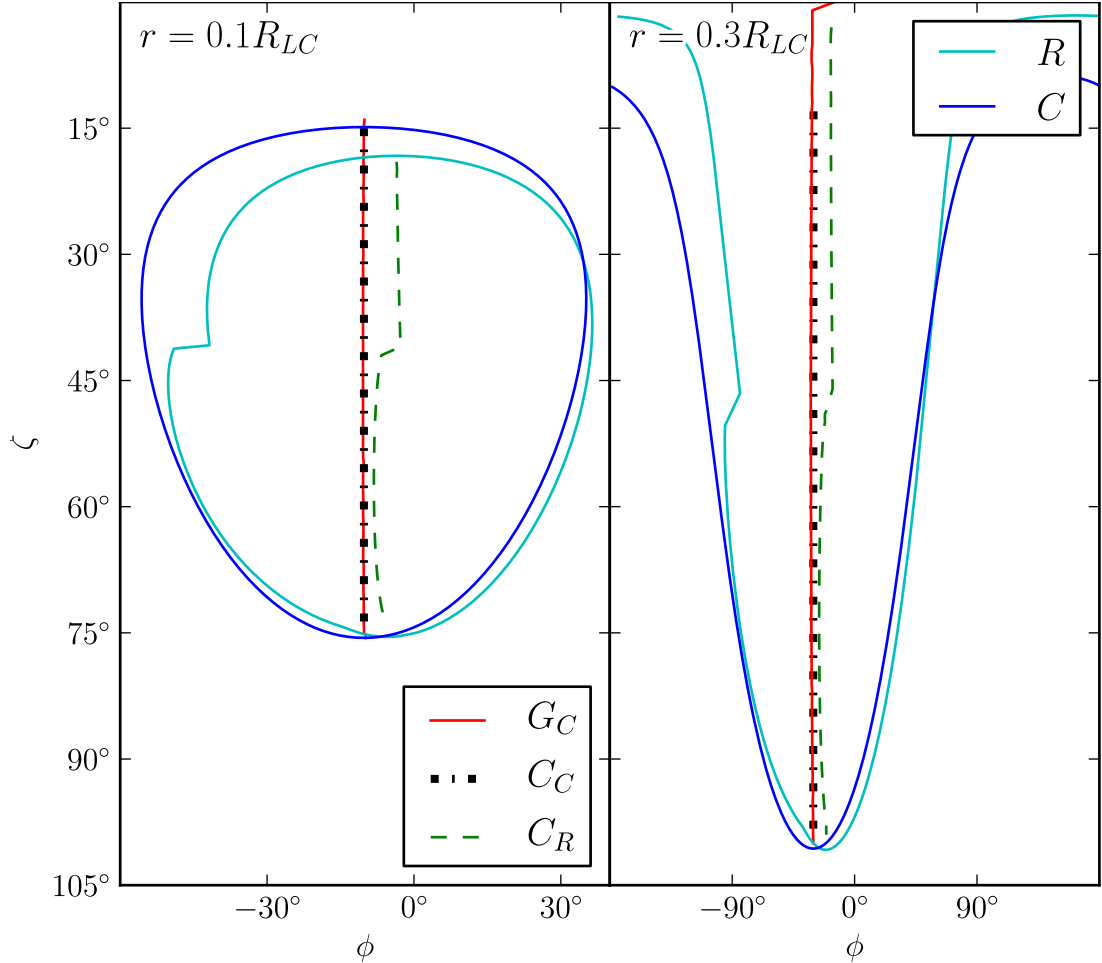


Figure 5.1: Pulse phase estimates for $\alpha = 45^\circ$, $\phi(\zeta) = 0$ for two different altitudes, $r = 0.1R_{LC}$ and $r = 0.3R_{LC}$. G_C : Peak phase from maximum of simple Gaussian intensity weighting. C_C : Peak phase from center of cap edges (circular cap). C_R : Peak phase from center of cap edges (retarded dipole cap).

peak phase shifts for these different definitions.

Not unexpectedly, Figure 5.1 shows that the pulse phase is more sensitive to the details of the open zone geometry for a conal emission zone. The offsets shown there illustrate the effect of the retarded potential field line flaring at high altitude. To this should be added the uncertainties associated with identifying the magnetic axis phase in the presence of patchy conal emission and non-dipole field structure (for

millisecond pulsars). Nevertheless, as we shall show, a substantial fraction of the phase offset is insensitive to the choice of cap center, and can be corrected.

5.2.2 ‘Fitting’ an RVM curve

The retarded dipole field structure increasingly departs from the point dipole as the scaled emission height $r = r_{\text{em}}/R_{\text{LC}}$ approaches unity. Thus if one fits polarization data for a low altitude emitter with the RVM model, the fit parameters α_f , ζ_f , and $r_f = \Delta\phi_f/4$ at the χ^2 minimum will be good approximations to the real values (α_r, ζ_r, r_r) . For modest r_r the RVM fit will absorb the sweep shape departures, (correctably) biasing the parameter estimates, while retaining reasonable χ^2 . At large altitude, the χ^2 will be poor, the parameters will be uncorrectably far from the true values and a fit to a detailed numerical model will be required. The key question is how, with realistic errors σ_{PA} , the unabsorbed distortion grows.

We use our estimated σ_{PA} to construct a ‘ χ^2 ’ weighted departure of the RVM model from the detailed retarded field simulation. This is the weighted systematic error caused by the inability of the RVM model to absorb the detailed shape of the retarded field curve. In a real observation, additional statistical measurement errors would increase ‘ χ^2 ’ above our model value, especially for small r . Any unmodeled physical effects should additionally increase the value of ‘ χ^2 ’ above $\sim 1/(\text{degree of freedom})$ at the minimum. Observers typically adopt the increase $\Delta\chi^2 = \chi^2 - \chi^2_{\text{min}}$ to estimate the confidence intervals on the fit parameters. We are free to do the same here, since our prescription weights appropriately show where the model parameters are most sensitive to the data values. We have confirmed this by fits to a series of Monte Carlo simulations of polarization angle data with added statistical errors, showing that $\Delta\chi^2$ follows the usual distribution for the appropriate numbers of degrees of freedom.

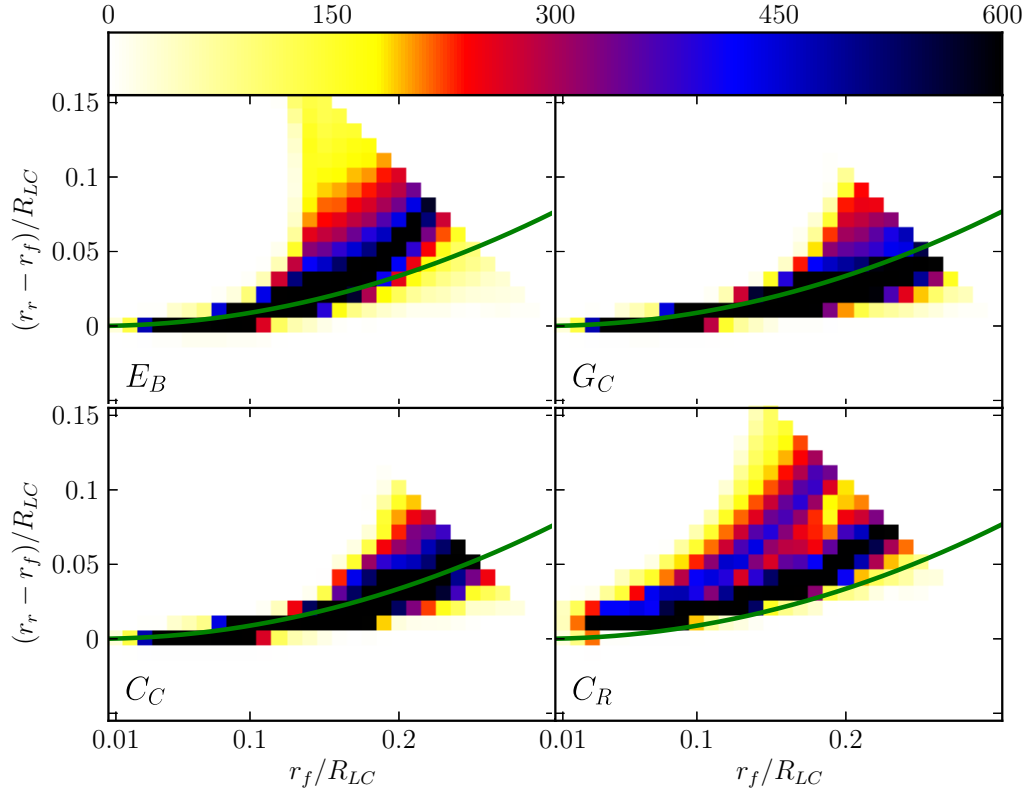


Figure 5.2: Altitude limits for effective RVM fits. Each panel shows the distribution of simulated model fits (color bar) in offset from the true altitude as a function of fit altitude r_f/R_{LC} . The dark band shows the systematic bias in the fit offset. The four panels are for different assumptions about the cap illumination and method of estimating the true phase of $\phi = 0$. E_B : Perfect knowledge of the location of magnetic axis in phase, without the use of an intensity model. G_C : Simple Gaussian intensity peak, $\phi = 0$ inferred from the altitude dependent shift of I_{\max} . C_C : Peak intensity assigned to the center of a double pulse from edges of an open zone circular cap footpoints. C_R : Peak intensity assigned to the center of a double pulse from edges of an open zone above the detailed retarded dipole cap. The green curve shows our estimate of the bias, Equation 5.4.

5.3 Correcting for Bias in the RVM Height Estimates

Our principal goal here is to test the utility of standard RVM fits and to provide a prescription to allow these fits wider applicability for pulsars with high altitude emission.

To do this we compare the RVM fit estimate r_f with the simulated value r_r . Since the mapping is not simple, statements about ranges of validity are perforce statistical. This makes our answers mildly sensitive to the distribution in the underlying pulsar population. Here we assume that our parent pulsar population has isotropically distributed inclination and viewing angles, ie. $\text{Prob}(\alpha) \propto \sin(\alpha)$, $\text{Prob}(\zeta) \propto \sin(\zeta)$ while the altitude is distributed uniformly on $0 \leq r_r \leq 0.3$. Note that we only *observe* a usable polarization sweep if a pulsar produces a minimum number of phase bins (here $\Delta\phi_{\text{obs}} > 0.1$). In turn, this means that our observable pulsar population is biased toward modest $|\beta| = |\alpha - \zeta|$.

We generate a set of pulsar models and apply the RVM fits. This delivers a set of observables $\alpha_f, \zeta_f, r_f; \sigma_{\alpha_f}, \sigma_{\zeta_f}, \sigma_{r_f}$ where the fit values are determined by χ^2 minimum and the error ranges are estimated from the curvature of the χ^2 surface. An observer presented with this set of measurements must infer the original pulsar properties.

Focusing here on the height measurement, we test the systematic bias in the RVM estimate. For best comparison with the BCW assumptions, we work with the height determined from the phase lag measured from the peak of a Gaussian pulse centered on the magnetic axis. In Figure 5.2, the color scale represent the number of pulsars in the simulated population at a given altitude derived from fitting RVM versus the difference between fitted and real altitude. Figure 5.2 shows that r_f increasingly underestimates r_r at increasing altitude. A simple formula to provide improved height estimates r'_f from RVM fits is then

$$r'_f = r_f + 0.2(r_f/0.5)^2, \quad (5.4)$$

as plotted in Figure 5.2. The line fits best to the darkest ridge (the ridge that contains a majority of simulated pulsars) for the models using the maximum of a simple Gaussian intensity peak (G_C) and the center of the cap edges for a circular cap (C_C). For the case using the center of the cap edge for a retarded dipole cap (C_R), the line slightly under-predicts the darkest ridge and does not capture the behavior of the second ridge which is caused by the shift of the central line from the cap notch (see Figure 5.1). We can (unrealistically) assume that we know where

in phase the magnetic axis is located and calculate the altitude from the shift in polarization directly. Inaccuracies in altitude are then from Equation 5.2 alone. With the assumption of perfect knowledge of the magnetic axis (E_B), we see the departure from the BCW formulation occurs at lower altitudes. Apparently, the estimate $\Delta\phi = -2r_f$ for the peak intensity shift preserves good accuracy to higher altitude than the $\Delta\phi = +2r_f$ shift of the polarization sweep, especially when the intensity arises from a circular cap.

In practice, the height offset depends on the geometrical angles (α, ζ) . In addition, the height estimate is affected by uncertainty in estimating the polarization sweep lag, i.e. in determining the phase of the pulse (or equivalently the phase of the magnetic axis). These effects are shown in Figure 5.3. For each panel we show, as a function of the estimated angles (α_f, ζ_f) , the maximum height (color bar) at which the estimated altitude is accurate. For the estimate to be useful, we require that r_r lies in the range $r_f \pm \sigma_{r_f}$ for a large fraction (99%) of the observable model pulsars. At small altitude this is always true. At large altitude the distortion due to the retarded field structure causes increasing departure from the BCW estimate. Once too small a fraction of models produce useful fits, the BCW approximation ‘breaks down’. Lowering the required fraction does not drastically change the results seen in Figure 5.3, since the fraction of failing models increases very rapidly with fit altitude. Also shown is a green contour that marks the area where the bins contain at least fifty simulated pulsars. Uncolored bins are where the BCW approximation is inaccurate at the lowest altitude. The contours are independent of the intensity model (the contours are the same for each model) because the α_f, ζ_f bin depends only on the polarization sweep which is calculated independently of the intensity model.

A strong dependence between the break-down altitude and α_f and ζ_f exists as can be seen in Figure 5.3. This is not due to any difficulty in finding the phase center but arises from the nontrivial relation between the shift in the maximum sweep of the polarization and the geometry angles. In Figure 5.3, we can see that for α_f and ζ_f further from 90° , BCW tends to break down at a lower altitude. The shift in the maximum sweep of the polarization angles for these values is smaller than predicted by the BCW model. Since the BCW model has no dependence on α and ζ , it is not

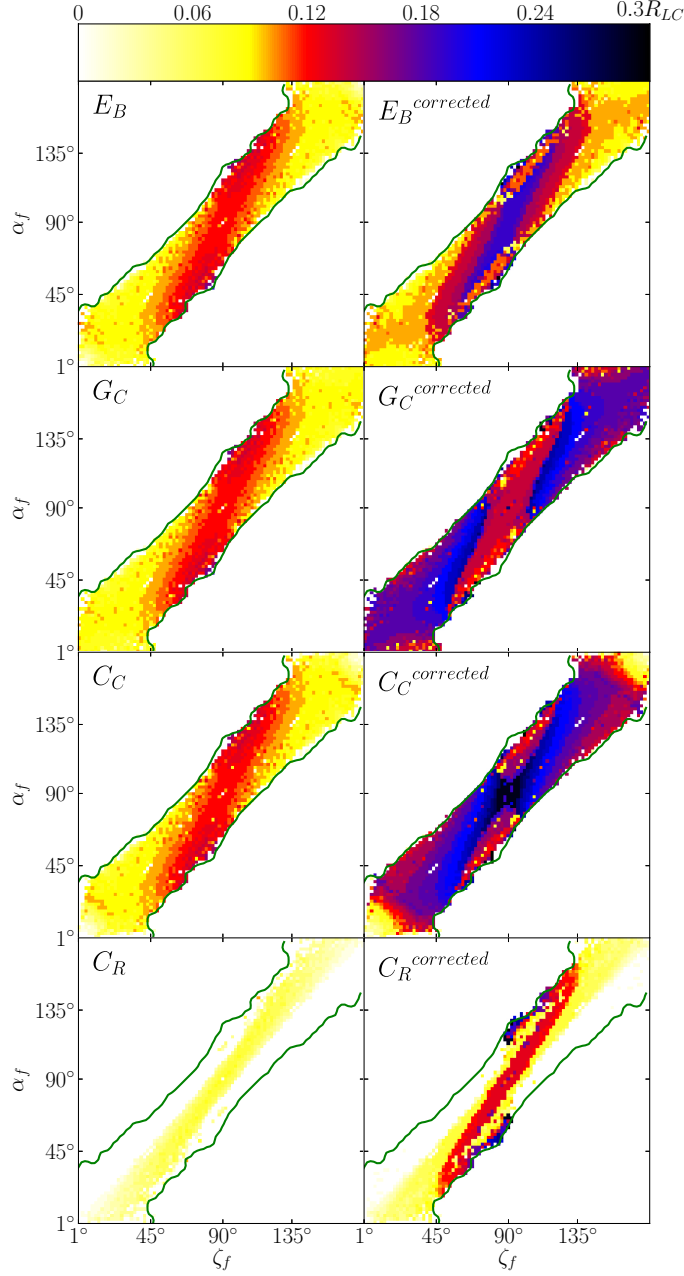


Figure 5.3: Maximum useful r_f altitude (color bar) in the (α_f, ζ_f) plane for four assumptions about the pulse intensity beam shape (see text for our criterion for good fit accuracy). Left: BCW estimates before correction. Right: corrected heights using Equation 5.4. Green contours indicate the area where at least fifty simulated pulsars were fit to an (α_f, ζ_f) pair.

surprising that the break-down altitude has a dependence on these angles.

The panels show the maximum useful height for four different estimates of the phase lag: (top-to-bottom) perfect knowledge of the magnetic axis, a Gaussian pulse peaked on the magnetic axis field line, a ‘conal’ pulse from a field lines with a circular cap on the star and a ‘conal’ pulse with a cap determined by the detailed open zone of the retarded vacuum solution. Notice that most observed pulsars have modest $|\beta| = |\zeta - \alpha|$, and are close to the diagonal. The right panels show the equivalent maximum useful height when the estimate has been corrected according to Equation 5.4. While the uncorrected estimates for the Gaussian pulse peak model are useful only to an average (over α_f and ζ_f) height of $\bar{r}_f = 0.11R_{LC}$, the corrected estimates are usable to higher altitudes (reaching $r'_f \sim 0.3$ for the commonly observed case of near-orthogonal rotators) with an average of $\bar{r}_f = 0.22R_{LC}$. Again, corrected RVM estimates from a model radio pulse do better than estimates assuming perfect knowledge of the magnetic axis, since the retarded potential phase shifts are a fractionally larger contribution to the phase offset in this case.

We can improve the heuristic correction function by including the viewing geometry. The bulk of the sensitivity is evidently due to ζ_f , as illustrated by the relatively small dispersion of the r_f error for individual ζ_f slices (see Figure 5.4 for a Gaussian central pulse). Accordingly, we have made an alternate corrected height estimate

$$r'_f = r_f + [0.3 + 0.7|\cos(\zeta)|](r_f/0.5)^3 \quad (5.5)$$

where $r_f = \Delta\phi/4$, as usual. This greatly extends the range for which a simple RVM height estimate can be used (Figure 5.5). This estimate, based on a Gaussian radio pulse emitted along the swept back magnetic axis, is in general the best function for an observer to use with no other information. It provides significant improvement in the emission height accuracy for the circular cone pulse profiles.

Of course if one has reason to believe that a particular pulse profile shape is more accurate, a different correction function may be preferred. For example if one had a double pulse arising from the open zone edges (C_R) and had high confidence that

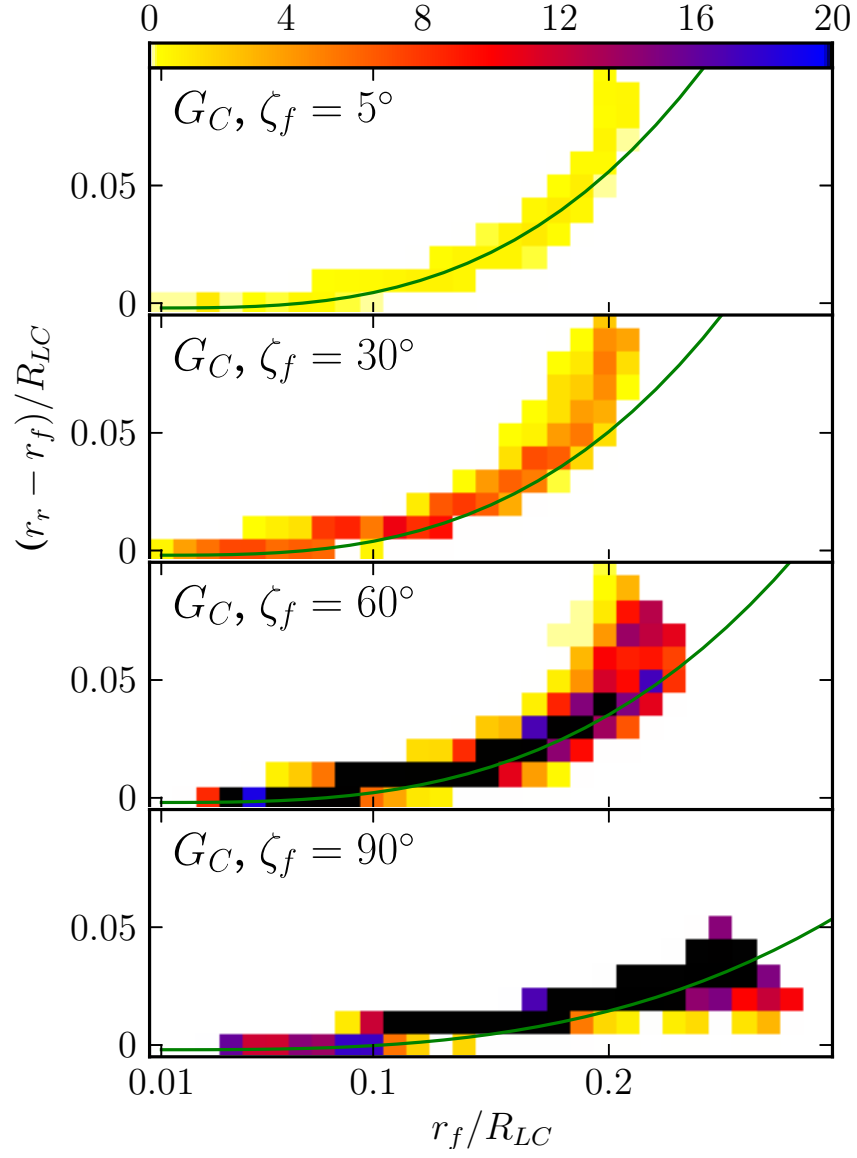


Figure 5.4: Altitude limits for effective RVM fits. Each panel shows the distribution of simulated model fits (color bar) in offset from the true altitude as a function of fit altitude r_f/R_{LC} for different ζ_f , assuming a simple Gaussian intensity peak, $\phi = 0$ inferred from the altitude dependent shift of I_{\max} . For these plots, the simulated pulsar population has been summed over α_f to emphasize the dominance of ζ_f in the correlation. The green curve shows our estimate of the bias with dependence on ζ_f , Equation 5.5.

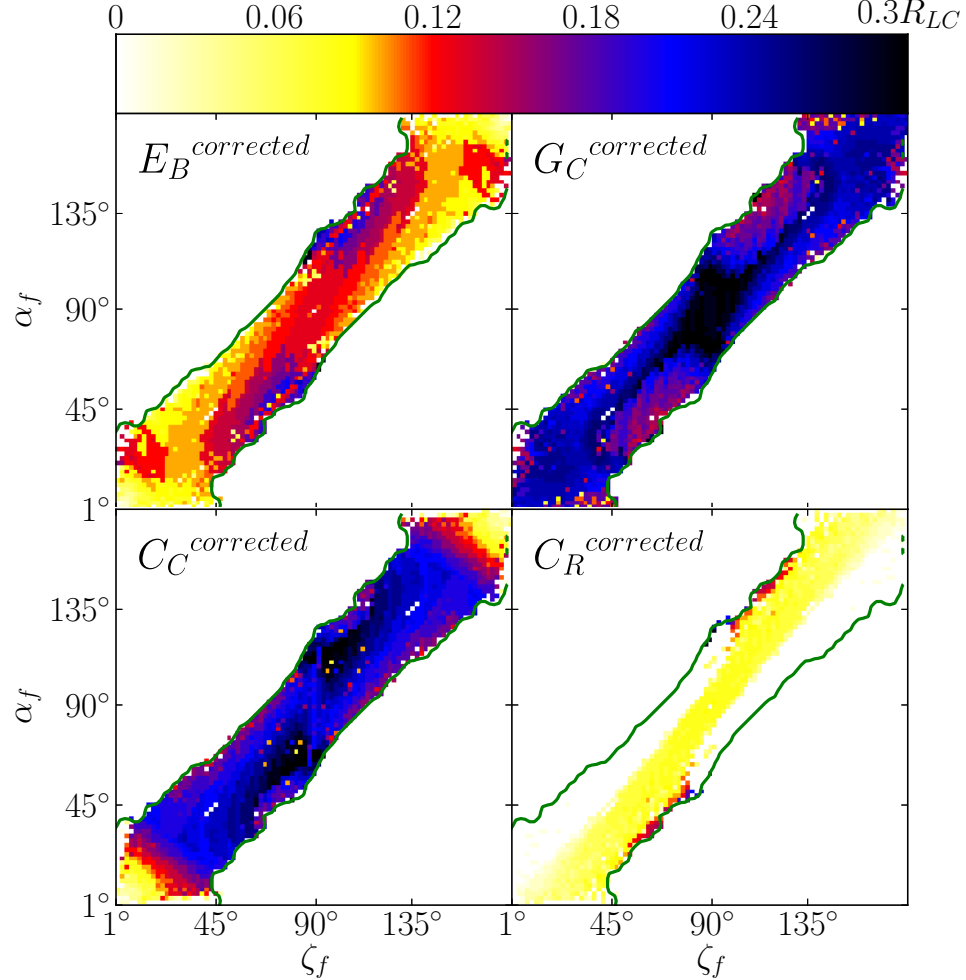


Figure 5.5: Maximum altitude for accurate height estimates (color bar) in the (α_f, ζ_f) plane, after applying Equation 5.5 (see text for our criterion for good fit accuracy). Note that the improvement is best for a circular (Gaussian or conal) cap. Green contours indicate the area where at least fifty simulated pulsars were fit to an (α_f, ζ_f) pair.

this pulse filled the retarded vacuum dipole open zone, one would correct by

$$r'_f = r_f + [0.3 + 2|\cos(\zeta)|^2](r_f/0.5)^3. \quad (5.6)$$

This formulation raises the average over α_f and ζ_f of the maximum useful height from $\bar{r}_f = 0.05R_{LC}$ with no correction to $\bar{r}_f = 0.15R_{LC}$.

In general, we recommend that when an observer fits an RVM model to pulsar data, obtaining viewing angle and polarization sweep lag measurements, they correct their height estimate using Equation 5.5. This is particularly useful whenever the RVM fit appears statistically adequate, but the resulting phase lag suggests a significant emission height. The change to the estimated height will be small for $r_f < 0.2$, but the accuracy of the resulting estimate will be greatly increased.

Of course, whenever $\chi^2/\text{DOF} \gg 1$ at the fit minimum, it is a sign that the model is inadequate. In many cases, this will be due to unmodeled orthogonal mode jumps and intervening scattering (Karastergiou, 2009), higher order multipoles, etc. However, for large altitudes and multi-altitude emission the effects of sweep back and the formation of caustics (which dominate γ -ray light curves) become dominant. The observer should be aware that large χ^2 at the fit minimum can signal such effects and, when the inferred altitude is large, consider fitting the data to numerical models of 3-D pulsar magnetospheres.

5.4 Height Calculation from Shift in ψ

We can alternatively estimate r_f and errors using the shift in ψ (Hibschman & Arons, 2001),

$$\Delta\psi \approx \frac{10}{3}r \cos(\alpha) \left[\frac{3}{8} + \frac{5}{8} \cos(\zeta - \alpha) \right] - \frac{47}{18}r \sin(\alpha) \sin(\zeta - \alpha) \quad (5.7)$$

or, in the small $|\beta| = |\zeta - \alpha|$ limit, $\Delta\psi \approx \frac{10}{3}r \cos(\alpha)$. As before, we compute the residual, $r_r - r_f$, as a function of α_f , ζ_f , and r_f . To estimate an emission height from the polarization shift in ϕ , one needs an estimate for $\phi = 0$, e.g. from a pulse peak intensity model; no such intensity model is needed if we have a measurable shift in ψ . The increase with r_f are shown in Figure 5.6, where the left panel uses the small β limit while the right uses the full formula. As for the $\Delta\phi$ estimate, the errors increase with r_f . However here, even when the full Equation 5.7 is used, the corrections show a substantial spread. In fact the uncorrected formula proves accurate ($|r_f - r_r|$ within

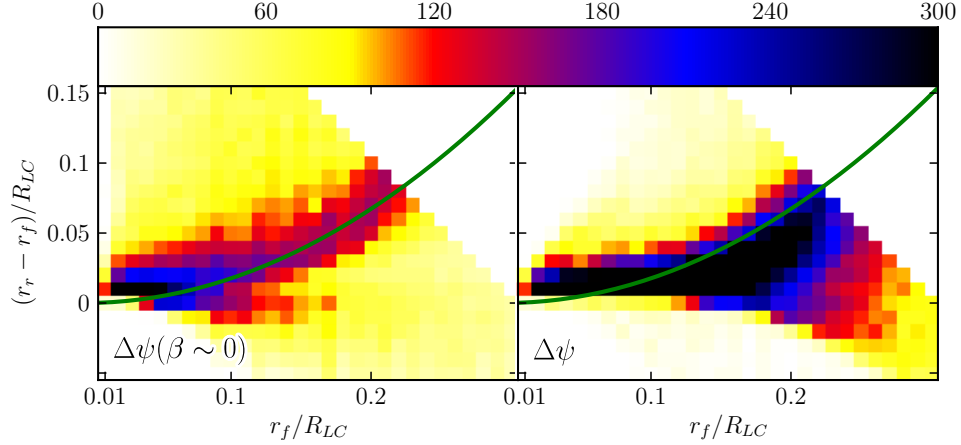


Figure 5.6: Altitude limits for effective RVM fits using the shift in ψ . Each panel shows the distribution of simulated model fits (color bar) in offset from the true altitude as a function of fit altitude r_f/R_{LC} . The dark band shows the systematic bias in the fit offset. The residual is more scattered when the altitude is measured from the shift in ψ instead of the shift in ϕ of the polarization sweep. On the left is the residual using the small $|\beta|$ limit. The green curve shows our estimate of the bias from the shift in ψ , Equation 5.8.

σ_{r_f} 99% of the time) only for $\bar{r}_f < 0.08$ (where \bar{r}_f is again the average over α_f and ζ_f) and for $\zeta_f < 60^\circ$ or $\zeta_f > 120^\circ$. For near-orthogonal rotators the estimate is unreliable at the lowest altitudes.

A heuristic correction to the $\Delta\psi$ estimate for Equation 5.7 can be made for $\zeta_f < 60^\circ$ or $\zeta_f > 120^\circ$

$$r'_f = r_f + 0.4(r_f/0.5)^2 \quad (5.8)$$

which allows accurate estimates to $\bar{r}_f = 0.12R_{LC}$. Including the ζ dependence,

$$r'_f = r_f + [0.2 + 0.1|\cos(\zeta)|^2](r_f/0.5)^2 \quad (5.9)$$

raises the useful range to $\bar{r}_f = 0.18R_{LC}$. Considering that the correction for the common orthogonal rotator case is especially poor, and that it is often difficult to infer the intrinsic ψ_0 , height estimates from the phase shift remain much more useful.

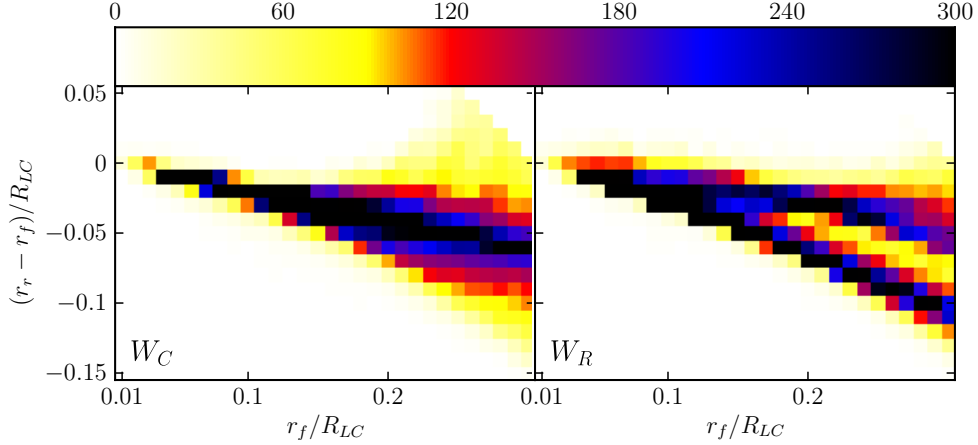


Figure 5.7: Altitude limits for effective pulse width. Each panel shows the distribution of simulated model fits (color bar) in offset from the true altitude as a function of fit altitude r_f/R_{LC} . W_C : Circular cap. W_R : Retarded dipole cap. The simple static dipole formula overestimates the altitude needed to accommodate a given pulse with W in the open zone. The error depends on the viewing geometry α and ζ , and bifurcates for the ‘notched’ cap of the formal retarded potential open zone.

5.5 Pulse Width Dependence on Emission Height

Since the field lines flare in the open zone, the full phase width W of the observed radio pulse can also be checked against the expected radio emission altitude. The standard prescription assumes a circular cap and static dipole field lines to infer a minimum height

$$r_W = \frac{4}{9} \arccos^2 \left[\cos(\alpha) \cos(\zeta) + \sin(\alpha) \sin(\zeta) \cos \left(\frac{W}{2} \right) \right]. \quad (5.10)$$

In Figure 5.7 we show that the retarded dipole field flares *more* than predicted by this simple formula and hence the minimum height in Equation 5.10 is an *over-estimate*. Thus, in general, lower altitudes are consistent with a given observed pulse width than suggested by this formula. Moreover, we expect that the general effect of currents in the magnetosphere will be to increase the foot-point angles of the open zone. This further increases the allowed W at a given height.

In general, larger widths are still most easily accommodated at large r or small

α , but sweep-back and magnetospheric currents substantially weaken the minimum altitude constraints from the commonly used Equation 5.10. Given the large sensitivity to the details of the open zone volume and the presently unknown effect of magnetospheric currents, it is not worth developing corrections to this formula.

5.6 Conclusions; Examples from Literature

We conclude by examining a few RVM/BCW estimates of emission height present in the literature.

In Romani et al. (2011), $\Delta\phi$ estimates were used to suggest large emission heights for two young energetic pulsars. For PSR J0538+2817 the shift gives $r_f = 0.15R_{LC}$, but RVM fitting only weakly constrains ζ . Applying Equation 5.4, we would infer $r'_f = 0.17R_{LC}$, a small, but significant increase which makes it easier to accommodate the large observed pulse width. Similarly PSR J1740+1000 gives $r_f = 0.12R_{LC}$. Here we constrain $\zeta = 80^\circ$ to 130° , so that the corrected fit altitude (Equation 5.4 or Equation 5.5) is $r'_f = 0.13R_{LC}$, again a small but statistically significant increase.

For millisecond pulsars the effects can be larger. For example, Keith et al. (2012) find that RVM fitting can be usefully applied to several recycled pulsars. PSR J1502-6752 ($P=26.7$ ms) is a mildly recycled pulsar for which the phase lag implies $r_f = 0.2R_{LC}$. With no significant ζ constraints, we apply Equation 5.4 to infer a 16% altitude increase to $r'_f = 0.23R_{LC}$. Similarly PSR J1708-3506 ($P = 4.5$ ms) has a phase shift implying $0.19R_{LC}$, which we correct to $0.21 - 0.22R_{LC}$. For this pulsar, a naive application of the pulse width formula (5.10) gives altitudes of $r_{W_{10}} \simeq 0.65R_{LC}$ (10% peak width). However, the increased r'_f and decreased pulse width height from sweep-back effects (Figure 5.7), along with additional current-induced open zone growth, make it likely that the pulse width can be accommodated at the corrected height.

Keith et al. (2012) also report a RVM/BCW height $r_f = 0.44R_{LC}$ for the $P=2.7$ ms pulsar PSR J1811-2404, along with well constrained viewing angles of $\alpha = 89.7^\circ$ and $\beta = 21^\circ$. While our full analysis does not cover this altitude, as Figure 5.5 shows the corrections of Equation 5.5 give a very high accuracy for orthogonal rotators viewed near 90° . Note in Figure 5.4, bottom panel, that the correction function is

nearly linear thus extrapolation to somewhat higher values may be justified. Naively applying this correction we get $r'_f = 0.81R_{LC}$. We certainly cannot trust this value in detail since plasma effects and other perturbations may be relevant at such altitudes. However, the correction is certainly large and it brings the expected height up to an altitude where the very wide observed radio pulse, and the likely detection of emission from both open zones, can be easily accommodated. Certainly simple RVM/BCW fitting is inadequate for this pulsar and one should use a detailed model for the high altitude field geometry.

Our exercise extends the range of utility of RVM-fit polarization sweeps for inferring the altitudes of radio pulsar emission. For fit altitudes less than $r_f = 0.25R_{LC}$ the corrections are not large, but they are systematic and, for high S/N data localizing the phase of maximum polarization sweep, they can be highly significant. We thus believe it is worth applying our recommended correction. For larger altitudes the corrections grow rapidly, but we caution that as one approaches the light cylinder, current-induced distortions should increase and, except for near-orthogonal rotators, one would expect the RVM formulae to provide a poor fit in any case. Fitting to detailed numerical models is then preferred. In all cases the dominant residual uncertainty is likely in locating the phase of the radio pulse. We also checked the use of absolute polarization axis position angles and pulse width to constrain the emission height. Here the difficulties in establishing the unperturbed ψ_0 and the expected distortions of the open zone boundaries by currents, etc. make the estimates much less useful. Nevertheless, we have shown that the effects of sweep-back do go in the direction of reconciling observed pulsar properties to a consistent emission height: larger heights are inferred by a given $\Delta\psi$ shift and larger pulse widths can be accommodated at a given height. We feel, however, that the corrections are less quantitative than for $\Delta\phi$.

In sum, since observers will continue to apply analytic RVM fits to pulsar polarization data, by applying our recommended correction (Equation 5.5), these results can continue to give accurate height estimates to $\leq 0.3R_{LC}$. At higher heights which will be common for millisecond pulsars, a fit to more detailed numerical models is

likely warranted.

This work was supported in part by NASA grants NNX10AP65G and NAS5-00147.

Chapter 6

Tackling Radio Polarization of Energetic Pulsars

This section is based on work done for “Tackling Radio Polarization of Energetic Pulsars” (Craig, 2014)

The traditional, geometrical rotating vector model (RVM) has proved particularly poor at capturing the polarization sweeps of the young energetic and millisecond pulsars detected by *Fermi*. We augment this model by including finite altitude effects using a swept-back vacuum dipole geometry. By further including the effects of orthogonal mode jumps, multiple emission altitudes, open zone growth via y-point lowering, and interstellar scattering, we show that a wide range of departures from RVM can be modeled well while retaining a geometrical picture. We illustrate these effects by fitting six *Fermi*-detected pulsars (PSR J0023+0923, PSR J1024–0719, PSR J1744–1134, PSR J1057–5226, PSR J1420–6048, and PSR J2124–3358) and we describe how such modeling can improve our understanding of their emission geometry.

6.1 Introduction

For pulsars emitting in the radio, the conventional assumption is that the electric vector position angle follows the projection onto the plane of the sky from the magnetic field line at the emission point. Polarization position angle curves (position angle versus pulsar phase), which we see as the pulsar sweeps past our field of view, are very closely related to the orientation of the magnetic field lines. Analysis of radio polarization is a powerful tool for understanding the geometry of pulsars. For example, polarization contains information about the phase of closest approach of the surface dipole axis. Additionally, polarization has traditionally been used to place strong constraints on the impact angle, the angle between the magnetic pole of the pulsar, and the viewing direction. Modeling polarization should also give estimates for the geometric parameters α , the angle of magnetic axes, and ζ , the viewing angle.

Naively, such projections should result in smooth polarization curves versus the pulsar period phase, particularly when adopting a point dipole model. We argue that zero altitude models are not appropriate for certain pulsars. In stark contrast, a relatively recent paper, Yan et al. (2011) exhibits the multitude of shapes that occur in millisecond pulsar polarization. More subtly, both polarization angle sweeps originating from zero altitude and polarization angle sweeps originating from a single, finite altitude can differ significantly in shape, although both appear smooth. Emission from finite altitude is a consideration for both millisecond pulsars and young pulsars. Karastergiou & Johnston (2007) give the emission altitude of young pulsars as 950–1000 km. This emission altitude is then $0.02 \times 1000/P_{\text{ms}} R_{\text{LC}}$ in terms of the light cylinder radius. The light cylinder radius, R_{LC} , is the distance from the center of the neutron star at which co-rotating particles would be traveling at the speed of light. Since $P_{\text{ms}} < 100$ ms for young pulsars, their emission altitude would be $> 0.2R_{\text{LC}}$, a significant fraction of the light cylinder. The neutron star radius in terms of light cylinder is $0.02 \times 10/P_{\text{ms}} R_{\text{LC}}$ for a neutron star radius of 10 km. For millisecond pulsars with $P_{\text{ms}} < 5$ ms, emission must come from $> 0.04R_{\text{LC}}$, which is also a significant fraction of the light cylinder.

Precise modeling of millisecond pulsar and young pulsar radio polarization is of

particular interest now because of the growth of γ -ray data from the *Fermi Gamma-Ray Space Telescope*. These energetic pulsars make up the γ -ray pulsar population. Thus, the understanding of γ -ray models can potentially benefit from radio polarization modeling because of the constraints on geometry that polarization often provides. All pulsars considered in this paper are *Fermi*-detected pulsars.

In essence, the present paper is an extension of the Karastergiou (2009) paper in which the author shows one can produce theoretical polarization curves similar to those observed using orthogonal mode jumps and interstellar scattering. Here, we also allow for emission from finite altitude (numerically calculated). Although analytically calculated modifications exist for small altitude emission, such calculations contain estimates that break down at altitudes $\sim 0.1R_{LC}$. Our model also allows for multiple altitudes of emission. Differences in altitude can explain non-90° position angle jumps seen particularly in millisecond pulsar polarization data. Another major difference between Karastergiou (2009) and the present paper is that we seek to quantitatively fit the model to the data resulting in parameters with error bars and χ^2 estimates. In contrast, Karastergiou (2009) was satisfied with producing polarization sweeps that appeared qualitatively similar to the data. Further, using the *F*-test, we compare the χ^2 of the simplistic point dipole model and our more complex model to statistically quantify whether the modifications are significant. This paper is a methods paper that chooses pulsars that can clearly illustrate the strengths of this model; we do not tackle a large sample.

In Section 6.2 of this paper, we discuss the rotating vector model (RVM) and how the discrepancies between data and the model demand a reevaluation of RVM. In Section 6.3, we describe the constituents of the model in detail. In Section 6.4, we describe the nuances of fitting the model. Section 6.4.1 focuses on a parameter ρ_{ypt} which we define and use heavily in this paper and which is a measure of the extent of the effective open zone required by phase of emission. We apply the model to data in Section 6.5. Table 6.1 gives property parameters to the pulsars analysed.

6.2 Rotating Vector Model and Beyond

We will start by discussing the analytic models used for radio position angle polarization and their shortcomings and then transition into the numerical model used for this paper. The model predominately used for radio position angle polarization is the RVM which was formulated by Radhakrishnan & Cooke (1969). The RVM is simple and states that pulsars are point dipoles with emission from the surface of the neutron star. The analytic RVM formula for polarization angles (ψ) is

$$\psi = \arctan \left[\frac{-\sin(\alpha) \sin(\phi + \Delta\phi)}{\sin(\zeta) \cos(\alpha) - \cos(\zeta) \sin(\alpha) \cos(\phi + \Delta\phi)} \right] + \Delta\psi, \quad (6.1)$$

where the inclination angle between the rotation axis and magnetic axis is α , the viewing angle is ζ , and the pulse phase is ϕ . Measures of horizontal and vertical offset are contained in $\Delta\psi$ and $\Delta\phi$. These are the absolute phase and position angle on the sky of the magnetic axis.

Table 6.1: Property Parameters of the Pulsars

Name	Period (ms)	R_{LC}/R_{NS}	f (GHz)	DM (cm $^{-3}$ pc)
J0023+0923	3.05	12.5	1.649	14.326
J1024–0719	5.162	20.0	1.369	6.49
J1057–5226	197.11	1000	1.5	30.1
J1744–1134	4.075	16.7	1.369	3.14
J1420–6048	68	250	1.5 and 3	360
J2124–3358	4.931	20.0	1.369	4.60

Despite its simplicity, the RVM has been applied to numerous pulsars with great success (i.e., Lyne & Manchester, 1988; Phillips, 1990; Everett & Weisberg, 2001). These pulsars are generally old, spun-down pulsars with long periods and low altitudes of emission. Blaskiewicz et al. (1991) (the Blaskiewicz, Cordes, & Wassermann, or BCW model) modified the RVM to include finite altitude and found that the point of fastest change in the polarization position angle sweep will shift back in phase due to sweep-back effects on the magnetic field lines, while the intensity profile shifts

forward in phase due to co-rotation of the particles in the pulsar magnetosphere. Therefore, by fitting the position angle data to the RVM and measuring this shift, one can estimate altitude.

The BCW formula with altitude (r) dependence measured in R_{LC} is given by

$$\psi = \arctan \left[\frac{-\sin(\alpha) \sin(\phi - 2r)}{\sin(\zeta) \cos(\alpha) - \cos(\zeta) \sin(\alpha) \cos(\phi - 2r)} \right] + \Delta\psi \quad (6.2)$$

(Dyks, 2008).

The formula is approximate and breaks down as altitude increases. The breakdown occurs between $\sim 0.05R_{LC}$ and $\sim 0.12R_{LC}$ at best, below or near altitudes expected for energetic young and millisecond pulsars. One can apply correction formulae to boost the break-down altitude to $\sim 0.3R_{LC}$, but even these formulae are sensitive to α and ζ and depend on an assumed radio intensity model (Craig & Romani, 2012). In essence, neither the RVM nor the BCW captures the morphological changes in the radio polarization position angle sweep at high altitudes which are needed to model high-energy, γ -ray emitting pulsars.

Further, the RVM produces smooth S-shaped position angle sweeps versus phase that resemble data from older, low-energy pulsars. Polarization position angle data from millisecond pulsars, on the other hand, are riddled with jumps, cusps, and sharp turns (i.e., Yan et al., 2011; Everett & Weisberg, 2001) which are absent in the RVM (the strongest evidence that the RVM lacks essential physical features needed to understand emission from these pulsars). By combining four physically motivated, data-driven ingredients (numerically calculated finite altitude, multiple altitudes, orthogonal mode jumps, and interstellar scattering), we hope to explain some of the features seen in the radio data of *Fermi* pulsars for which the RVM alone fails.

In the model presented in this paper, and in contrast to the RVM and the BCW, finite altitude polarization is calculated using numerical computation, which avoids the approximations needed in the BCW. The retarded dipole presented in Kaburaki (1980) and used in Watters & Romani (2011) is used in this modeling. Particles follow magnetic field lines to a given altitude of emission (as measured radially from the center of the neutron star) and, similar to the RVM, radiate tangent to the field

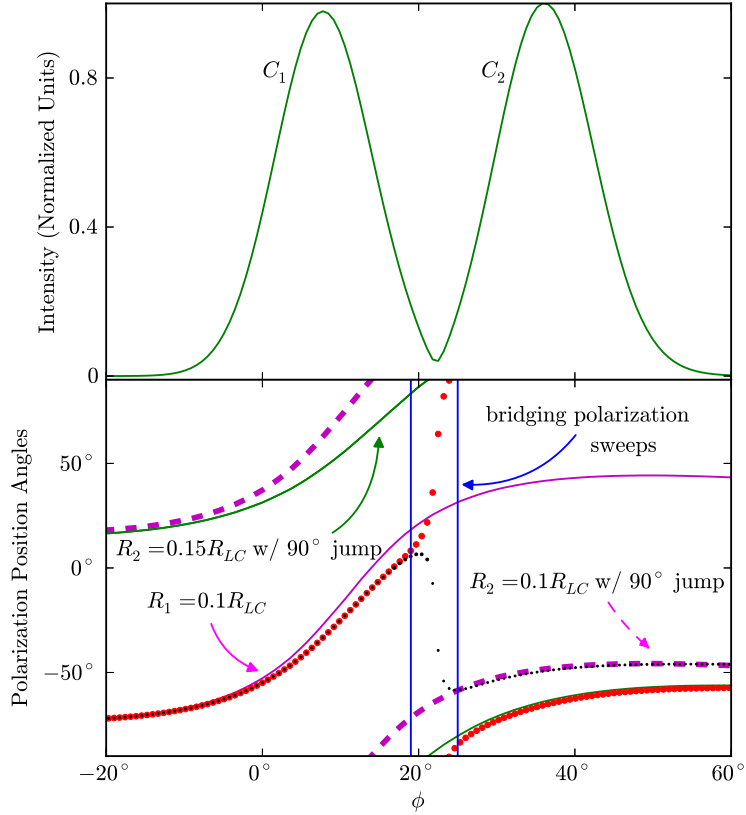


Figure 6.1: Plot of model pulsar intensity and polarization sweep showing the effects of single and multiple altitudes with a small scattering constant. The model parameters are $\alpha = 145^\circ$, $\zeta = 140^\circ$, $P = 5$ ms, and $\tau = 0.03$ ms. The black points are polarization position angles for a model with $R_1 = 0.1R_{LC}$ for polarization associated with intensity component C_1 and $R_2 = 0.15R_{LC}$ plus an orthogonal mode jump for polarization associated with intensity component C_2 . The red points are polarization position angles for a model with $R_1 = 0.1R_{LC}$ for polarization associated with intensity component C_1 and $R_2 = 0.1R_{LC}$ plus an orthogonal mode jump for polarization associated with intensity component C_2 . Each model polarization sweep for a given component is weighted using the Gaussian intensity profile. Subtle changes in altitude can create drastic changes in the direction of the bridging polarization in the phase of orthogonal mode jump. The two Gaussian components of model intensity are equal in amplitude but interstellar scattering effects make the first Gaussian component in phase (C_1) slightly lower in amplitude compared with the second Gaussian component in phase (C_2). A phase of zero is the point of closest encounter to the magnetic axis in the model.

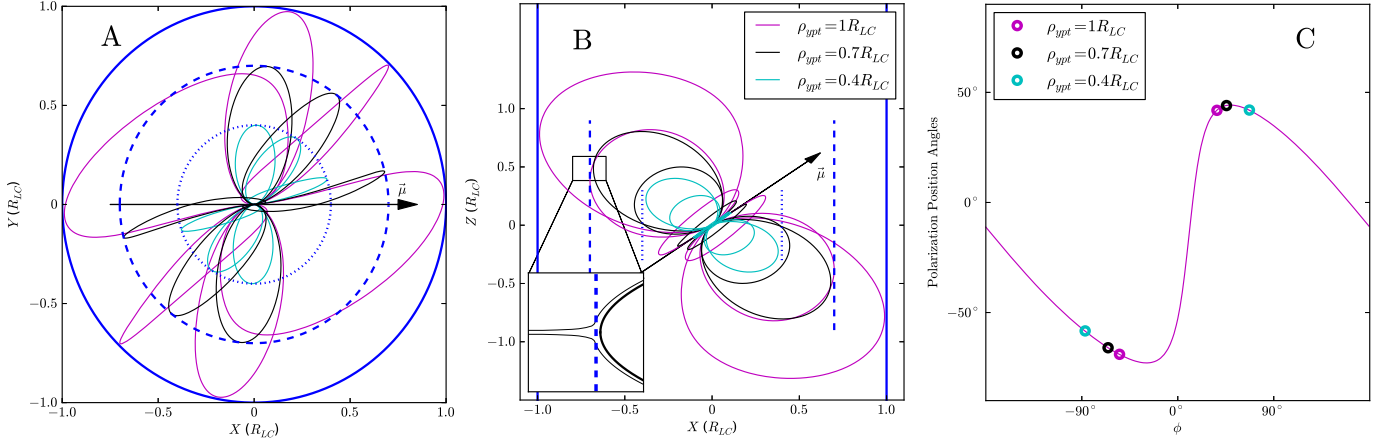


Figure 6.2: Panels (A) and (B) show pulsar magnetic field lines at various viewing angles for a pulsar with $\alpha = 45^\circ$. The magenta lines are the last closed field lines of a vacuum dipole and the solid blue lines represent the light cylinder ($1R_{LC}$). Formally, for the vacuum dipole model, the y-point radius (ρ_{ypt}), the cylindrical radius from the spin axis at which the closed and open field lines are adjacent, is $\rho_{ypt} = 1R_{LC}$. In reality, due to finite mass and current effects, $\rho_{ypt} < 1R_{LC}$. Also plotted is the last closed field lines for $\rho_{ypt} = 0.7R_{LC}$ and $\rho_{ypt} = 0.4R_{LC}$. The inset plot of panel (B) shows a close-up of the y-point area and illustrates why this point is called the y-point. Panel (C) shows a typical model polarization sweep with $\alpha = 145^\circ$, $\zeta = 140^\circ$, and $R = 0.1R_{LC}$. Open circles mark the expected emission phase for the model. Decreasing ρ_{ypt} increases the phase of emission. A phase of zero is the point of closest encounter to the magnetic axis in the model.

line. Co-rotation and time-of-flight effects are then applied when emission from the lab frame is projected onto the plane of the sky (that is, $\psi = \psi_v + (|\Omega|/c)\mathbf{r} \cdot \hat{\mathbf{k}}$ where ψ is the pulsar phase, ψ_v is the co-rotational velocity in the $\hat{\psi}$ direction, \mathbf{r} is the origin of the emitted photon, and $\hat{\mathbf{k}}$ is the direction of the photon motion in the co-rotation frame). The numerical model is particularly valid at lower altitudes of emission and we will often favor fits to the model with low altitude results. High altitude emission requires a force-free model. We ignore magnetospheric charge and current present in force-free models, implicitly assuming that such effects occur at higher altitudes than

considered here.

The numerical model does not include the superposition of multiple emission heights which would result in caustics; the altitudes are defined by a single radial distance from the center of the neutron star. The numerical model does not include cross-drift of particles or higher-order multipoles.

6.3 Adding Physical Ingredients

6.3.1 Multiple Altitudes

In order to include multiple altitudes, we invoke the patchy cone model (Lyne & Manchester, 1988; Karastergiou & Johnston, 2007), which holds that different components of the pulsar intensity profile come from different areas of the magnetosphere, and hence, different altitudes. The polarized intensity is modeled by a combination of Gaussian profiles. The Gaussian profiles are modeled after those used in Karastergiou (2009). Each Gaussian component or set of Gaussian components is assigned an altitude (R_1 , R_2 , etc.). We used as few altitudes as will result in a reasonable fit and multiple components often have a single altitude. The Stokes parameters are calculated from the model polarization position angles and these Gaussian components weigh the Stokes parameters Q and U from different altitudes to calculate a single polarization position angle per phase bin:

$$\begin{aligned} Q_{\text{tot}}(\phi) &= \sum_n g_n(\phi) \cos(2\psi_n(\phi)), \\ U_{\text{tot}}(\phi) &= \sum_n g_n(\phi) \sin(2\psi_n(\phi)), \\ \psi(\phi) &= \frac{1}{2} \arctan \left(\frac{U_{\text{tot}}(\phi)}{Q_{\text{tot}}(\phi)} \right) \end{aligned} \quad (6.3)$$

(Karastergiou, 2009). Here $g_n(\phi)$ is a Gaussian component and $\psi_n(\phi)$ is the model polarization associated with that component.

The allowable altitude range in the model is $R = R_{\text{NS}}$ (the neutron star radius)

to $R = .9R_{LC}$. Admittedly, we do not attempt to quantify how high of an emission height is too far from the neutron star surface to apply a vacuum model for predictions of polarization position angles. In all likelihood, there will be a smooth deviation of the polarization predicted by the vacuum model from the actual polarization with increasing model altitude and with strong dependence on α , ζ , and the exact location of the emission origin within the magnetosphere. Recent and future studies combining vacuum and force-free models (Kalapotharakos et al., 2012a) applied to polarization may hold the key to quantifying this breakdown.

The cone–core model is similar to the patchy cone model but more restrictive. Physically, a cone of emission beams from the pulsar cap, flaring out at higher altitudes (Radhakrishnan & Cooke, 1969). The central part of the intensity pulse profile originates from emission low in the magnetosphere near the neutron star surface and the wings of the intensity pulse profile originates from emission high in the magnetosphere. We do not force a cone–core model when fitting altitude but radio modeling of PSR J0023+0923 and PSR J1024–0719 favor high altitude–low altitude–high altitude emission (versus phase) based on polarization fitting as discussed in Sections 6.5.1 and 6.5.2.

The number of model altitudes used in each fit was motivated by the polarization data. For PSR J0023+0923 and PSR J1024–0719, we applied two-altitude fits since our conjecture is that the “jump” seen in the polarization sweep is from a change in emission altitude (Sections 6.5.1 and 6.5.2). For PSR J1057–5226 and PSR J1744–1134 (Sections 6.5.3 and 6.5.4), we applied both one and two-altitude fitting schemes. Although a single-altitude fit would result in a simpler model, it is not unreasonable to assume that emission from opposite poles or at drastically different pulsar phases originates from different heights. Only one altitude was used in the fitting of the polarization position angle data of PSR J1420–6048 because of the single smooth sweep in the data (Section 6.5.5). Polarization data from PSR J2124–3358 (Section 6.5.6) was fit with more altitudes than reported here but such fits did not drastically change the χ^2_{min} , the χ^2 map, nor the fit altitudes. For the sake of simplicity, we only report the three-altitude fit results.

6.3.2 Interstellar Scattering

Interstellar scattering causes a delay of signal as it travels through the medium of space. The result is a delay of the peak, an exponential tail on the intensity profile, and a flattening of the position angle sweep as polarization information from earlier phases “leaks” into polarization in later phases (e.g., Li & Han, 2003). Scattering can be characterized by a scattering time constant (τ_s) and a scattering kernel:

$$g_{ts}(t - t') = \begin{cases} 0, & t - t' < 0 \\ e^{-(t-t')/\tau_s}, & t - t' > 0 \end{cases} \quad (6.4)$$

(Cronyn, 1970). Other response functions also exist, but this scattering kernel (a thin scattering screen halfway between the source and the observer) is incorporated in the model of this paper. Scattering time constants (τ_s) as calculated using the Cordes & Lazio (2002) model are used in the computations but are negligible for all pulsars except for PSR J1420–6048 in which scattering time was a free parameter (see Section 6.5.5 for details).

Adding scattering to position angle polarization is done by convolving the scattering kernel with $Q_{\text{tot}}(\phi)$ and $U_{\text{tot}}(\phi)$:

$$\begin{aligned} Q_{\text{tot}}^{\text{scat}}(\phi) &= \int Q_{\text{tot}}(\phi(t')) g(t - t') dt', \\ U_{\text{tot}}^{\text{scat}}(\phi) &= \int U_{\text{tot}}(\phi(t')) g(t - t') dt'. \end{aligned} \quad (6.5)$$

The resulting $Q_{\text{tot}}^{\text{scat}}(\phi)$ and $U_{\text{tot}}^{\text{scat}}(\phi)$ are plugged into Equation 6.3 (bottom line) to obtain polarization. Further, model linear intensity with interstellar scattering is calculated using $\sqrt{Q_{\text{tot}}^{\text{scat}}(\phi)^2 + U_{\text{tot}}^{\text{scat}}(\phi)^2}$.

6.3.3 Orthogonal Mode Jumps in the Context of Multiple Altitudes and Interstellar Scattering

The model also includes orthogonal mode jumps in the polarization position angle sweep (Backer et al., 1976). To create orthogonal jumps, 90° is added to the model

polarization position angles ($\psi + 90^\circ$); Q and U model values can be calculated and used in Equations 6.3 and 6.5 the same as unjumped polarization. We do not attempt to understand the origin of these jumps since our model does not contain the physics needed to do so but rather we use the jumps on the basis of empirical observation (e.g., Stinebring et al. 1984; Gould & Lyne 1998; Karastergiou et al. 2005). Note that components of polarized intensity at the same altitude but in different modes will cancel exactly where their individual absolute intensities are equal (Equation 6.3). Polarized intensity going to zero at a given phase in the intensity profile indicates an orthogonal mode jump. Further, if the orthogonal mode jump occurs between components of different altitudes, the polarized intensity will not cancel exactly, although in most cases it will be near zero.

Additionally, without multiple altitudes, only 90° jumps are allowed and the direction of the bridging polarization position angle sweep between the jump is in the opposite direction from the sweep without the jump. Mathematically, this is due to the forward scattering nature of the scattering kernel. Equation 6.5 is nonzero only for $t - t' > 0$ and convolution with such a function will mathematically cause polarization from earlier in phase to mix with polarization at any given phase. Similarly, this is why the second model Gaussian component in phase (C_2) is higher in intensity than the first (C_1) in Figure 6.1.

Figure 6.1 illustrates some properties of scattering and mode jumps that will be of particular interest in the analysis of fitting PSR J0023+0923 and PSR J2124–3358 polarization data. An orthogonal mode jump in the position angle sweep between components of the same altitude will result in a bridging sweep with the opposite curvature compared with the unjumped sweep. In the example figure, the magenta solid line has an upward curvature at the jump phase. The resulting curve with the addition of an orthogonal mode jump (black dots) curves downward at the jump phase. This opposite curvature should always occur due to forward scattering if the individual component altitudes are exactly the same. If the component altitudes are not the same, the bridging curvature between the orthogonal polarization position angles could be the same as or opposite to the curvature of the original sweep direction depending on the polarization position angles (and Stokes parameters) being

combined. This will be an important argument for orthogonal mode jumps between different altitude components in Sections 6.5.1 and 6.5.6.

In Figure 6.1 (along with all subsequent graphs with an x -axis of pulsar phase), the phase of zero is the point of closest encounter to the magnetic axis in the model.

6.4 Fitting Methodology

Simple Gaussian curves were used to model the pulsar intensity. A fixed set of Gaussian phases, widths, and amplitudes drawn by eye that mimic the linear intensity amplitude were used. Formally fitting the pulsar intensity would require simultaneously fitting the polarization position angle parameters and the Gaussian parameters. Such a fit would be computationally intensive and have minimal corrections to the model fits of the polarization.

For the fitting of the polarization position angles, we fit the horizontal and vertical offsets ($\Delta\phi$ and $\Delta\psi$) and altitudes (R_1 , R_2 , etc.) with α and ζ fixed in 1° increments. We used a simulated annealing scheme to find the global minimum for a given α and ζ (Flannery et al., 1992). We then randomly sample the surrounding parameter space within 3σ of the lowest χ^2 for every fixed $\alpha-\zeta$ pair to calculate fit error bars.

Phase cuts were applied to the polarization data points where total normalized intensity dropped below 10% for a given pulse. Error bar cuts were also applied to data points where error bars exceeded $\pm 20^\circ$. Error bar cuts were chosen such that we had good confidence that data points are within half of the 180° range that they can occupy (because of the possibility of orthogonal mode jumps). Phase cuts were chosen such that only data points with a reasonable signal-to-noise ratio were considered.

6.4.1 Y-Point Considerations

The light cylinder is defined as $R_{LC} = cP/2\pi$ where c is the speed of light and P is the period of the pulsar. This cylindrical distance (measured from the neutron star rotation axes) is where particles in co-rotation with the neutron star would be traveling at the speed of light. At this point (or more physically, before this point),

the field lines “break open.” These open field lines are where in the magnetosphere particles accelerate and the pulsar radiates. The point at which an open field line is adjacent to a closed field line is the y-point since the adjacent open and closed field lines form a Y in the field (see Figure 6.2(B) inset for illustration of the y-point). Figure 6.2 (panels (A) and (B)) plots the field lines of a model pulsar with $\alpha = 45^\circ$ (μ is the magnetic axis and the spin axis is vertical). Panel (A) shows a top view of the light cylinder (solid blue lines) while panel (B) shows a side view of the light cylinder. The magenta field lines represent the last closed field lines of a vacuum dipole model with the y-point occurring just beyond the light cylinder.

Studies with force-free simulations (Spitkovsky, 2006) valid at heights near the light cylinder indicate the y-point typically occurs further in than the light cylinder due to particle mass and charge current. The location of the y-point controls the size of the cap of emission from which the open field lines and emission originate. Smaller ρ_{ypt} , the cylindrical distance of the y-point from the neutron star, results in a larger cap, a wider range of viewing angles over which emission can be seen, and a wider phase over which emission is produced. Often, the emission phase in data is too large to be accommodated by the open zone of the formal vacuum dipole even with finite altitude; this is evidence that the field lines break open further in from the light cylinder. The cyan and black field lines in Figure 6.2 illustrate the location and form of the last closed field lines with the y-point distance equal to $\rho_{\text{ypt}} = 0.4R_{\text{LC}}$ or $\rho_{\text{ypt}} = 0.7R_{\text{LC}}$ respectively.

Panel (C) of Figure 6.2 shows the effect of a shifted y-point on the range of emission allowed from open field lines. Panel (C) is a plot of a typical model polarization position angle sweep with $\alpha = 145^\circ$, $\zeta = 140$, and $R = 0.1R_{\text{LC}}$. The open circles mark the region in phase where emission is allowed for various ρ_{ypt} . As ρ_{ypt} decreases, the allowed range of emission increases.

In the modeling for this paper, emission is treated as coming from all field lines not just those defined as open by the formal cap using the light cylinder distance. Polarization data are fit without constraints from the emission phase. We then report the ρ_{ypt} needed for the entire phase of emission seen in the intensity data to be covered by model data in the same phase.

Table 6.2: Fit Parameters for PSR J0023+0923

	DOF	(Unreduced) χ^2_{\min}	α ($^\circ$)	ζ ($^\circ$)	R_1 (R_{LC})	R_2 (R_{LC})	ΔR (R_{LC})
RVM	131-4	1053	$8^{+25(+56)}_{-6(-7)}$	$13^{+38(+71)}_{-10(-11)}$
Region A 2 Alt	131-6	313	$57^{+15(+53)}_{-14(-30)}$	$105^{+14(+36)}_{-16(-47)}$	$0.67^{+0.23(+0.23)}_{-0.24(-0.43)}$	$0.28^{+0.24(+0.33)}_{-0.14(-0.20)}$	$0.39^{+0.23(+0.35)}_{-0.11(-0.23)}$
Region B 2 Alt	131-6	324	$59^{+8(+28)}_{-10(-58)}$	$49^{+2(+7)}_{-5(-48)}$	$0.53^{+0.07(0.17)}_{-0.07(-0.22)}$	$0.90^{+0.00(+0.00)}_{-0.06(-0.27)}$	$-0.37^{+0.08(+0.17)}_{-0.06(-0.22)}$

Note. — Errors reported without (with) parentheses are for 1σ (3σ) from χ^2_{\min} .

6.5 Application (and Illustration) with Individual Pulsars

6.5.1 PSR J0023+0923: Nonorthogonal Jumps with Multiple Altitudes

PSR J0023+0923 is a *Fermi* millisecond pulsar with $P = 3.05$ ms. Figure 6.3 shows the radio pulse profile and the polarization position angles at 1.646 GHz. The polarization sweep cannot be explained well using the RVM because of sharp curvature between intensity components C_2 and C_3 and between components C_3 and C_4 . The RVM with an orthogonal mode jump between these components produces more reasonable fits as reported in Table 6.2. This fit is unsatisfying because the jump is closer to $\sim 60^\circ$ rather than 90° . Fitting with an orthogonal mode jump plus two altitudes (one altitude, R_1 , assigned to C_1 , C_2 , C_4 , and C_5 and a second altitude, R_2 , assigned to C_3) gives a fit with significantly smaller χ^2_{\min} (unreduced $\chi^2_{\min} = 313$ versus unreduced $\chi^2_{\min} = 1053$). By including two physically motivated parameters (the two altitudes), the χ^2_{\min} is decreased by a factor of three. The F -test between the RVM and the two-altitude model gives $F = 149.12$, $\text{DOF}_1 = 2$, and $\text{DOF}_2 = 125$. The F statistic is defined as

$$F = \frac{\frac{\chi^2_1 - \chi^2_2}{\text{DOF}_1}}{\frac{\chi^2_2}{\text{DOF}_2}} \quad (6.6)$$

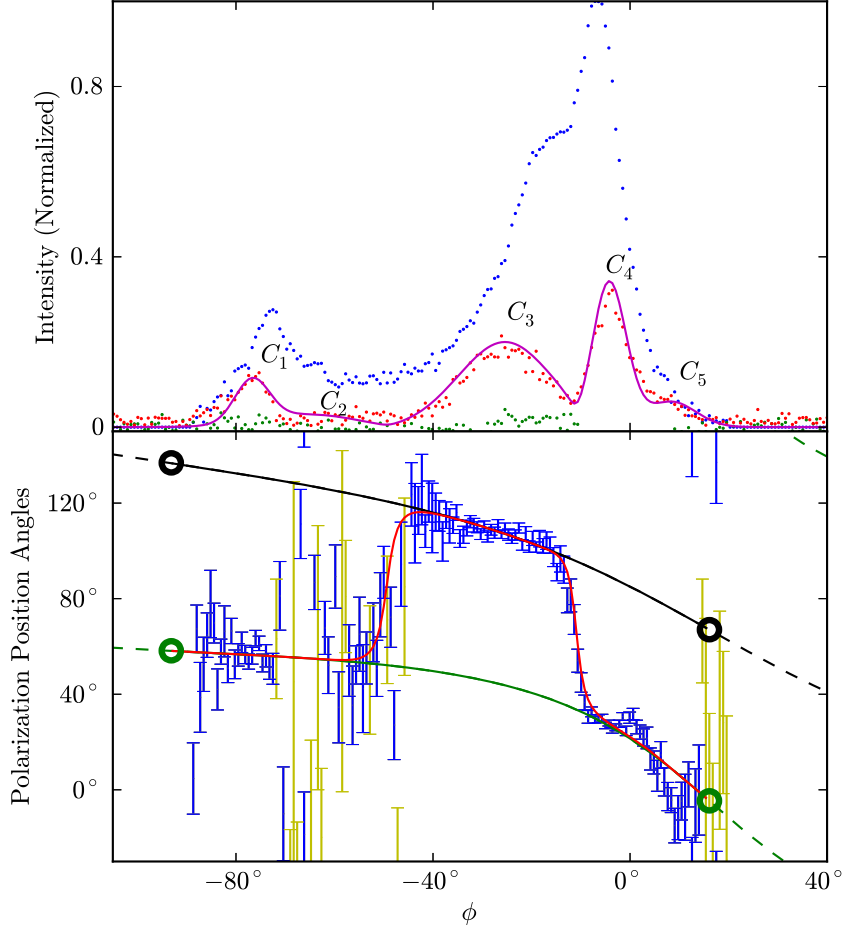


Figure 6.3: In the upper panel, blue points are total radio intensity data at 1.646 GHz, red points are linear polarization intensity data and green points are circular polarization intensity data for PSR J0023+0923. The solid magenta line in the upper panel is the model linear intensity used in fitting. In the bottom panel, blue error bars are polarization position angles used in the fit and yellow error bars are polarization position angles excluded by error bar cuts (but not excluded by phase cuts). The model polarization comes from a fit with (unreduced) $\chi^2 = 332$ and parameters $\alpha = 59^\circ$ and $\zeta = 119^\circ$. The green solid line is the polarization for a model with $R_1 = 0.77R_{LC}$ and the black solid line is the polarization for a model with $R_2 = 0.38R_{LC}$. The red solid line is the model polarization of the two altitudes weighted by the model intensity. Empty circles mark the limiting phase of emission from open field lines with $\rho_{ypt} = 1R_{LC}$. A phase of zero is the point of closest encounter to the magnetic axis in the model.

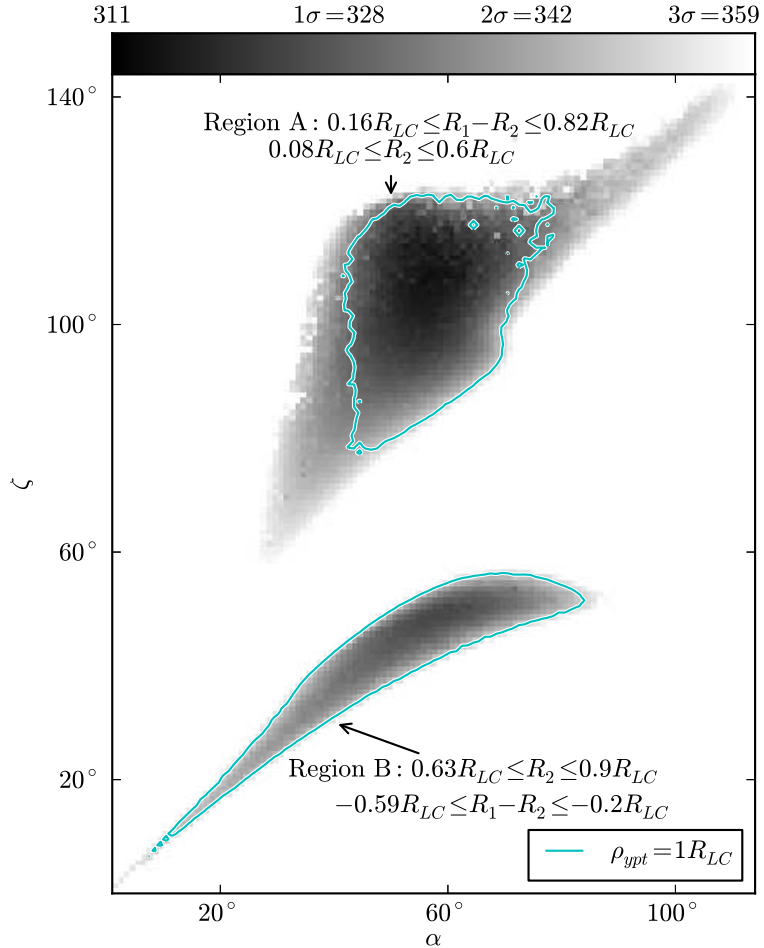


Figure 6.4: Map of (unreduced) χ^2 for PSR J0023+0923 in the α - ζ plane. Cyan contours mark 3σ from χ^2_{\min} for fits with $\rho_{ypt} = 1R_{LC}$. This contour contains the lowest values of χ^2 . The two regions of statistically acceptable fits have drastically different fit parameters.

where χ^2_2 is the χ^2 value for the model with the extra model parameters compared to the model that yields χ^2_1 , DOF_1 is the number of extra parameters, and DOF_2 is the DOF for the model with the extra parameters. The probability of exceeding this F is $\text{Prob} \sim 0$. This pulsar is an excellent example of how modeling with multiple altitudes can greatly improve χ^2_{\min} compared to the RVM. It is an example of how multiple altitudes can easily explain a non-90° orthogonal mode jumps since components of

emission with different altitudes allow for these non-90° mode jumps. Figure 6.3 shows the polarization position angle and intensity data overlaid with the best fit two altitudes plus the orthogonal mode jump model.

Further confirmation that this mode jump is between components from different altitudes in the magnetosphere comes from the curvature direction of the polarization position angle sweep between adjacent modes. The polarization sweep direction between components C_3 and C_4 is in the same direction as both the individual unweighted model curves (solid black and red lines). Such a direction of curvature is impossible for a mode jump between equal altitudes as discussed in Section 6.3.3. Also, such a direction of curvature is impossible in the RVM model which partially accounts for the poor fit.

Satisfactory fits exist for both $\rho_{\text{ypt}} = 1R_{\text{LC}}$ and $\rho_{\text{ypt}} < R_{\text{LC}}$. Figure 6.4 is the (unreduced) χ^2 map in the $\alpha-\zeta$ plane and the thin cyan contour represents the allowable area up to 3σ from χ^2_{\min} in which the emission comes only from the formal open field line region of the magnetic pole as defined by $\rho_{\text{ypt}} = 1R_{\text{LC}}$. The minimum χ^2 region is well within the $\rho_{\text{ypt}} = 1R_{\text{LC}}$ region as seen from Figure 6.4. Also Figure 6.3 shows a polarization position angle model that emits over the entire phase of emission seen in the data where the circles on the plot mark the phase defining the formal open zone for the two altitudes of emission used in the model.

In the $\alpha-\zeta$ plane, two islands of acceptable regions of $\chi^2 < 3\sigma$ arise as seen in Figure 6.4. Parameters and errors for each of these sections are reported separately in Table 6.2. The distinguishing parameter between these two regions is R_2 . For the region between $\zeta = 1^\circ$ and $\zeta = 56^\circ$, $R_2 = 0.63\text{--}0.90R_{\text{LC}}$. For the region between $\zeta = 58^\circ$ and $\zeta = 141^\circ$, $R_2 = R_{\text{ns}} = 0.08\text{--}0.61R_{\text{LC}}$. The region between $\zeta = 58^\circ$ and $\zeta = 141^\circ$ is more plausible for our model because it favors lower altitudes. Additionally, $\Delta R = R_1 - R_2$ for this region is positive and favors the cone–core model discussed previously (see Table 6.2 for values).

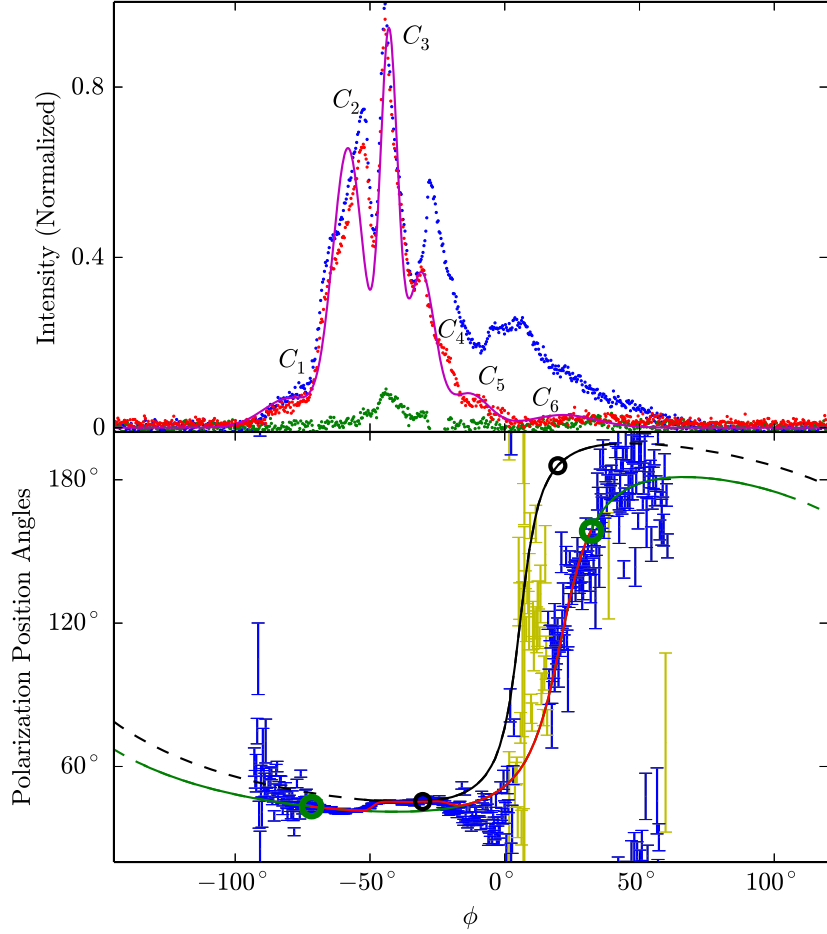


Figure 6.5: In the upper panel, blue points are total radio intensity data for 1.369 GHz, red points are linear polarization intensity data, and green points are circular polarization intensity data for PSR J1024–0719. The solid magenta line in the upper panel is the model linear intensity used in fitting. In the bottom panel, blue error bars are polarization position angles used in the fit and yellow error bars are polarization position angles excluded by error bar cuts (but not excluded by phase cuts). The model polarization comes from a fit with (unreduced) $\chi^2 = 3448$ and parameters $\alpha = 113^\circ$ and $\zeta = 108^\circ$. The green solid line is the polarization for a model with $R_1 = 0.22R_{LC}$ and the black solid line is the polarization for a model with $R_2 = 0.05R_{LC}$. The red solid line is the model polarization of the two altitudes weighted by the model intensity. Empty circles mark the limiting phase of emission from open field lines with $\rho_{ypt} = 1R_{LC}$. Solid lines mark the allowed emission phase for an effective open zone with $\rho_{ypt} = 0.24R_{LC}$ which is required for the model phase to cover the entire emission phase in the data. A phase of zero is the point of closest encounter to the magnetic axis in the model.

Table 6.3: Fit Parameters for PSR J1024–0719

(Unreduced)								
	DOF	χ^2_{\min}	α (°)	ζ (°)	R_1 (R_{LC})	R_2 (R_{LC})	ΔR (R_{LC})	$\Delta \rho$ (R_{LC})
RVM	397-4	8963	$98^{+1(+3)}_{-3(-4)}$	$87^{+1(+2)}_{-2(-2)}$
Region A 2 Alt 397-6	3409	$112^{+1(+2)}_{-1(-3)}$	$63^{+2(+5)}_{-3(-6)}$	$0.90^{+0.00(+0.00)}_{-0.02(-0.05)}$	$0.82^{+0.00(+0.01)}_{-0.02(-0.05)}$	$0.08^{+0.01(+0.01)}_{-0.00(-0.01)}$	$0.11^{+0.00(+0.01)}_{-0.01(-0.01)}$	$1.00^{+0.00(+0.00)}_{-0.02(-0.04)}$
Region B 2 Alt 397-6	3447	$113^{+1(+4)}_{-1(-4)}$	$108^{+1(+4)}_{-1(-4)}$	$0.22^{+0.01(+0.04)}_{-0.03(-0.05)}$	$0.05^{+0.00(+0.01)}_{-0.00(-0.00)}$	$0.17^{+0.01(+0.04)}_{-0.03(-0.05)}$	$0.04^{+0.01(+0.08)}_{-0.01(-0.03)}$	$0.24^{+0.00(+0.07)}_{-0.02(-0.04)}$

Note. — Errors reported without (with) parentheses are for 1σ (3σ) from χ^2_{\min} .

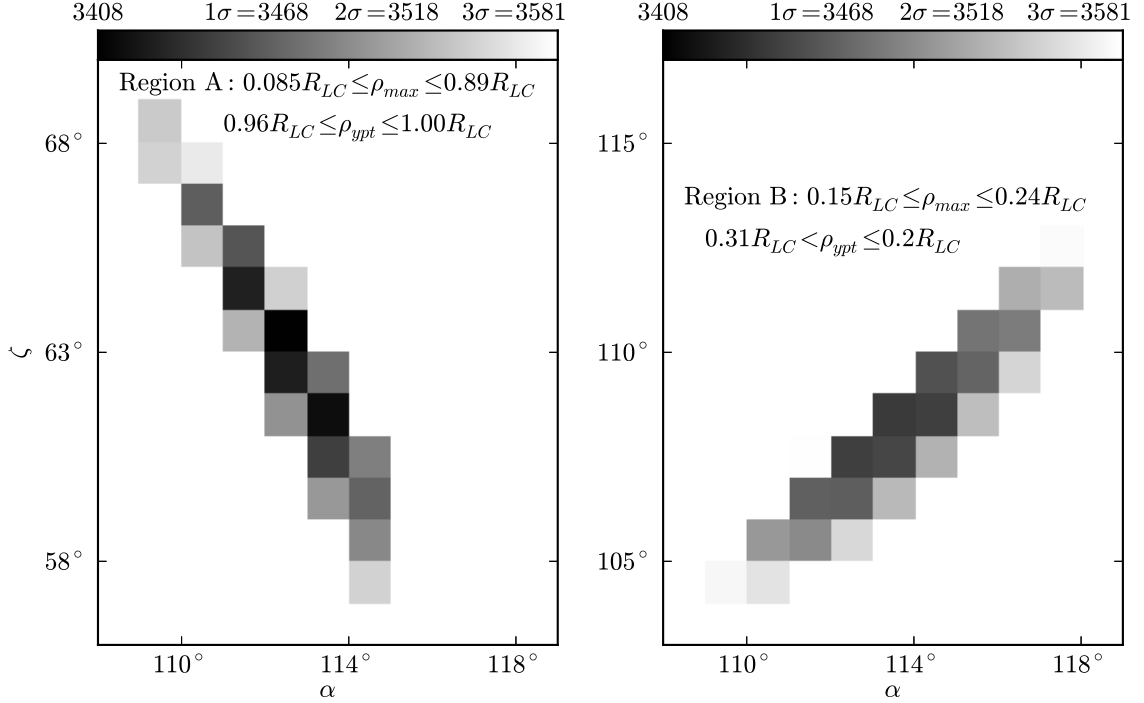


Figure 6.6: Map of (unreduced) χ^2 for PSR J1024–0719 in the α – ζ plane for Regions A and B. The regions vary drastically from one another in parameters although they are comparable in χ^2 . Both are very restrictive in their respective parameters.

6.5.2 PSR J1024–0719: Kinks with Multiple Altitudes

PSR J1024–0719 is another millisecond *Fermi*-detected pulsar ($P = 5.162$ ms). This pulsar fits reasonably well to the RVM (1.369 GHz data shown in Figure 6.5) although certain features in the polarization data are highly statistically significant and unexplained by the RVM. Most notably, a kink in the polarization occurs in the transition from intensity component C_2 to C_3 and from C_4 to C_5 (as labeled on Figure 6.5). Similar to PSR J0023+0923, this jump can be modeled using multiple altitudes, modeling the kink as the shift in altitude between the emission components. The error bars on this model are fairly small for the fit parameters (Table 6.3) since a limited number of parameter combinations make a sweep with this particular polarization difference with two heights. Additionally, the data contains the polarization at the point of closest encounter to the magnetic axis (the fastest change in the sweep) which also greatly constrains the fitting parameters. Overall, this pulsar is another excellent example of how using multiple altitudes can explain features not found in the RVM.

Similar to PSR J0023+0923, two regions arise in the α – ζ plane of the (unreduced) χ^2 map (see Figure 6.6) that are statistically acceptable. For the two regions, the altitudes are significantly different and are reported separately in Table 6.3.

In Region A, the ρ_{ypt} needs to be $0.22R_{\text{LC}} \leq \rho_{\text{ypt}} \leq 0.34R_{\text{LC}}$ in order to account for the full phase of the emission and remain within 3σ of χ^2_{\min} . Figure 6.5 displays the model polarization sweep from this region. The green and black circles represent the limiting phase of emission defined by the formal cap with $\rho_{\text{ypt}} = 1R_{\text{LC}}$. The solid lines mark the effective open zone emission for $\rho_{\text{ypt}} = 0.24R_{\text{LC}}$. Both sets of circles are well within the limiting phase of emission seen in the data. For most of the models within 3σ of χ^2_{\min} , the emission phase of the outer altitude (R_1 represented by the green line in Figure 6.5) controls the location of ρ_{ypt} . For Region A, $R_1 = 0.14\text{--}0.26R_{\text{LC}}$, $R_2 = 0.05\text{--}0.06R_{\text{LC}}$. The outer emission altitude, R_1 , is typically larger than the inner emission altitude, R_2 , which is consistent with a cone–core model similar to the two fit altitude parameters for the polarization position data from PSR J0023+0923

For Region B, the ρ_{ypt} is much higher than that in Region A but likewise so are R_1 and R_2 . Approximately $\rho_{\text{ypt}} = 0.96\text{--}1.0R_{\text{LC}}$, $R_1 = 0.85\text{--}0.9R_{\text{LC}}$, $R_2 = 0.77\text{--}0.83R_{\text{LC}}$.

Although ρ_{ypt} is much larger in Region B than in Region A, the altitude of emission is also close to R_{LC} resulting in a $\Delta\rho = \rho_{\text{ypt}} - \rho_{\text{max}}$ (the difference between the y-point cylindrical distance needed to open up the field lines to the appropriate amount to accommodate the emission phase in the data and the maximum cylindrical distance of the emission within this phase) similar to that of Region A. Additionally, $\Delta\rho$ is relatively small (see Table 6.3). This is problematic because we expect emission this close to the light cylinder to resemble a force-free model and to be dictated by physics that we do not include in the vacuum model. To explain the phase of emission seen in the data using this model, one must either push the altitude up to extreme heights or accept ρ_{ypt} much smaller than $1R_{\text{LC}}$.

PSR J1024–0719 is modeled with two altitudes, one altitude component inside the other in terms of phase, making it a good candidate for the cone–core model. The parameter $\Delta R = R_1 - R_2$ (where R_1 is the altitude associated with component C_1 , C_2 , C_5 , and C_6 and R_2 is the altitude associated with C_3 and C_4) should be positive in the case of a cone–core model. Table 6.3 shows this value to be positive for both Regions A and B. Further, to 3σ , these values are positive and radio modeling of PSR J1024–0719 polarization is consistent with the cone–core model.

For the RVM (unreduced) $\chi^2_{\text{min}} = 8963$ and for the two-altitude model (unreduced) $\chi^2_{\text{min}} = 3408$. By including two physically motivated parameters, the χ^2_{min} is decreased by a factor of three. The F -test between the RVM and the two-altitude model gives $F = 318.66$, $\text{DOF}_1 = 2$, and $\text{DOF}_2 = 391$. The probability of exceeding this F is $\text{Prob} \sim 0$. By these statistical measures, a two-altitude model is clearly better than the RVM.

6.5.3 PSR J1057–5226: Y-Point and Finite Altitude

PSR J1057–5226 is a relatively young pulsar ($P = 197.11$ ms) that has had its radio polarization position angle sweep fit in the literature with the RVM (Weltevrede & Wright, 2009). Here we fit the latest polarization data for PSR J1057–5226 at 1.369 GHz with the RVM plus our own finite-altitude model. Polarization and intensity data for PSR J1057–5226 is plotted in Figure 6.7. First note that we are unable to

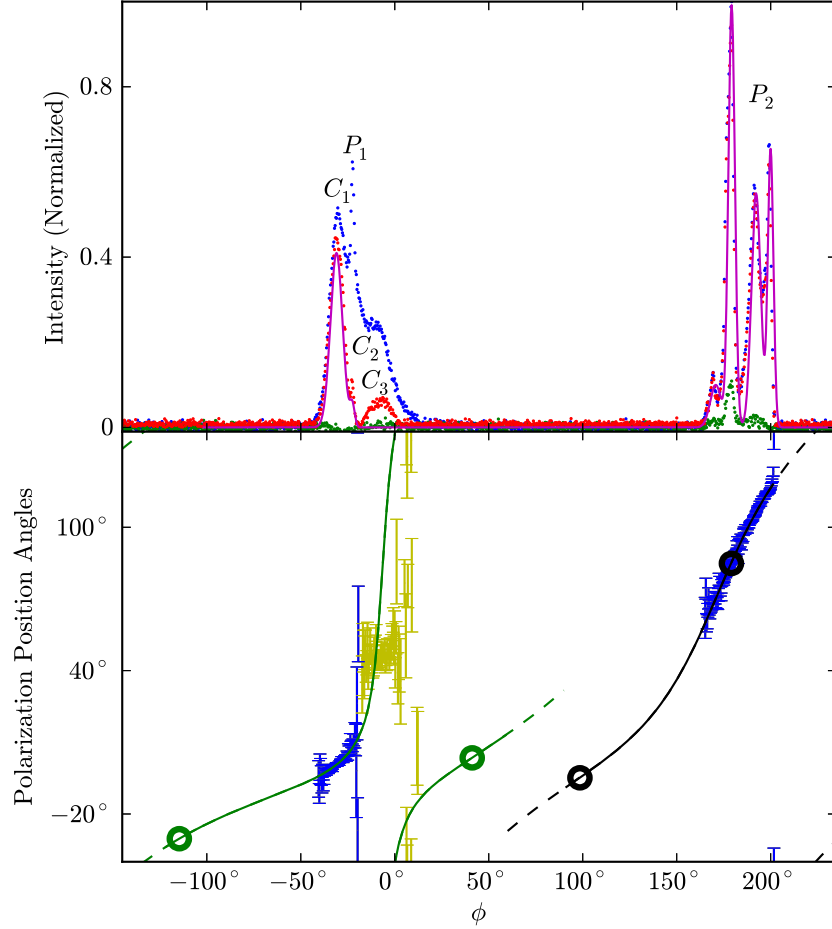


Figure 6.7: In the upper panel, blue points are total radio intensity data for 1.5 GHz, red points are linear polarization intensity data, and green points are circular polarization intensity data for PSR J1057–5226. The solid magenta line in the upper panel is the model linear intensity used in fitting. In the bottom panel, blue error bars are polarization position angles used in the fit and yellow error bars are polarization position angles excluded from the fit because of phase cuts (see text). The model polarization comes from a fit with (unreduced) $\chi^2 = 289$ and parameters $\alpha = 77^\circ$ and $\zeta = 30^\circ$. The green solid line is the polarization for a model with $R_1 = 0.58R_{LC}$ and the black solid line is the polarization for a model with $R_2 = 0.63R_{LC}$. Empty circles mark the limiting phase of emission from open field lines with $\rho_{ypt} = 1R_{LC}$. Solid lines mark allowed emission phase for an effective open zone with $\rho_{ypt} = 0.71R_{LC}$ ($\Delta\rho = 0.49R_{LC}$) which is required for the model phase to cover the entire emission phase in the data. A phase of zero is the point of closest encounter to the magnetic axis in the model.

Table 6.4: Fit Parameters for PSR J1057–5226

(Unreduced)								
DOF	χ^2_{\min}	α (°)	ζ (°)	R_1 (R_{LC})	R_2 (R_{LC})	$\Delta\rho$ (R_{LC})	ρ_{\max} (R_{LC})	ρ_{ypt} (R_{LC})
RVM 166-4	325	$77^{+0(+1)}_{-1(-1)}$	$70^{+0(+0)}_{-0(-0)}$
1 Alt 166-5	282	$76^{+2(+2)}_{0(-1)}$	$64^{+5(+5)}_{-34(-35)}$	$0.19^{+0.43(+0.46)}_{-0.12(-0.13)}$
2 Alt 166-6	281	$69^{+14(+26)}_{-4(-9)}$	$64^{+5(+6)}_{-37(-39)}$	$0.12^{+0.72(+0.72)}_{-0.06(-0.12)}$	$0.31^{+0.59(+0.59)}_{-0.29(-0.31)}$	$0.15^{+0.32(+0.40)}_{-0.15(-0.15)}$	$0.31^{+0.36(+0.52)}_{-0.25(-0.28)}$	$0.46^{+0.54(+0.54)}_{-0.40(-0.40)}$

Note. — Errors reported without (with) parentheses are for 1σ (3σ) from χ^2_{\min} .

explain the polarization position angles associated with C_3 as labeled in Figure 6.7 with either the RVM or our current model. This portion of the polarization sweep had not appeared in the previous RVM fitting papers due to poor signal-to-noise. Although we will not attempt to explain this component here, we hope to explore modifications to our current model that will explain this component in future work.

Ignoring the polarization position angles associated with C_3 for the moment, unlike PSR J0023+0923 and PSR J1024–0719, PSR J1057–5226 does not have any compelling features to indicate mode jumps or multiple altitudes. The χ^2_{\min} for the RVM even gives a reasonable fit for the number of degrees of freedom (DOF, Table 6.3). Even so, by fitting to a finite altitude and finite multiple altitudes, we can significantly decrease the χ^2_{\min} and open the parameter space. Further, Weltevrede & Wright (2009) were forced to conclude that emission comes from outside the formal open zone cap due to the large emission phase of PSR J1057–5226. Here we seek a more physical model using a finite altitude and $\rho_{\text{ypt}} < R_{LC}$.

We can model the data with $\rho_{\text{ypt}} = 1R_{LC}$ within 1σ of χ^2_{\min} but this requires pushing the model to the highest allowed altitudes. On the other hand, low altitudes are also permitted but require low ρ_{ypt} in order for the models to emit in the phase observed in the data. The true fit likely lies somewhere between the extremes. A strong correlation exists between α , ζ , R_1 , and R_2 such that if one has an estimated range for R_1 or R_2 , the acceptable α – ζ models would be significantly decreased.

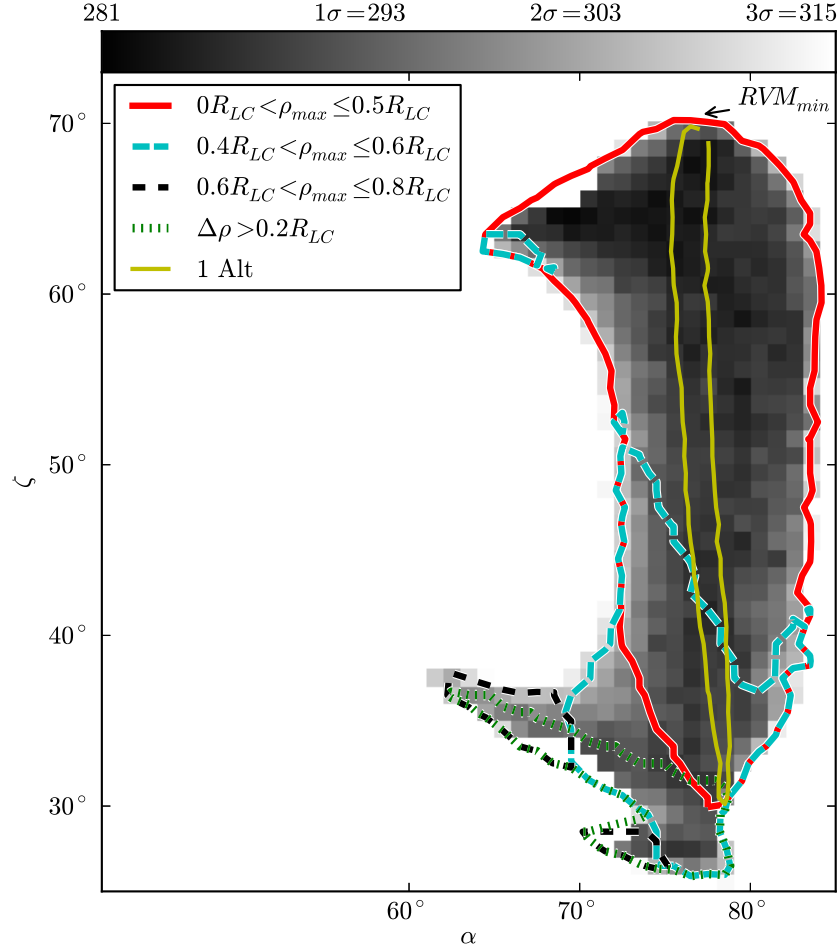


Figure 6.8: Map of (unreduced) χ^2 for PSR J1057–5226 in the α – ζ plane with 3σ contours for sets of ρ_{max} ranges, the single-altitude model fit, and $\Delta\rho > 0.2R_{LC}$. The best fit for the RVM is also indicated on the map. The best fit using the RVM is quite different from the best fit using finite altitude and restrictions from the phase of emission seen in the data ($\Delta\rho > 0.2R_{LC}$).

Red, cyan, and black contours on Figure 6.8 are 3σ contours from χ^2_{\min} of different ranges of ρ_{max} , the maximum cylindrical distance of the emission within the emission phase for the model. These contours exemplify the correlation between altitude and α – ζ pairs in a single parameter. Further, fits with smaller ρ_{max} are more physically

Table 6.5: Fit Parameters for PSR J1744–1134

(Unreduced)							
	DOF	χ^2_{\min}	α (°)	ζ (°)	R_1 (R_{LC})	R_2 (R_{LC})	$\Delta\rho$ (R_{LC})
RVM	209-4	355	$74^{+0(+1)}_{-2(-4)}$	$97^{+0(+1)}_{-2(-3)}$
2 Alt no jump	209-6	311	$76^{+2(+6)}_{-11(-15)}$	$60^{8(+84)}_{-18(-26)}$	$0.68^{+0.09(+0.18)}_{-0.12(-0.62)}$	$0.70^{+0.20(+0.20)}_{-0.03(-0.64)}$	$0.06^{+0.00(+0.33)}_{-0.04(-0.06)}$
2 Alt jump	209-6	314	$92^{+2(+4)}_{-53(-70)}$	$57^{+76(+79)}_{-8(-32)}$	$0.87^{+0.03(+0.03)}_{-0.76(-0.81)}$	$0.88^{+0.02(+0.02)}_{-0.24(-0.44)}$	$0.05^{+0.24(+0.27)}_{-0.05(-0.05)}$
1 Alt single pole	209-5	310	$66^{+5(+15)}_{-4(-7)}$	$85^{+3(+35)}_{-36(-39)}$	$0.65^{+0.07(+0.20)}_{-0.27(-0.54)}$...	$0.36^{+0.09(+0.12)}_{-0.35(-0.47)}$
2 Alt single pole	209-6	309	$66^{+11(+17)}_{-22(-36)}$	$85^{+24(+32)}_{-53(-60)}$	$0.65^{+0.14(+0.25)}_{-0.55(-0.59)}$	$0.59^{+0.31(+0.31)}_{-0.23(-0.52)}$	$0.37^{+0.19(+0.30)}_{-0.37(-0.37)}$
							$1.00^{+0.00(+0.00)}_{-0.56(-0.93)}$

Note. — Errors reported without (with) parentheses are for 1σ (3σ) from χ^2_{\min} .

likely but so is larger $\Delta\rho$ such as $\Delta\rho > 0.2R_{LC}$ (3σ dashed green contours on Figure 6.8). As such, one might expect the most physically plausible fits to fall within the green and cyan contours.

The yellow contour is the 3σ contour from χ^2_{\min} of a single-altitude model. Going from one altitude to two altitudes does not greatly improve χ^2_{\min} . Adding the additional parameter does allow for a wider variety of geometric configurations (α and ζ) which could be of importance when comparing to multi-wavelength results.

For the RVM (unreduced) $\chi^2_{\min} = 325$ and for the two-altitude model (unreduced) $\chi^2_{\min} = 281$ (see Table 6.4). The F -test between the RVM and the two-altitude model gives $F = 12.50$, $DOF_1 = 2$, and $DOF_2 = 160$. The probability of exceeding this F is $P = 8.78 \times 10^{-6}$. Comparing the RVM to the single-altitude model ($\chi^2_{\min} = 282$), the probability of exceeding $F = 24.55$ is $Prob = 1.82 \times 10^{-6}$. Comparing the single-altitude model to the two-altitude model, the probability of exceeding $F = 0.57$ is $Prob = 4.52 \times 10^{-1}$.

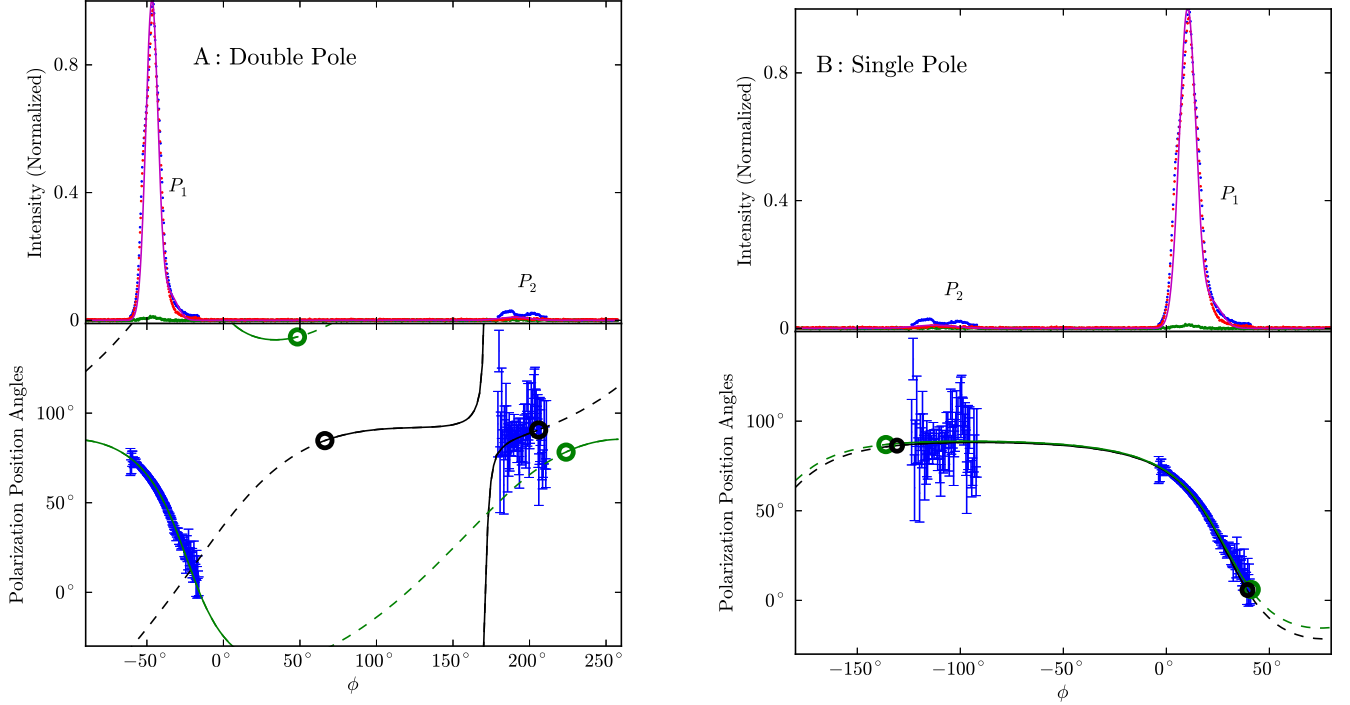


Figure 6.9: In the upper panels, blue points are total radio intensity data for 1.369 GHz, red points are linear polarization intensity data, and green points are circular polarization intensity data for PSR J1744–1134. The solid magenta line in the upper panels is the model linear intensity used in fitting. In the bottom panels, blue error bars are polarization position angles used in the fit. For panel (A), the model polarization comes from a double magnetic pole model with (unreduced) $\chi^2 = 342$, $\alpha = 82^\circ$, and $\zeta = 39^\circ$. The green line is the polarization for a model with $R_1 = 0.78R_{LC}$ and the black line is the polarization for a model with $R_2 = 0.72R_{LC}$. The emission phase from the data for these model parameters requires $\rho_{ypt} = 0.96R_{LC}$ as marked on the plot with the solid lines. For panel (B), the model polarization comes from a single magnetic pole model with (unreduced) $\chi^2 = 317$, $\alpha = 66^\circ$, and $\zeta = 85^\circ$. The green solid line is the polarization for a model with $R_1 = 0.65R_{LC}$ and the black solid line is the polarization for a model with $R_2 = 0.59R_{LC}$. The emission phase from the data is covered with $\rho_{ypt} = 1R_{LC}$ for these model parameters. Empty circles mark the limiting phase of emission from open field lines with $\rho_{ypt} = 1R_{LC}$. A phase of zero is the point of closest encounter to the magnetic axis in the model.

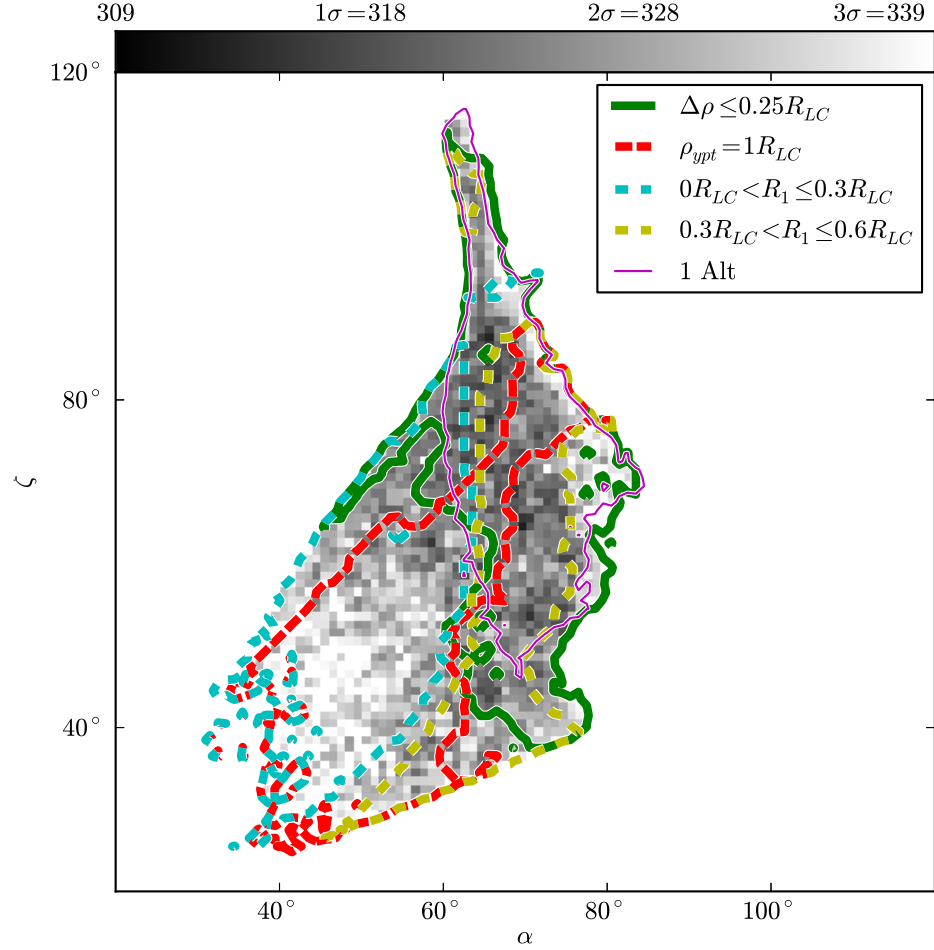


Figure 6.10: Map of (unreduced) χ^2 for PSR J1744–1134 in the α – ζ plane for a single magnetic pole model with 3σ contours for two R_1 ranges to show correlation between α , ζ , and altitude for $\Delta\rho \leq 0.25R_{LC}$ (the more approximate models) and $\rho_{ypt} = 1R_{LC}$ (the less approximate models), and for the single-altitude model which lies mostly in the physically inaccurate contour of $\Delta\rho \leq 0.25R_{LC}$ and therefore argues for a two-altitude model.

6.5.4 PSR J1744–1134: Multiple Altitudes with Single Versus Double Pole

PSR J1744–1134 is yet another millisecond pulsar detected in γ -rays by *Fermi*. Similar to PSR J1057–5226, the polarization of PSR J1744–1134 fits well to the RVM.

But even with the consideration that the star surface is $\sim 0.06R_{LC}$ based on period, the emission zone of a vacuum dipole model with emission from both poles is not large enough to accommodate the range of the emission in phase seen in the data. In the vast majority of fits, the cylindrical distance between the edge of the open zone required and the maximum cylindrical emission point ($\Delta\rho$) is smaller than $0.2R_{LC}$. We considered a two-pole model with and without an orthogonal mode jump between the polarization position angles associated with P_1 and P_2 as labeled on Figure 6.9. Results for the fits are reported in Table 6.5.

The peaks, P_1 and P_2 , are separated by $\sim 103^\circ$ – 134° ; thus another possibility is that the emission is not from two magnetic poles but a single broad pulse. Interestingly, with this assumption, models exist within the 1σ multidimensional contour with $\rho_{ypt} = 1R_{LC}$. Figure 6.10 shows the α – ζ maps of (unreduced) χ^2 for the single broad pulse model. The red contour shows the 3σ range with the assumption that $\rho_{ypt} = 1R_{LC}$. Additionally, the green contour is the 3σ contour with a $\Delta\rho \leq 0.25R_{LC}$ cut and the thin magenta line is the 3σ contour if $R_1 = R_2$; these two contours strongly overlap which makes us slightly favor models where $R_1 \neq R_2$. Quite a range of altitudes falls within the 3σ contours and there is a strong correlation between R_1 and α and ζ . We also plotted two rough ranges of R_1 on the α – ζ map to illustrate this correlation. Overall, the polarization position angles associated with P_2 are very noisy, which translates into noisy χ^2 surfaces. To decrease this noise, we applied a $0^\circ 5$ Gaussian smoothing kernel to the map and contours. Additionally, Figure 6.9, panel (B) shows the polarization sweep derived from a single magnetic pole model with $\alpha = 66^\circ$ and $\zeta = 85^\circ$.

For single-pole and double-pole models, fit parameters and errors are reported in Table 6.5. Overall, adding a finite altitude, whether using a single-pole or two-pole model, significantly decreases the χ^2_{min} which can be shown statistically using an F -test. The (unreduced) $\chi^2_{min} = 355$ for the RVM and $DOF_1 = 2$, and $DOF_2 = 203$ for the F -test. For the single magnetic pole emission (unreduced $\chi^2_{min} = 309$), the probability of exceeding the resulting F is $P = 7.63 \times 10^{-7}$; for the two magnetic pole model without an orthogonal mode jump (unreduced $\chi^2_{min} = 311$), the probability of exceeding the resulting F is $P = 1.47 \times 10^{-6}$; for the two magnetic pole model with

an orthogonal mode jump (unreduced $\chi^2_{\min} = 314$), the probability of exceeding the resulting F is $P = 3.89 \times 10^{-6}$.

6.5.5 PSR J1420–6048: Multiple Altitudes and Interstellar Scattering

The millisecond pulsar ($P = 68$ ms) PSR J1420–6048 has been studied previously (Roberts et al. 2001; Weltevrede et al. 2010a). The RVM fit in these papers estimated $\alpha > 145^\circ$ and $\zeta - \alpha \sim 0^\circ 5$ (the angle convention used in these papers is different from that used in this paper and they must be converted. See Everett & Weisberg 2001 for an explanation and the conversion formula). This fit is consistent with our results of fitting with the RVM. Since the effects of interstellar scattering scales to the -4 power in frequency (Lang, 1971), comparing 10 cm data to 20 cm data reveals that the polarization and intensity profile of PSR J1420–6048 have signs of scattering (Figure 6.11). In particular, note the widening of the intensity profile and the flattening of the polarization sweep at the trailing edge of the intensity components for the 20 cm data compared to the 10 cm data. The scattering time constant calculated using the Cordes & Lazio (2002) model is $\tau = 6.5 \times 10^{-2}$ ms. The ratio of τ to period (and also the value of dispersion measure or DM) is far larger than that for any of the other pulsars considered in this paper yet this value is still smaller than what would cause the scattering seen by comparing the 10 cm and 20 cm data. Because of this discrepancy, τ is a fit parameter in analyzing polarization data of PSR J1420–6048.

When fitting the 10 cm data ($\tau \sim 0$), the best fit non-scattered model is $\alpha = 100^{+34(+79)}_{-63(-97)}^\circ$, $\zeta = 39^{+116(+140)}_{-25(-38)}^\circ$, and $R = 0.64^{+0.26(+0.26)}_{-0.64(-0.64)} R_{LC}$ where errors without (with) parentheses are 1σ (3σ) errors. The error bars on these values are large due to the low signal-to-noise in the polarization position angles and the exact parameter values at χ^2_{\min} are less valuable than the full range defined by these error bars. When fitting the 20 cm polarization data, with a small scattering time ($\tau = 0.1$ ms), the best fit non-scattered model is $\alpha = 175^{+2(+3)}_{-6(-18)}^\circ$, $\zeta = 177^{+1(+1)}_{-4(-14)}^\circ$, and $R = .37^{+0.10(+0.50)}_{-0.33(-0.37)} R_{LC}$ which is drastically different than the results for the 10 cm data. In fact the 3σ

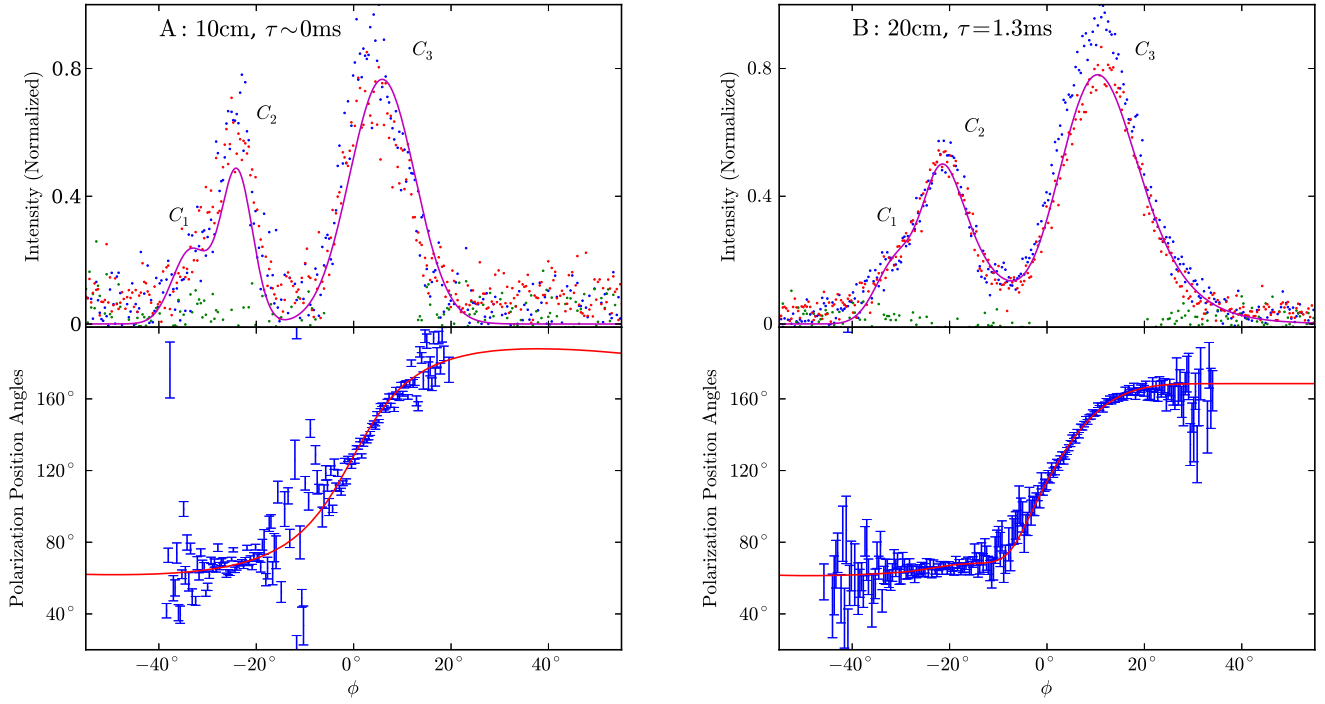


Figure 6.11: In the upper panel, blue points are total radio intensity data, red points are linear polarization intensity data, and green points are circular polarization intensity data for PSR J1420–6048. The solid magenta line in the upper panel is the model linear intensity used in fitting. In the bottom panel, blue error bars are polarization position angles used in the fit. The model polarization comes from a fit with (unreduced) $\chi^2 = 435$ (joint fit with data from both 10 cm and 20 cm) and parameters $\alpha = 120^\circ$, $\zeta = 150^\circ$, and $R_1 = 0.53R_{LC}$ weighted by the model intensity. Panel (A) shows the 10 cm intensity and polarization position angle data and the model with scattering time $\tau \sim 0$ ms. Panel (B) is the 20 cm intensity and polarization position angle data and the model with scattering time $\tau = 1.3$ ms. The $\rho_{ypt} < 1R_{LC}$ constraints lie beyond the phase plotted. A phase of zero is the point of closest encounter to the magnetic axis in the model.

multi-dimensional contours as measured from the individual χ^2_{\min} do not overlap.

Physically, we expect that two different frequencies should come from different altitudes but we are making the assumption that they are closely spaced and any systematic error from this assumption is overpowered by the statistic error. A combined

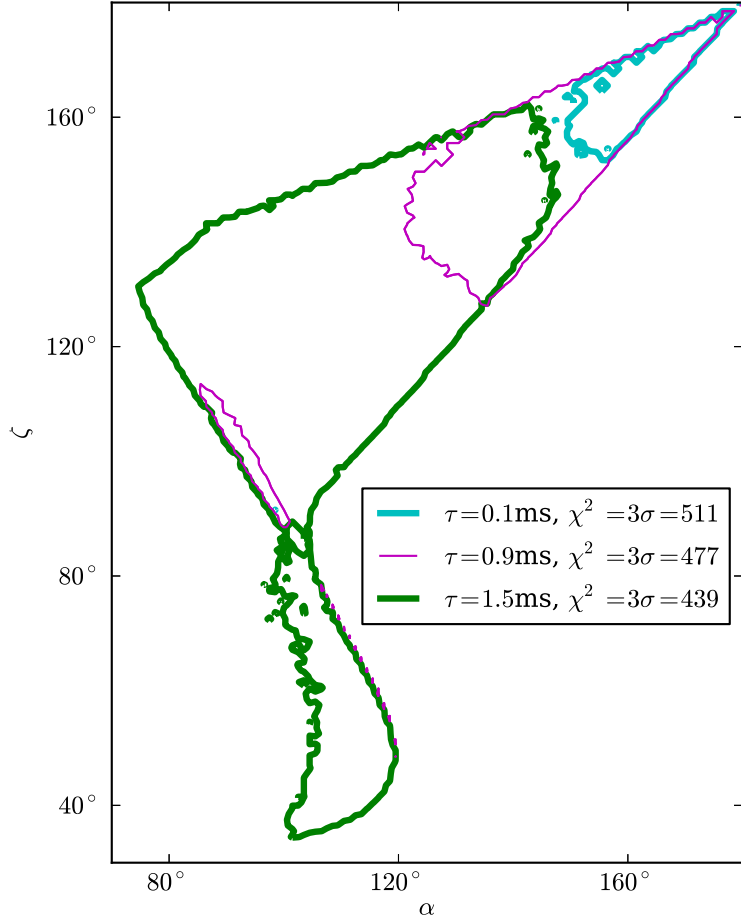


Figure 6.12: Contours of the joint (unreduced) χ^2 set to 3σ in the α - ζ plane for modeling of the polarization data in 10 cm and 20 cm of PSR J1420–6048. Different colors represent fits to different τ , scattering time. Increasing scattering time widens the acceptable fit parameters, decreases the acceptable α values, and decreases χ^2_{\min} .

χ^2 from the two sets of data (10 cm and 20 cm) at low scattering constants results in a minimum region similar to the minimum of fitting 20 cm alone (see Figure 6.12, cyan contours $\tau = 0.1$ ms). A combined χ^2 from the two sets of data at an intermediate scattering constant results in two distinct minimum regions (see Figure 6.12, magenta contours $\tau = 0.9$ ms). A combined χ^2 from the two sets of data at high scattering constants results in a single minimum region (see Figure 6.12, green contours $\tau = 1.5$ ms). In the combined χ^2 , we assume that the altitudes are the same. Fitting the

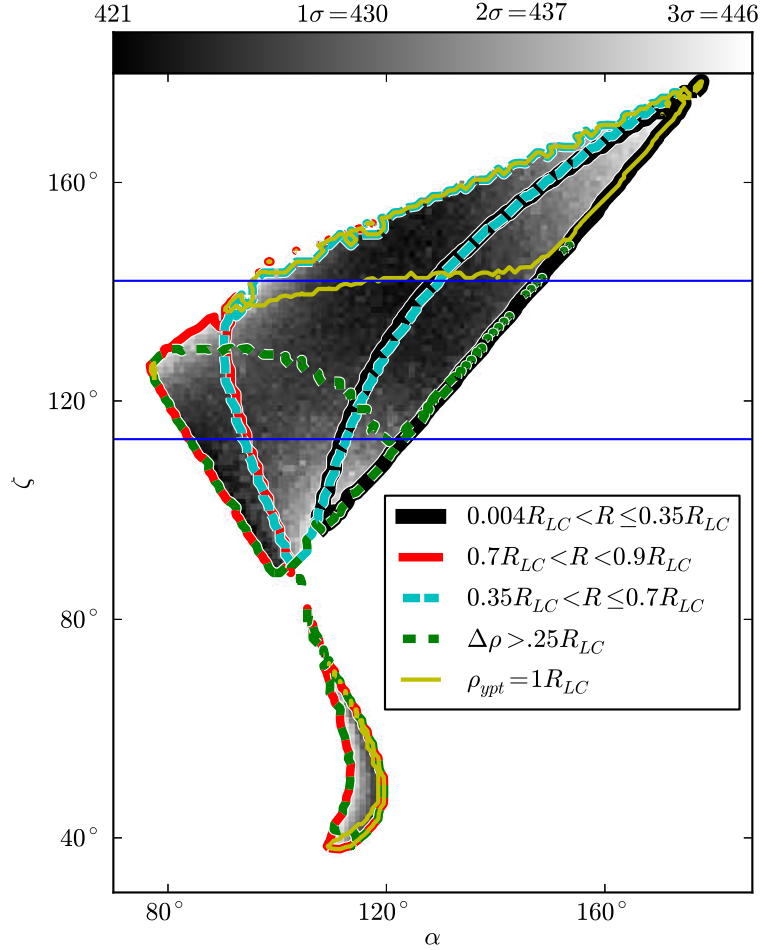


Figure 6.13: Map of the joint (unreduced) χ^2 for polarization data in 10 cm and 20 cm of PSR J1420–6048 in the α – ζ plane. The model has a scattering constant of $\tau = 1.3$ ms. Contours of 3σ are for three ranges of R to show the correlation between α , ζ , and altitude and for $\Delta\rho \leq 0.25R_{LC}$ (the most physically inaccurate models) and $\rho_{ypt} = 1R_{LC}$ (the most physically accurate models). Horizontal blue lines indicate the region favored by X-ray torus fitting (Section 6.5.5).

data with different scattering constants gives drastically different results. The larger the scattering constant, the better the χ^2_{\min} . We can place a practical limit on the scattering because a large scattering constant results in a distorted intensity profile which is not seen in the data. Therefore, we did not fit with a scattering constant

larger than $\tau = 1.5$ ms since scattering constants much larger than this distort the intensity profile. In Figure 6.12, as the scattering constant increases, the two islands of best fit χ^2 seen at the lowest scattering constant merge into a single χ^2 surface. Because of the drastic decrease in χ^2_{\min} from increasing the scattering constant and the merging of the χ^2_{\min} , the true scattering constant is $\tau \sim 1.1\text{--}1.5$ ms. Additionally, we report α , ζ , and R in Table 6.6 for select values of τ .

Further, the error bars on the DM are larger than the shift that we expect from including scattering when comparing the two different wavelengths. The DM reported in Weltevrede et al. (2010a) is 360^{+2}_{-2} cm $^{-3}$ pc and the correction to the DM from our fitting of scattering time constants with error bars are reported in Table 6.6. The ΔDM values are all within the 2 cm $^{-3}$ pc error bars of the original DM up to 3σ from χ^2_{\min} .

As τ increases, the best fit values of α and ζ shift and the 3σ range for these values increases drastically. Also, the χ^2_{\min} values decrease statistically significantly from $\tau = 0.1$ ms to $\tau = 1.5$ ms. For $\tau = 1.5$ ms, $3\sigma = 439$ from χ^2_{\min} . The χ^2_{\min} for $\tau = 0.1$ ms is not within this 3σ of the $\tau = 1.5$ ms fit.

Figure 6.13 is the (unreduced) χ^2 map for $\tau = 1.3$ ms. The black, cyan, and red contours are for 3σ contours at various altitude ranges, illustrating that although the allowed range of altitudes is large for this pulsar, knowledge of α and ζ could greatly decrease this range because of the correlation between R and $\alpha\text{--}\zeta$ pairs. A large number of fits could be additionally excluded if cuts of $\Delta\rho$ are applied. The green dashed contour corresponds to $\Delta\rho < 0.25R_{\text{LC}}$. If only fits up to 3σ with $\rho_{\text{ypt}} = 1R_{\text{LC}}$ are considered, only fits within the yellow contour on Figure 6.13 would be allowed.

X-Ray Torus of PSR J1420–6048

Young pulsars appear to produce relativistic plasma confined to the spin equator. When this wind shocks the e^+/e^- pitch angle scatter and synchrotron radiate, producing an equatorial torus. Since the bulk flow in the region is mildly relativistic, with expected bulk velocity $\beta \sim 0.3\text{--}0.7$, this torus can be Doppler brightened on the side emerging from the plane of the sky. In several cases, there seems to be a secondary

Table 6.6: Fit Parameters for PSR J1420–6048

		τ (Unreduced)			
DOF	(ms)	χ^2_{\min}	α ($^\circ$)	ζ ($^\circ$)	R (R_{LC})
356-5	.1	480	$175^{+3(+4)}_{-15(-77)}$	$177^{+1(+2)}_{-13(-86)}$	$0.37^{+0.10(+0.52)}_{-0.31(-0.37)}$
356-5	.9	448	$166^{+13(+13)}_{-76(-81)}$	$169^{+10(+10)}_{-104(-119)}$	$0.26^{+0.64(+0.64)}_{-0.26(-0.26)}$
356-5	1.3	421	$126^{+22(+51)}_{-46(-50)}$	$153^{+9(+25)}_{-113(-115)}$	$0.52^{0.38(+0.38)}_{-0.52(-0.52)}$
356-5	1.5	415	$105^{+27(+42)}_{-28(-31)}$	$140^{+14(+22)}_{-102(-106)}$	$0.58^{+0.32(+0.32)}_{-0.44(-0.58)}$

Note. — Errors reported without (with) parentheses are for 1σ (3σ) from χ^2_{\min} .

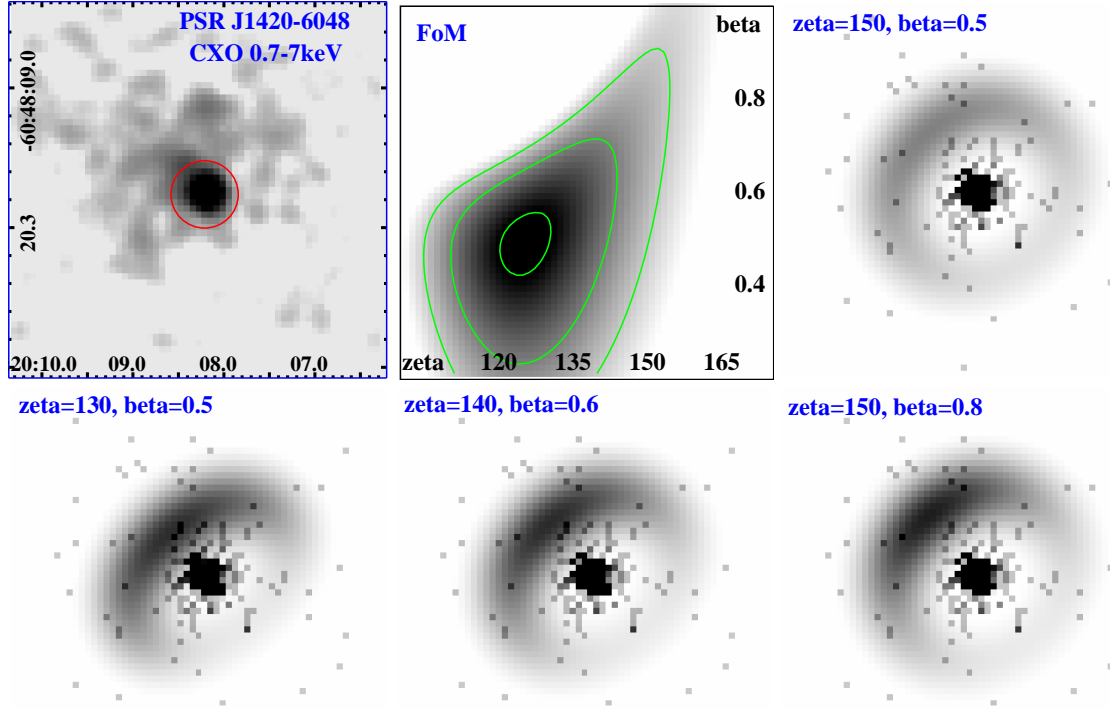


Figure 6.14: X-ray pulsar wind nebula of PSR J1420–6048. Upper left shows the pulsar wind nebula structure, while the figure of merit (FoM) panel show contours of the fit in the ζ - β plane. The other panels show the dependence of the torus shape and brightness on these parameters (see Section 6.5.5).

shock along the polar axis producing polar “jets” in the pulsar wind nebula, with the jet on the opposite side of the Doppler-enhanced torus rim, being Doppler boosted. The Crab and Vela pulsars provide classic examples of this relativistic torus–jet geometry.

Ng & Romani (2004) and Ng & Romani (2008) showed how fits to *Chandra* X-ray images of such tori can provide useful constraints on the pulsar spin orientation. For PSR J1420–6048, we obtained a 90 ks *Chandra* ACIS observation (ObSID 12545). We combined this exposure with a 10 ks archival observation (ObsID 2794), removing the spacecraft dither and reprocessing the data giving sub-pixel (EDSER) event positioning, to obtain the best possible image of the compact PWN surrounding this energetic pulsar. Figure 6.14 (upper left) shows a lightly smoothed 0.7–7 keV *Chandra* image of the combined exposure, with a logarithmic stretch. The pulsar point source is in the red circle. Unfortunately, this pulsar does not show a striking torus structure, so unlike several other young pulsars, we cannot obtain a high-quality, model-independent measurement of its spin geometry. Still, the diffuse counts do show a semi-circular arc of flux, trailing off to the NE. If we interpret this as an equatorial torus, we can apply the methods of Ng & Romani (2008) to constrain the spin orientation. A few parameters are well measured: the position angle of the symmetry axis ($\Psi = 40^\circ \pm 3^\circ$, measured N through E) and the radius of the “torus” ($7'' \pm 1''/5$) are reasonably constrained. In unsmoothed images there is some evidence for a polar component on a $1''$ – $2''$ scale, but this is not well measured. The parameter of greatest interest to the present study is the inclination ζ of the pulsar spin to the Earth line-of-sight. To minimize sensitivity to point source flux and possible jet structure we fit outside of the $5''$ radius red circle dominated by the central point source. The main constraint comes from the shape and brightness ratio between the front and back sides of the torus. The second panel of Figure 6.14 shows that this introduces substantial co-variance between ζ and the bulk β of the post-shock flow. The best fits are near typical $\beta \sim 0.5$, with $\zeta \approx 125^\circ$. This is in considerable tension with the larger ζ preferred by the polarization position angle fits to models with small scattering times; we only reach $\zeta \approx 155^\circ$ with a rather aphysical $\beta \sim 0.9$. This co-variance is visible along the bottom row of torus (+point spread function+jet) models, which

Table 6.7: Fit Parameters for PSR J2124–3358

	DOF (Unreduced)	χ^2_{\min}	α ($^\circ$)	ζ ($^\circ$)	R_1 (R_{LC})	R_2 (R_{LC})	R_3 (R_{LC})
RVM 536-4	2331	$2^{+3(+7)}_{-0(-0)}$	$5^{+8(+19)}_{-0(-0)}$
3 Alt 536-7	773	$2^{+7(+12)}_{-1(-1)}$	$2^{+7(+12)}_{-1(-1)}$	$0.05^{+0.01(+0.03)}_{-0.00(-0.00)}$	$0.40^{+0.01(+0.02)}_{-0.01(-0.03)}$	$0.55^{+0.02(+0.04)}_{-0.01(-0.03)}$	

Note. — Errors reported without (with) parentheses are for 1σ (3σ) from χ^2_{\min} .

show that as ζ increases from 130° to 150° , the post-shock Lorentz factor must grow to maintain a reasonable intensity ratio between the “front” and “back” sides of the torus. The last panel on the top row shows how with $\zeta = 150^\circ$, $\beta = 0.5$, the torus is too face-on and uniform for a good fit to the data. Thus the X-ray pulsar wind nebula structure agrees with the γ -ray pulse shape, where the observed peak separation $\Delta = 0.31$ implies $\zeta \approx 110^\circ$ – 140° , with the largest ζ only available in the two-pole caustic picture (Romani & Watters, 2010), which tends to produce too much unpulsed emission.

Polarization position angle fits with scattering constant $\tau = 1.3$ ms as discussed in Section 6.5.5 favor ζ between 120° and 150° as can be seen from the color map of Figure 6.13. The measurement of ζ from the X-ray torus fit indicates ζ between 113° and 142° (from the contours of 2σ). The horizontal blue lines on Figure 6.13 mark the region of 2σ set by the X-ray torus fitting. By assuming a scattering constant, we not only reconcile the fits of 10 cm and 20 cm data but also find consistency between radio polarization position angle fits and X-ray torus fits.

6.5.6 PSR J2124–3358: A Complex Example

PSR J2124–3358 is yet another millisecond pulsar ($P = 4.931$ ms). Plotted in Figure 6.15 is the polarization and intensity profile for this pulsar at 1.369 GHz. The pulsar PSR J2124–3358 has emission at practically all phases of the period. The polarization position angles are complicated but can be greatly simplified by assuming orthogonal mode jumps at the appropriate components. We assumed that the polarization associated with components C_1 , C_2 , and C_6 are orthogonal to the polarization

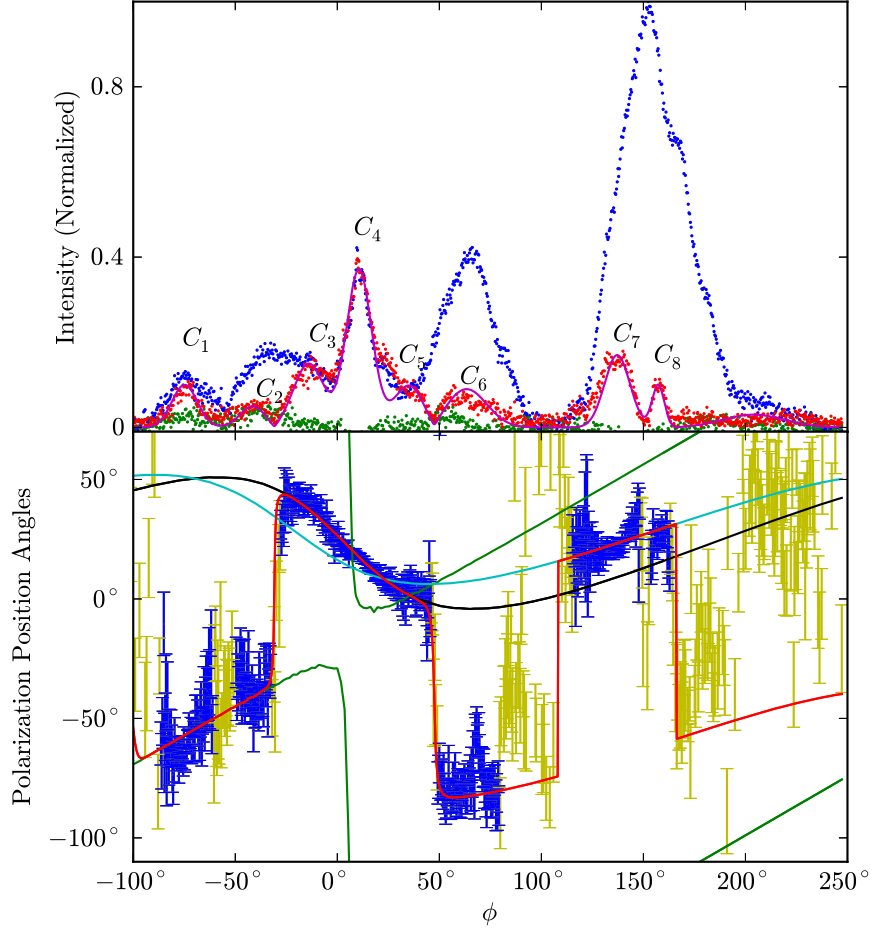


Figure 6.15: In the upper panel, blue points are total radio intensity data for 1.369 GHz, red points are linear polarization intensity data, and green points are circular polarization intensity data for PSR J2124–3358. The solid magenta line in the upper panel is the model linear intensity used in fitting. In the bottom panel, blue error bars are polarization position angles used in the fit and yellow error bars are polarization position angles excluded by error bar cuts. The model polarization comes from a fit with (unreduced) $\chi^2 = 773$ and parameters $\alpha = 2^\circ$ and $\zeta = 2^\circ$. The green solid line is the polarization for a model with $R_1 = 0.05R_{LC}$ (associated with intensity components C_1 and C_2), the black solid line is the polarization for a model with $R_2 = 0.40R_{LC}$ (associated with intensity components C_3, C_4 , and C_5), and the cyan solid line is the polarization for a model with $R_2 = 0.55R_{LC}$ (associated with intensity components C_6, C_7 , and C_8). We assumed that the polarization associated with components C_1, C_2 , and C_6 are orthogonal to the polarization associated with components C_3, C_4, C_5, C_7 , and C_8 . The red solid line is the model polarization of the three altitudes weighted by the model intensity. There are clearly features in the data that are not captured by the model but the overall structure of the polarization is captured. A phase of zero is the point of closest encounter to the magnetic axis in the model.

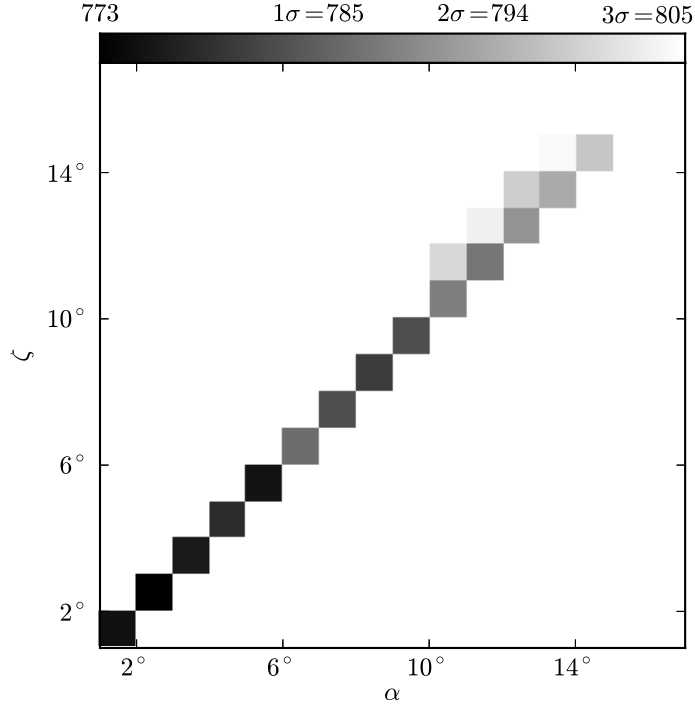


Figure 6.16: Map of (unreduced) χ^2 for PSR J2124–3358 in the α – ζ plane. All of the fitted models within 3σ from χ^2_{\min} have a phase of emission that is within the phase of emission predicted by the models and thus $\rho_{\text{ypt}} = 1R_{\text{LC}}$ is acceptable.

associated with components C_3 , C_4 , C_5 , C_7 , and C_8 as labeled in Figure 6.15. With these orthogonal mode jumps, the polarization forms a close-to-continuous sweep and the RVM can be reasonably fit to the data. Table 6.7 reports the best fit values and (unreduced) χ^2_{\min} for this fit.

With the assumption of multiple altitudes and mode jumps, the polarization was also fit. More than three altitudes did not significantly improve the fit. Also plotted in Figure 6.15 (top panel) is the best fit polarization model with multiple altitudes. The polarization associated with components C_1 and C_2 is assigned one altitude (R_1); the polarization associated with components C_3 , C_4 , and C_5 is assigned the second altitude (R_2); and the polarization associated with components C_6 , C_7 , and C_8 is assigned the third altitude (R_3). The fit is far from perfect and does not capture the many bumps and wiggles in the polarization data. The model does capture the overall

curvature of the polarization and significantly decreases the χ^2 (Table 6.7) although the α and ζ values do not change drastically between the two fits. For the RVM (unreduced) $\chi^2_{\min} = 2331$ and for the three-altitude model (unreduced) $\chi^2_{\min} = 773$. The F -test between RVM and the two-altitude model gives $F = 355.4$, $\text{DOF}_1 = 3$, and $\text{DOF}_2 = 529$. The probability of exceeding this F is $\text{Prob} \sim 0$, indicating the addition of altitude to the model is highly statistically significant.

The curvature direction of the bridging polarization sweep between orthogonal mode jumps is important here similar to the polarization of PSR J0023+0923 in Section 6.5.1. As discussed in Section 6.3.3, for a single-altitude polarization sweep with an orthogonal mode jump, the bridging section of polarization between the two modes will have the opposite curvature of that of the original sweep due to forward scattering. In PSR J2124–3358 between the polarization components associated with the intensity components C_5 and C_6 , the bridging sweep direction has a negative curvature and the original sweep direction is also negative. This indicates that the polarization of these two components are not exactly 90° , which is consistent with a multi-altitude model that has non- 90° orthogonal jumps between altitudes.

The values for R_1 , R_2 , and R_3 are quite restrictive and the statistical error bars on these values are quite small. These values are small because very few altitude combinations capture the subtle difference between polarization associated with the various components; for instance, note the rather large offset between the black and cyan solid lines in Figure 6.15 which represent model polarization from R_1 and R_2 . Only very particular sets of altitude will result in polarization with this amount of vertical shift. Also, $\rho_{\text{ypt}} = 1R_{\text{LC}}$ for all fits within the 3σ bound of χ^2_{\min} due to the small geometrical angles (α and ζ , see Figure 6.16).

6.6 Conclusion

In this paper, we attempted to push the limit of what we can learn from geometrical-based models applied to radio polarization. We have shown that this model can explain polarization for which the RVM fails (partially or fully) and can significantly alter fit parameters (α and ζ) obtained from the RVM. We have shown that a handful

of physical effects can alter our understanding of the geometry of millisecond and young pulsar radio emission. Additionally, we provided statistical comparisons to simpler models to quantify the significance of adding these physical phenomena to the model.

Both PSR J0023+0923 and PSR J1024–0719 clearly illustrate how multi-altitudes can capture the non-90° jumps seen in the position angle sweeps of the millisecond pulsar population. PSR J1057–5226 and PSR J1744–1134 illustrate the need for finite altitude and $\rho_{\text{ypt}} < R_{\text{LC}}$ to fully explain the large phase range of the emission seen in the data. PSR J1420–6048 illustrates how scattering affects can rectify discrepancies seen between multi-wavelength data. Finally, PSR J2124–3358 is a typical worst-case radio polarization from a millisecond pulsar. Despite its clear non-RVM characteristics, we were able to capture the overall structure of the polarization position angles sweep with finite and multiple altitudes and orthogonal mode jumps.

The RVM is not accurate for the radio polarization sweeps of these energetic pulsars. First, this emission originated from a significant fraction of the light cylinder which necessitates numerical calculation of this radio polarization. Additionally, non-90° jumps cannot be explained by simple orthogonal mode jumps and some polarization is scattered by the interstellar medium. Polarization of millisecond pulsars is notoriously hard to model and very few studies have attempted to tackle these objects. That we can explain some of the polarization of these pulsars is a significant step in the correct direction. This is a methods paper; with various example polarization data from a number of pulsars, we have shown that this method of using physically motivated, geometrically based phenomena can explain the inconsistencies of simpler models.

We greatly thank R. N. Manchester for supplying radio data for PSR J1024–0719, PSR J1744–1134, and PSR J2124–3358 which is published in Yan et al. (2011). We also owe many thanks to S. Johnston (2012, private correspondence) for supplying radio data for PSR J1057–5226 and PSR J1420–6048 and to J. W. T. Hessels for supplying radio data for PSR J0023+0923 (J. W. T. Hessels et al. in preparation). Roger W. Romani prepared figures and wrote the section on X-ray analysis of PSR

J1420–6048. Support for this project was provided in part by grants GO1-12073X and G03-14057A from the Smithsonian Astrophysical Observatory. This work was also supported in part by NASA grants NNX10AP65G and NAS5-00147. This work has been supproted by the Stanford Office of the Vice Provost of Graduate Education DARE Doctoral Fellowship Program to H.A.C.

Chapter 7

Characterization of Pulsars and Sub-Luminous Populations

This chapter focuses on work done in collaborations with others. Main contributions are in modeling polarization position angle data using the rotating vector model (RVM) and the numerical model. Example work will include use of the models for general characterization of pulsars and for a population study of γ -ray sub-luminous pulsars. Because of the collaborative nature of the work, this chapter will also focus on the broader use of polarization data in conjunction with other types of data. For the most part, γ -ray modeling was performed by Roger W. Romani.

First, We will discuss the paper “PSRs J0248 + 6021 and J2240 + 5832: Young Pulsars in the Northern Galactic Plane. Discovery, Timing, and Gamma-ray observations” (Theureau et al., 2011) in which two pulsars are reported as detected in the γ -ray by the *Fermi* Large Area Telescope. Many properties of the pulsars are characterized using γ -ray and radio data.

PSR J1119-6127 is likewise characterized in “Observations of Energetic High Magnetic Field Pulsars with the *Fermi* Large Area Telescope” (Parent et al., 2011). A number of high magnetic field pulsars are discussed in the paper and PSR J1119-6127 is analyzed with a single-altitude polarization model.

In “Broad-Band KeV to MeV Characteristics Of Soft Gamma-Ray Pulsar PSR J1513–5908” (Den Hartog et al., in prep.), the pulsar PSR J1513–5908 (B1509–58)

is analyzed in a number of wavelengths using revisited and updated data. We analyze the radio polarization using a single-altitude model.

The pulsar PSR J0737–3039A is analyzed using a two-altitude polarization model in “*Fermi* LAT Pulsed Detection of PSR J0737–3039A in the Double Pulsar System”. We also include scattering effects in this model although it is difficult to reproduce the scattering effects seen in the data. This pulsar has complex polarization, which we selectively cut. This pulsar is particularly interesting because few mildly spun-up pulsars have been detected in the γ -rays.

Finally, We will discuss the paper “Sub-luminous γ -Ray Pulsars” (Romani et al., 2011). The paper examines a number of young radio pulsars that are weak in the γ -rays. We try to determine whether this sub-luminosity is due to aligned geometry using geometric constraints (including six pulsars for which we perform analysis using radio polarization).

7.1 PSR J0248+6021 and PSR J2240+5832: Characterizing Young Pulsars with RVM

This section is based on work done for “PSRs J0248+6021 and J2240+5832: Young Pulsars in the Northern Galactic Plane. Discovery, Timing, and γ -Ray Observations” (Theureau et al., 2011).

PSR J0248+6021 ($P = 217$ ms) and PSR J2240+5832 ($P = 140$ ms) are young pulsars first discovered in the radio (Foster et al., 1997; Ray et al., 1999). The polarization sweep for both pulsars is relatively smooth such that likely only a single-altitude component contributes to the emission.

For these two pulsars, we applied both the RVM and γ -ray light curve models to the available data. Figure 7.1 shows the light curves at various wavelengths as well as the polarization data. Modeling results indicate that the γ -ray emission from PSR J0248+6021 is from a merged double γ -ray peak while the emission from PSR J2240+5832 is from a narrow caustic. The paper discusses various measurements

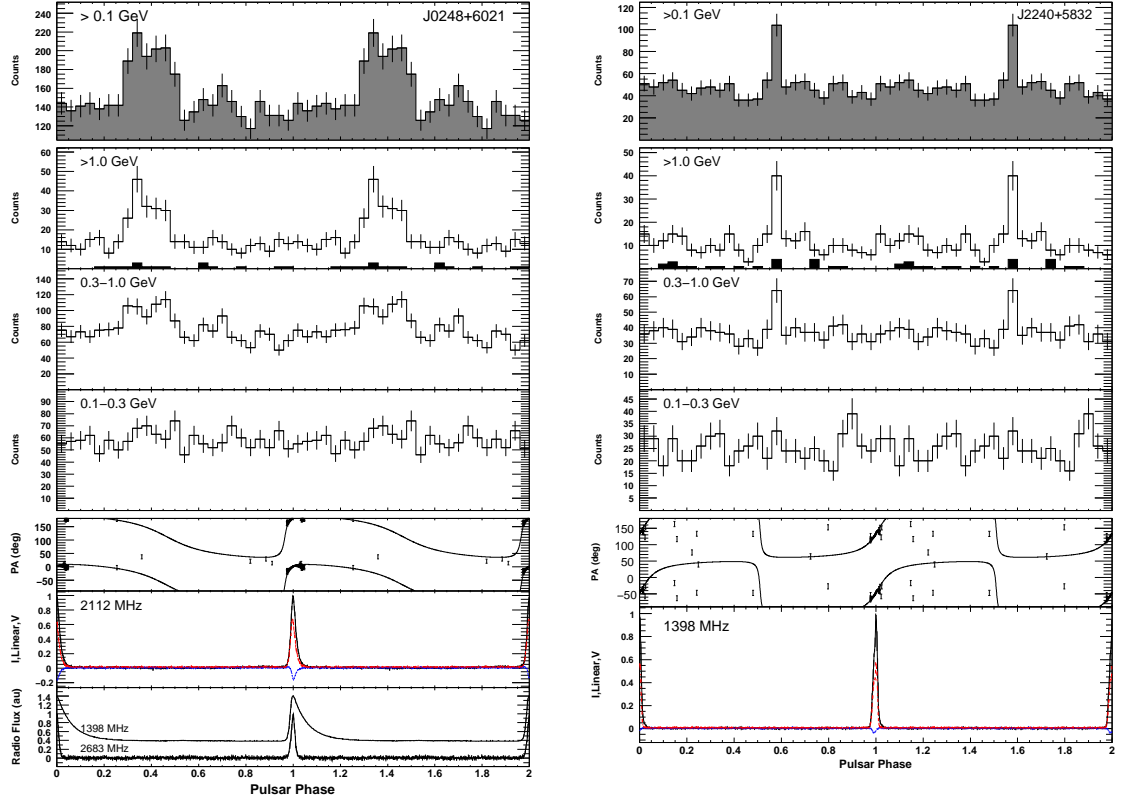


Figure 7.1: Figure taken from Theureau et al. (2011). Phase-aligned γ -ray and radio light curves for PSR J0248+6021 and PSR J2240+5832 obtained with the *Fermi* Large Area Telescope and the Nançay Radio Telescope. The bottom panel for PSR J0248+6021 show the radio profiles at three frequencies. The second panel from the bottom for PSR J0248+6021 and the bottom panel for PSR J2240+5832 show the degree of linear (red dashed) and circular polarizations (blue dotted), as well as the linear polarization position angle and a RVM fit. The other panels show the γ -ray light curve data in different energy bands. Two rotations are shown for clarity.

of the pulsars PSR J0248+6021 and PSR J2240+5832 such as flux density, proper motion, dispersion measure, kick velocity, and rotation measure.

We applied the RVM to the polarization data of PSR J0248+6021 (2.1 GHz) and PSR J2240+5832 (1.4 GHz). We cut on polarization with error bars greater than $\pm 2^\circ$. The polarization position angle sweeps are flattened due to scattering. Data at 1.4 GHz was available for PSR J0248+6021 but appeared distorted by scatter so only the 2.1 GHz data was used. Red error bars on Figure 7.2 show points used in

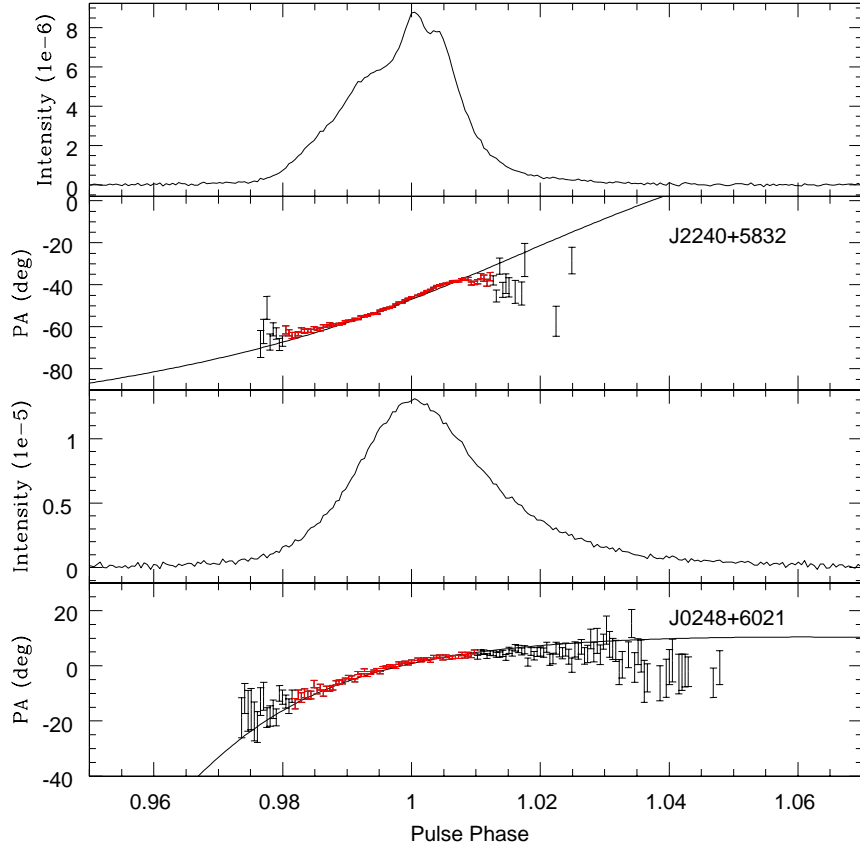


Figure 7.2: Figure taken from Theureau et al. (2011). Expanded view of the radio polarization position angle sweep near the peak in radio intensity. The red points show the data used in the RVM fit. The black points failed the selection cuts described in the text. Top two frames are data for PSR J2240+5832 at 1.4 GHz. The RVM curve shown corresponds to $\alpha = 108^\circ$ and $\zeta = 123^\circ$. Bottom two frames are data for PSR J0248+6021 at 2.1 GHz. The RVM curve shown corresponds to $\alpha = 46^\circ$ and $\zeta = 52^\circ$.

the fitting procedure.

For PSR J0248+6021, the best fits give geometric angles $\beta \sim 5^\circ$ (where $\beta = \zeta - \alpha$) and α between 25° and 110° . The best χ^2 is 86.6 with reduced $\chi^2_{\text{min}} = 1.6$. For PSR J2240+5832, the best fits give geometric angles $\beta \sim 16^\circ$ and α between 75° and 130° although plausible solutions extended to α between 10° and 150° . The best χ^2 is 86.6

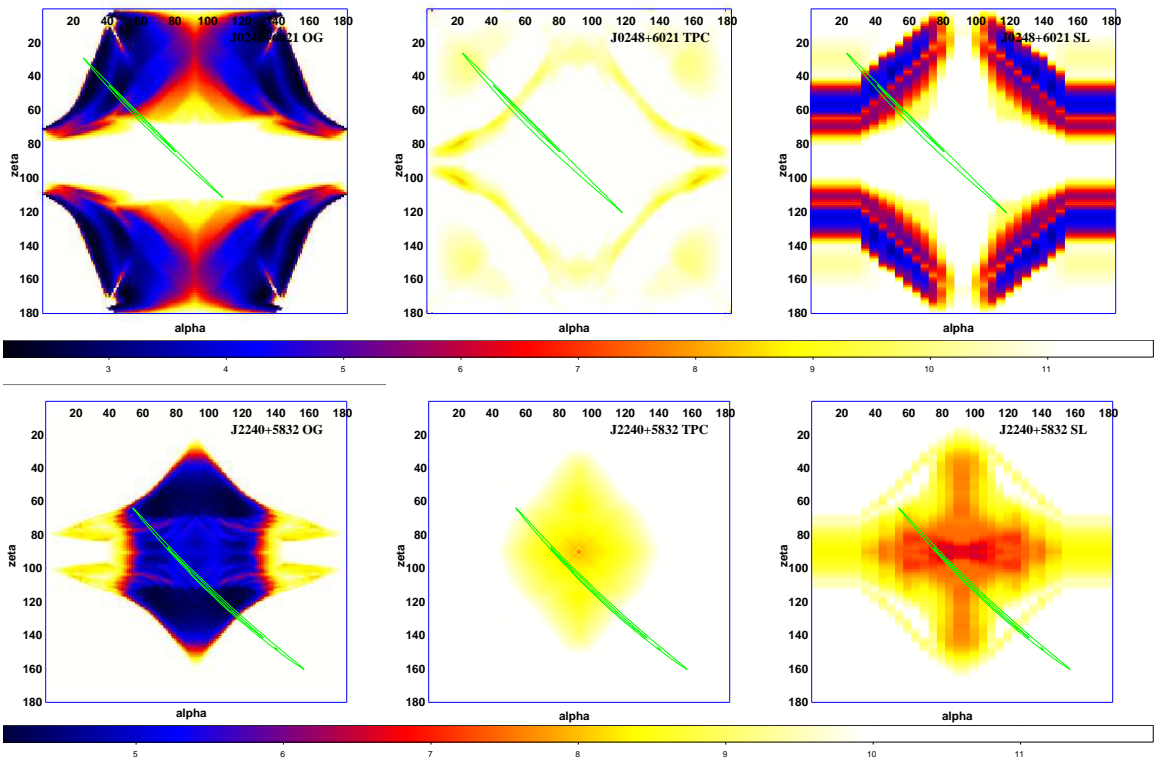


Figure 7.3: Figure taken from Theureau et al. (2011). Pulsar geometry and emission modeling fit map for PSR J0248+6021 and PSR J2240+5832 in the α - ζ plane. Green contours show the RVM fit to the radio polarization data. Contours are at $\delta(\chi^2/\text{Degree of Freedom}) = 0.25$ and 0.5 above the minimum $\chi^2/\text{Degree of Freedom}$ of 1.6 for PSR J0248+6021 and $\delta(\chi^2/\text{Degree of Freedom}) = 0.4$ and 0.8 above the minimum $\chi^2/\text{Degree of Freedom}$ of 5.1 for PSR J2240+5832. The color backgrounds are χ_3 maps of the fit to the observed > 100 MeV pulse profile for the outer gap model (left), the two-pole caustic model (middle), and the separatrix layer model (right), at different values of the magnetic inclination, α , and the minimum angle to the line-of-sight, ζ (Romani & Watters, 2010). Each panel has the same color scale, where dark colors represent better fits. The preferred models lie along the green RVM-selected band.

with reduced $\chi^2_{\min} = 1.6$. Figure 7.2 additionally shows reasonable model polarization sweeps overlaid on data points.

On Figure 7.3, green contours trace the best fit RVM in the α - ζ plane. The colored maps show best fit outer gap model, two-pole caustic model, and separatrix layer model (Bai & Spitkovsky, 2010) to the γ -ray data. The weighting used is the

χ_3 of Romani & Watters (2010). For PSR J0248+6021, the best fit overlap between outer gap and RVM model is $\alpha = 46^\circ$ and $\zeta = 52^\circ$. For PSR J2240+5832, the best fit overlap between outer gap and RVM models is $\alpha = 101^\circ$ and $\zeta = 117^\circ$. Overall, the outer gap model seemed to be more consistent with the polarization model results than the other γ -ray models.

7.2 PSR J1119–6127: Characterization a High Magnetic Field Pulsar with Single-Altitude Model

This section is based on work done for “Observations of Energetic High Magnetic Field Pulsars with the Fermi Large Area Telescope” (Parent et al., 2011).

In the paper Parent et al. (2011), detection with the *Fermi* Large Area Telescope of PSR J1119-6127 (Period = 0.408s) and upper limits of pulsars PSR J1718-3718, PSR J1734-3333 and PSR J1846-0258 are reported and criteria for non-detection are discussed. These pulsars have high magnetic fields. In the paper, the spectrum of PSR J1119-6127 is concluded to be more similar to a young pulsar rather than a magnetar as might be expected from such a high magnetic field.

Data used to analyze the radio polarization was taken during a glitch recovery in PSR J1119-6127 wherein more data per phase was available. Because of the larger number of available data points, modeling the polarization position angles was more constraining. Data analysis details are given in Weltevrede et al. (2010b) and Hobbs et al. (2004).

In the γ -ray modeling, both two-pole caustic and outer gap models were tested with $w = 0.02$. Results of these fittings are seen in Figure 7.4. The figure of merit here is the χ_3 weighting defined in Romani & Watters (2010). Additionally, on the plot are the RVM fit contour results in green as well as a numerical single-altitude model fit contour in magenta. Two-pole caustic fitting results and the polarization fitting results have poor overlap compared to the outer gap model. The best models are at $\alpha = 125^\circ$ to 130° and $\zeta = 140^\circ$ to 150° for the outer gap model and at $\alpha = 125^\circ$

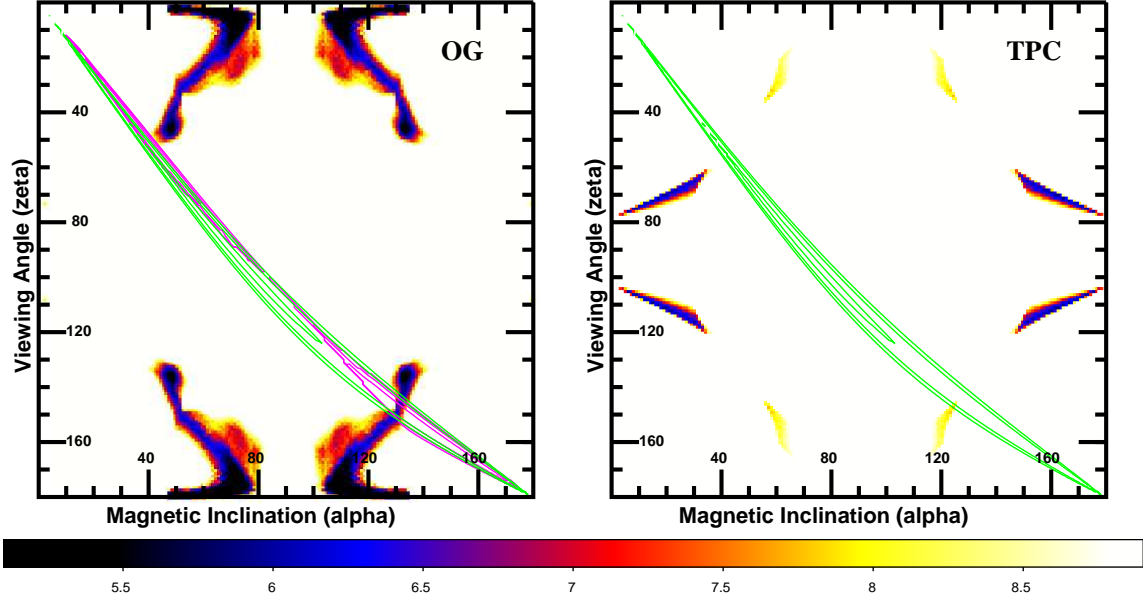


Figure 7.4: Figure taken from Parent et al. (2011). Pulsar geometry and emission modeling fit map for PSR J1119–6127 with the outer gap (left panel) and the two-pole caustic (right panel) models in the α – ζ plane. Green contours show the RVM fit to the Weltevrede et al. (2011) radio polarization data. For the left panel we also show the polarization fit for finite-altitude, open zone radio emission ($R = 0.09 R_{LC}$, magenta contours). Contours are at 1.5, 2.5, and 3.5 times the minimum value of the reduced $\chi^2 = 0.85$. The background color scale gives the χ_3 statistic fit to the observed > 500 MeV γ -ray pulse profile. The color scales in the panels are the same, with dark colors representing better fits. Preferred models lie along the diagonal polarization fit band.

and $\zeta = 145^\circ$ for the two-pole caustic model. The two models give similar geometry angles but the outer gap model is a better fit over a larger parameter space as can be seen in Figure 7.5

The best fit parameters for polarization modeling yield reduced χ^2 of 1.1. The altitude of emission derived from polarization fitting is $0.1R_{LC}$. It is interesting to note that using the BCW model yields lower altitudes (Weltevrede et al., 2011) and requires smaller α for emission originating in the open zone.

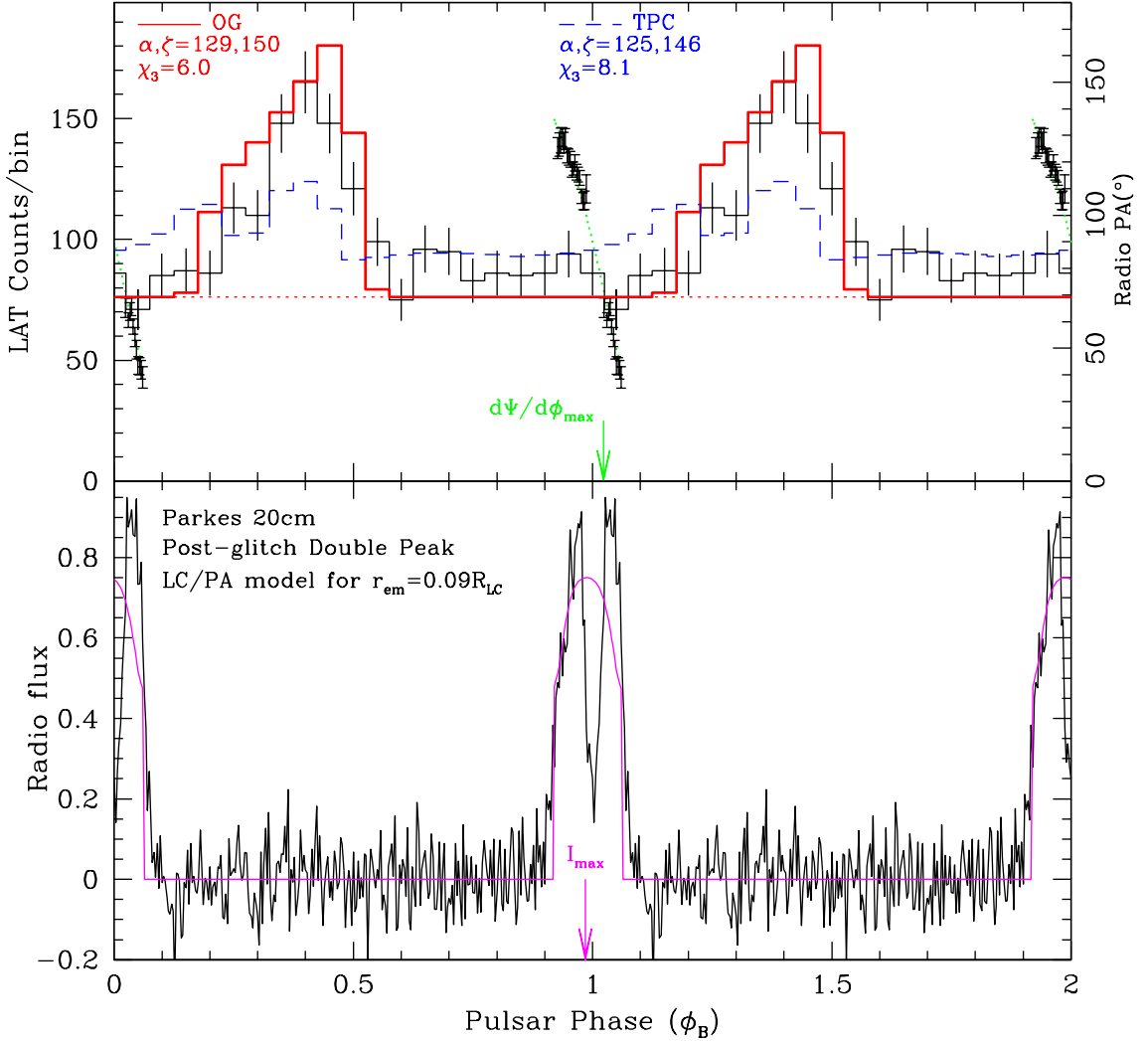


Figure 7.5: Figure taken from Parent et al. (2011). Light curves and polarization of PSR J1119–6127 overlaid with models. The bottom panel shows the Parkes radio light curve in the two peaked (post-glitch) mode, which provides the best model constraints. The corresponding radio polarization position angle data are shown (right scale) in the upper panel. The model pulsar phase (ϕ_B , bottom axis) is referenced to the closest approach of the magnetic axis to the Earth line-of-sight, as fit from the polarization sweep. The sweep rate maximum (green arrow) and pulse profile offsets (magenta arrow) are shown, with good matches to the observed radio data for an altitude of $R = 0.09 R_{\text{LC}}$. The upper panel shows the *Fermi* pulse profile (left scale) and model outer gap (solid line) and two-pole caustic (dashed line) profiles. These are best-fit profiles (geometric angles in the legend) and the phase is referenced to the radio-determined phase of the magnetic axis. The γ -ray background, shown by the dotted line, was estimated using an annular ring centered on the radio position with inner and outer radii of 0.5° and 1.5° respectively, during the off-pulse region.

7.3 PSR J1513–5908: Characterizing a Soft γ -ray Pulsar with Single-Altitude Model

This section is based on work done for “Broad-Band KeV to MeV Characteristics of Soft γ -Ray Pulsar PSR J1513–5908” (Den Hartog et al., in prep.).

The paper “Broad-Band KeV to MeV Characteristics of Soft γ -Ray Pulsar PSR J1513–5908” (Den Hartog et al., in prep.) aims to do a spectral study covering 2 KeV to 1 GeV including updated *Fermi* data and revisited archival RXTE-PCA and HEXTE data along with historic CGRO-COMPTEL data of the pulsar PSR J1513–5908 (PSR B1509–58). The pulsar was also analyzed using radio polarization data.

The polarization data analyzed is 1.4 GHz data. The pulsar PSR J1513–5908 has a period of 151 ms. Also noted in the paper is an extra component in the radio intensity of PSR J1513–5908 before the peak of the main pulse. We had hoped to model this component using polarization but the scatter of the data was too large to derive useful fit results.

The typical retarded dipole with photons projected tangent to the magnetic field lines is used to calculate the position angles of the polarization. Further, models used here extrapolate from the classical RVM allowing emission from finite radial altitudes above the surface of the neutron star with relativistic and sweep-back effects. Allowed altitudes ranged between $.002R_{LC}$ (the radius of the neutron star assuming $R_{NS} \sim 15$ km) to $.9R_{LC}$.

Figure 7.6 shows the polarization position angle sweep and intensity profile for 20 cm data. The sweep is relatively simple and shows no signs of orthogonal mode jumps or multiple altitude. RVM fits relatively well to the polarization with $\chi^2_{\min} = 44$ for Degree of Freedom=DOF= 55 – 4. The four fit parameters are α , the angle between the magnetic axis and rotation axis, ζ , the viewing angle as measured from the rotation axis and the horizontal and the vertical offsets in the polarization angles. The best fit model with finite altitude has $\chi^2_{\min} = 39$ for DOF= 55 – 5 although the

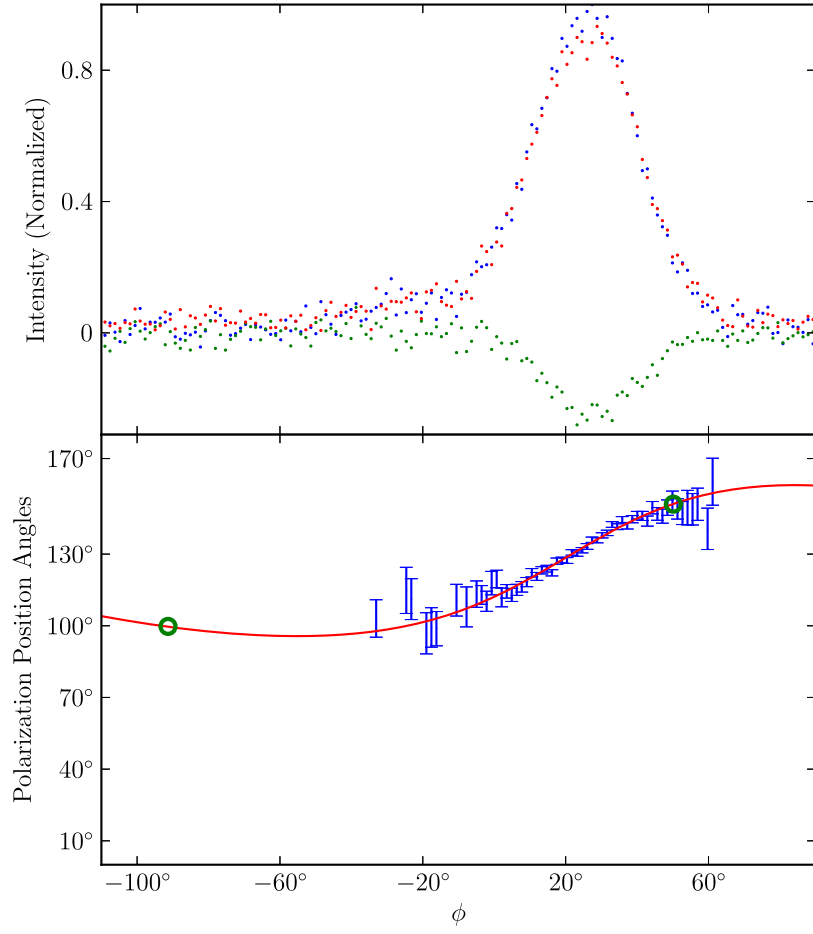


Figure 7.6: Figure taken from Den Hartog et al. (in prep.). Intensity and polarization data for PSR J1513–5908 overlaid with model. In the upper panel, blue points are total intensity data, red points are linear polarization intensity data, and green points are circular polarization intensity data for PSR J1513–5908 at 20 cm. In the bottom panel, blue error bars are polarization position angles used in the fit. The red solid line is the fit model polarization with $R = 0.24R_{LC}$, $\alpha = 153^\circ$, and $\zeta = 133^\circ$. Empty circles mark phase of emission from open field lines.

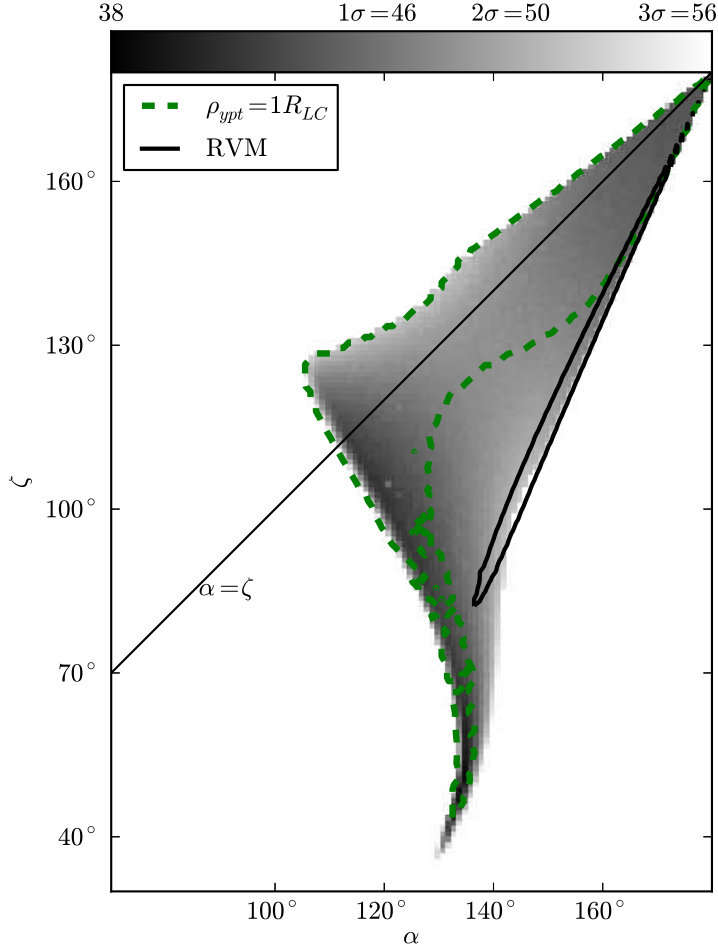


Figure 7.7: Figure taken from Den Hartog et al. (in prep.). Map of χ^2 for PSR J1513-5908 fit to radio polarization in the α - ζ plane. Overlaid are 3σ above χ^2_{\min} contour for zero altitude RVM fit (black) and 3σ above χ^2_{\min} contour for the assumption that emission must come from the formal open zone.

best fit model might not be the most physically viable model as will be discussed later. The solid red line in Figure 7.6 is a finite-altitude model at $\alpha = 153^\circ$, $\zeta = 133^\circ$, and $R = 0.24R_{LC}$ with $\chi^2 = 48$. Green circles on the solid red line mark the expected end of emission based on a formal open zone assumption.

Figure 7.7 shows the best fit χ^2 surface map projection in the α - ζ plane for the single-altitude model. The 3σ contours for the RVM fit are overlaid on the color

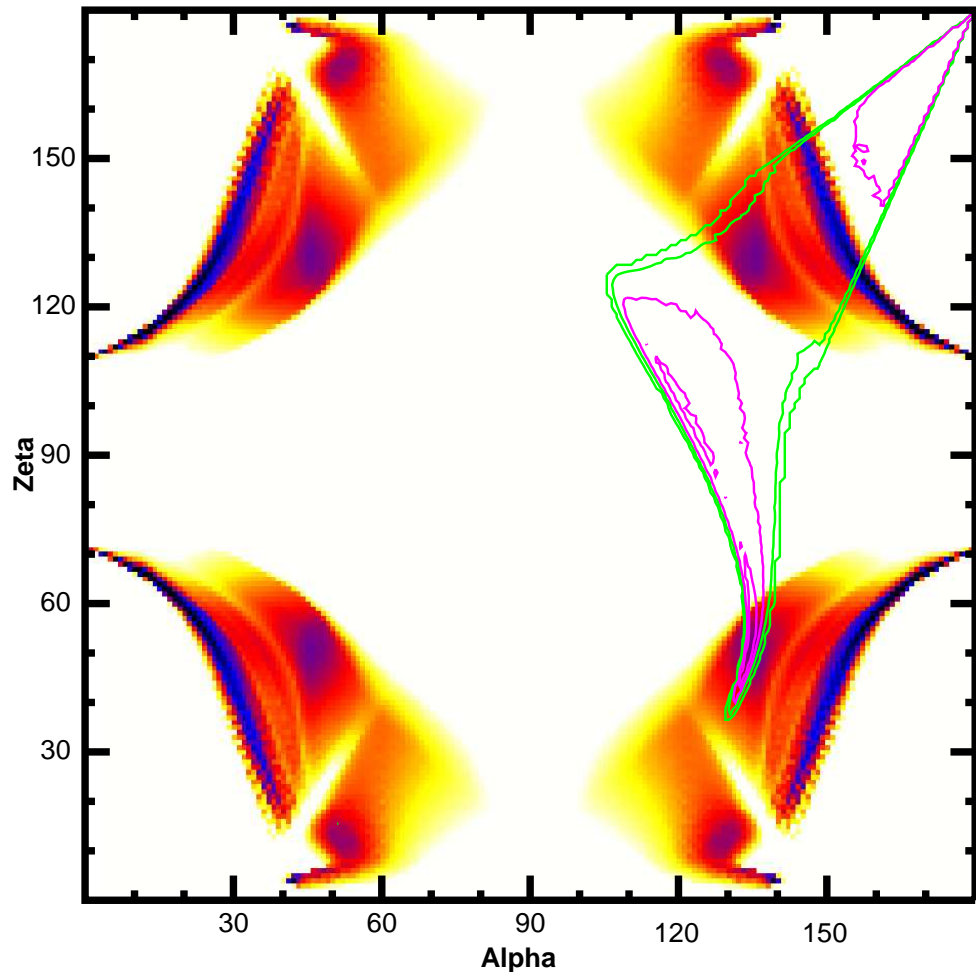


Figure 7.8: Figure taken from Den Hartog et al. (in prep.). Pulsar geometry and emission modeling fit map of an outer gap model and radio polarization model for PSR J1513–5908 in the α – ζ plane. Contours show the polarization fit of the 0.5σ and 1.0σ regions in magenta; and the 2.0σ and 3.0σ regions in green. A wide range of geometries is allowed by these polarization data, including the best γ -ray fits. Good fits must also match the phase of the magnetic dipole axis (see text).

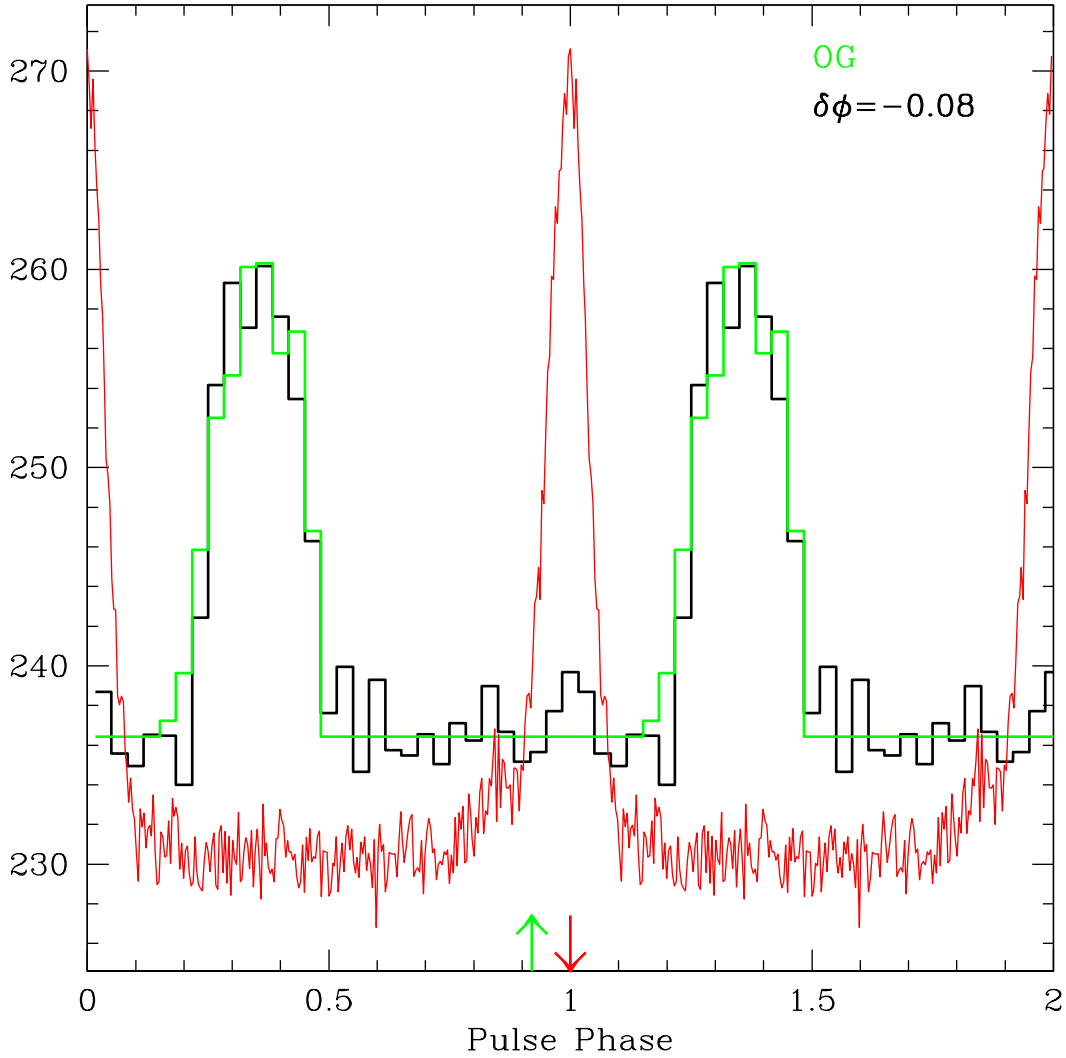


Figure 7.9: Figure taken from Den Hartog et al. (in prep.). Radio and γ -ray light curves of PSR J1513–5908 with model light curve for $\alpha = 153^\circ$, $\zeta = 133^\circ$. A single peak dominates since the line of sight skims the γ -ray caustic. The radio emission altitude is $0.24R_{LC}$ and polarization and γ -ray fits both indicate that the magnetic axis (green upwards arrow) leads the radio peak by $\phi = 0.08$.

map in black. Additionally, on this panel is a green contour that encloses the model parameters for which model emission phase is equal to or greater than the emission phase seen in the data. The model emission phase is defined by the emission from the classic open field lines. Overlap between these contours is minimal. This indicates a physical need to increase emission phase from RVM either by increasing the altitude of emission or widen the open zone cap.

Following Romani & Watters (2010) we fit the γ -ray light curve using the χ_3 statistic. While PSR J1513–5958 is very energetic, implying a small gap and emission close to the last closed field lines, we find appreciably better light curves for a modest gap width, $w = 0.05 - 0.1$. In Figure 7.8, the background color scale shows the goodness of fit for an outer gap model with $w = 0.1$. Overlaid are contours from the radio fitting. To be a viable model, the γ -ray fit must lie inside the radio contours. Since the polarization presents a simple sweep, this is not very constraining, with a wide range of geometries compatible at the 3σ level. However, the polarization fit also tightly constrains the phase of the magnetic axis relative to the radio intensity peak. For a viable model, this should match as well.

The strip of best γ -ray fits crosses the radio-allowed region along $\alpha = 153^\circ$ and $\zeta = 145^\circ$ to $\alpha = 156^\circ$ and $\zeta = 128^\circ$ with $\chi_3 < 4.5$. In this region the phase of the magnetic axis ranges from -0.06 to -0.08 (in fractions of a period) and the radio emission altitude varies from 0.1 to $0.3R_{LC}$. In Figure 7.9, we show the fit γ -ray light curve for $\alpha = 153^\circ$ and $\zeta = 133^\circ$. The radio fit altitude is $0.24R_{LC}$ and the polarization fit is 1.2σ from its minimum. In this region *both* the γ -ray and polarization fits place the magnetic dipole axis 0.08 before the radio peak. A second region of plausible γ -ray fits (with $\chi_3 \approx 5.4$) lies close to the polarization fit minimum. In this region, $\alpha = 135^\circ$ and $\zeta = 51^\circ$ and the γ -ray light curve, while dominated by a single peak, has a tail to phase 0.5. However the fit magnetic axis phases do not agree (-0.03 for γ -ray, 0 for radio) and the radio altitude is quite high, 0.75 to $0.85R_{LC}$. At this altitude the details of the magnetic structure are less reliable; so we prefer the lower altitude solution with the correct phase match. At this lower altitude, there is also room for the field lines to open within the light cylinder, giving a y-point radius < 1 and a larger effective w .

Table 7.1: Polarization Fit Parameters for PSR J0737 – 3039A

α (°)	ζ (°)	R_1/R_{LC}	R_2/R_{LC}	χ^2	DOF
$98.8^{+8}_{-1.5}$	$95.8^{+13.2}_{-4.3}$	$0.01^{+0.22}_{-0.01}$	$0.11^{+0.49}_{-0.05}$	48	35

Note. — Errors are the extrema of the 1σ contours in the full multidimensional parameter space. R_1 is the emission altitude of the central component of P1 and R_2 is the altitude of the central component of P2.

7.4 PSR J0737–3039A: Characterizing a Double Pulsar System with Finite-Altitude Model

This section is based on work done for “Fermi LAT Pulsed Detection of PSR J0737–3039A in the Double Pulsar System” (Guillemot et al., 2013).

The paper (Guillemot et al., 2013) reports the detection of PSR J0737–3039A, the first detection of a mildly recycled pulsar by the *Fermi* Large Area Telescope. Such a pulsar is only mildly spun up by its companion. The pulsar PSR J0737–3039A is in a 2.4 hour orbit with another pulsar (Burgay et al., 2003; Lyne et al., 2004). Such a detection is exciting because it fills in an underpopulated region of the P - \dot{P} picture (Abdo et al., 2010a).

Further, understanding the pulsars formation has been of interest. The viewing angle is a measure of the misalignment between the spin axis and orbital angular momentum since the inclination of the binary system is known. This measurement in turn is given as ζ near 90° (as discussed below) indicating that the misalignment angle is small. This has important implications on the formation theory of the system (Breton et al., 2008; Ferdman et al., 2013; Podsiadlowski et al., 2005).

The 1.4 GHz data from Parkes radio telescope was used in the analysis of PSR J0737–3039A. We used orthogonal mode jumps and interstellar scattering as well as multiple and finite altitude. We fit only the central components of the two peaks. We believed that the trailing edges of the emission was dominated by plasma effects and that the present model would not adequately capture the field line structure from

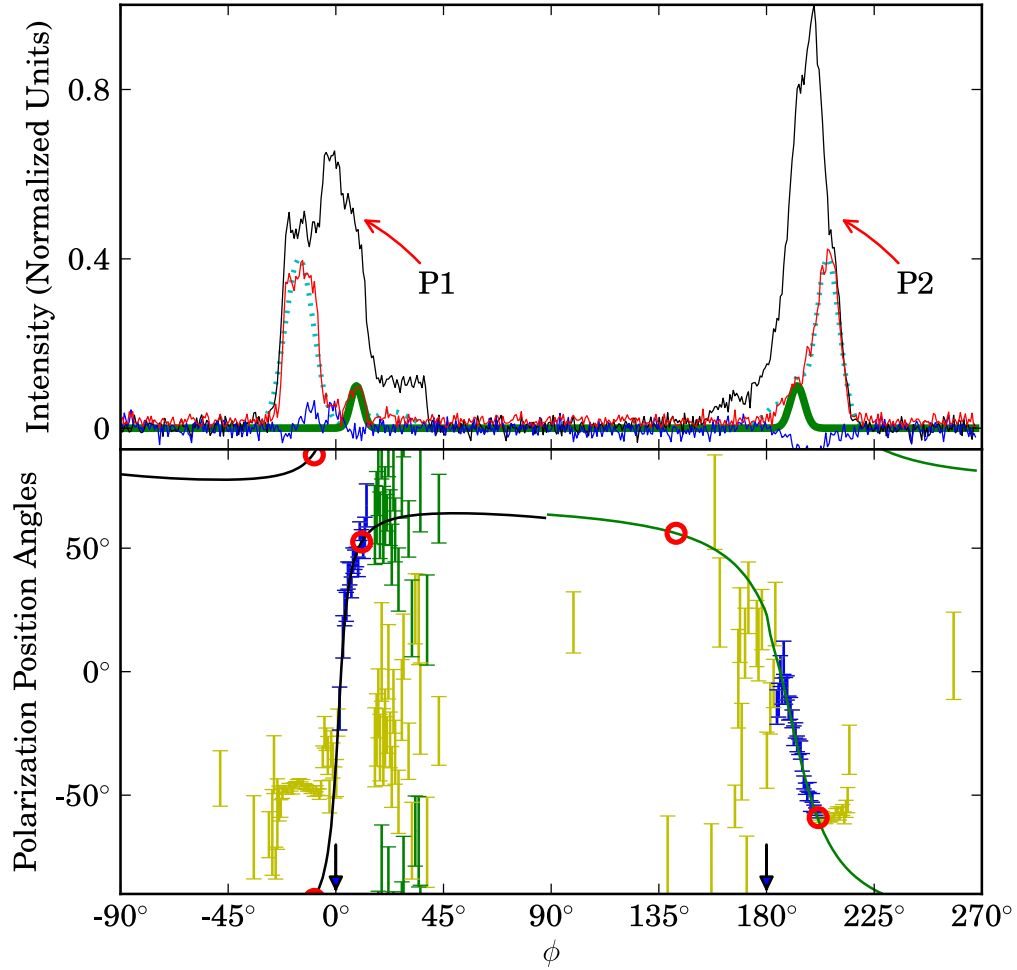


Figure 7.10: Figure taken from Guillemot et al. (2013). Polarimetric profile for PSR J0737–3039A as observed at 1.4 GHz with the Parkes radio telescope (R. N. Manchester, private communication). Top panel: Stokes parameter curves (black is total intensity, red is linear polarized intensity, and blue is circularly polarized intensity) and Gaussian decomposition of the linear intensity components (dotted curve is all linear and the thick green curve gives the rapid sweep central component fit here). Bottom: position angle data (blue: central components, yellow: other position angle values, green: P1 tail with an orthogonal mode jump). The smooth curves give the best fit model for the two poles while the red circles denote the boundaries of the open zone at the emission altitude. Arrows denote the phase of the closest approach of the magnetic axes to the Earth line-of-sight.

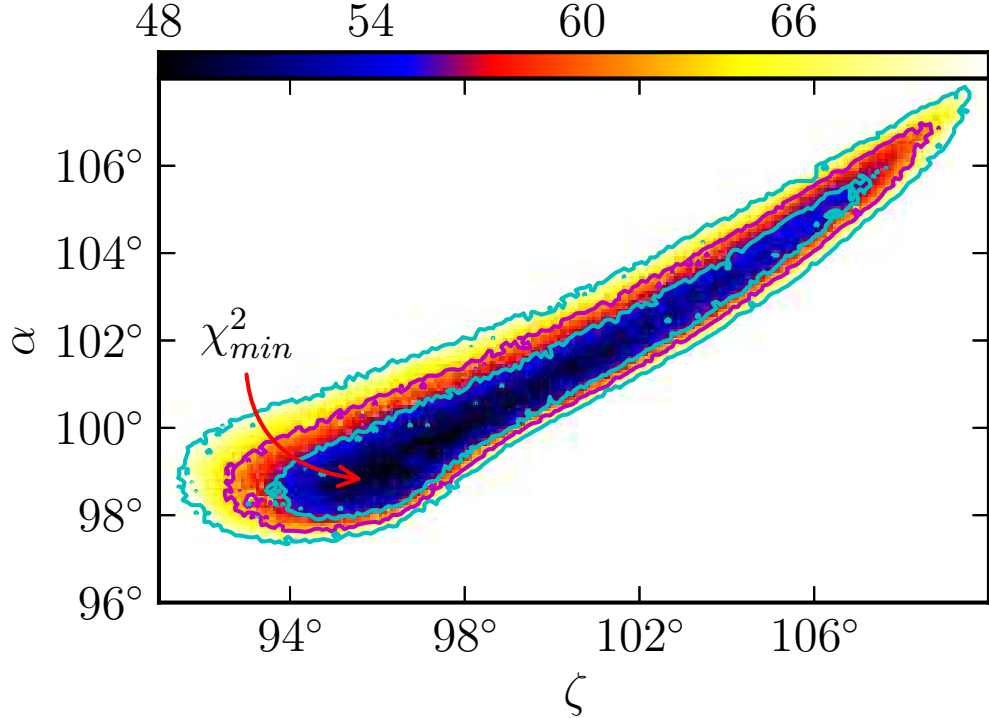


Figure 7.11: Figure taken from Guillemot et al. (2013). Map of χ^2 surface of the RVM fit to the radio polarization data (central components) for PSR J0737 – 3039A in the α – ζ plane. The best fit orientation angles (α , ζ) are indicated by an arrow, while the contours are shown at the 1σ , 2σ and 3σ levels above χ^2_{\min} .

this much higher emission. Thus we favored modeling only the central part of the polarization of the two radio peaks. In particular, the flattened components of the polarization can not be modeled using typical magnetic field lines and single altitudes.

Figure 7.10 labels the Gaussian components used for the intensity in the upper panel (green thick line) and the polarization in the lower panel (blue data points). The unmodeled data points are in yellow on the Figure 7.10. Trailing edges of $P1$ in linear intensity are separated from the central component by linear intensity of zero which suggests a orthogonal mode jump (for a more in depth discussion of this phenomena see Section 6.3.3). The green data points show the polarization offset by 90° .

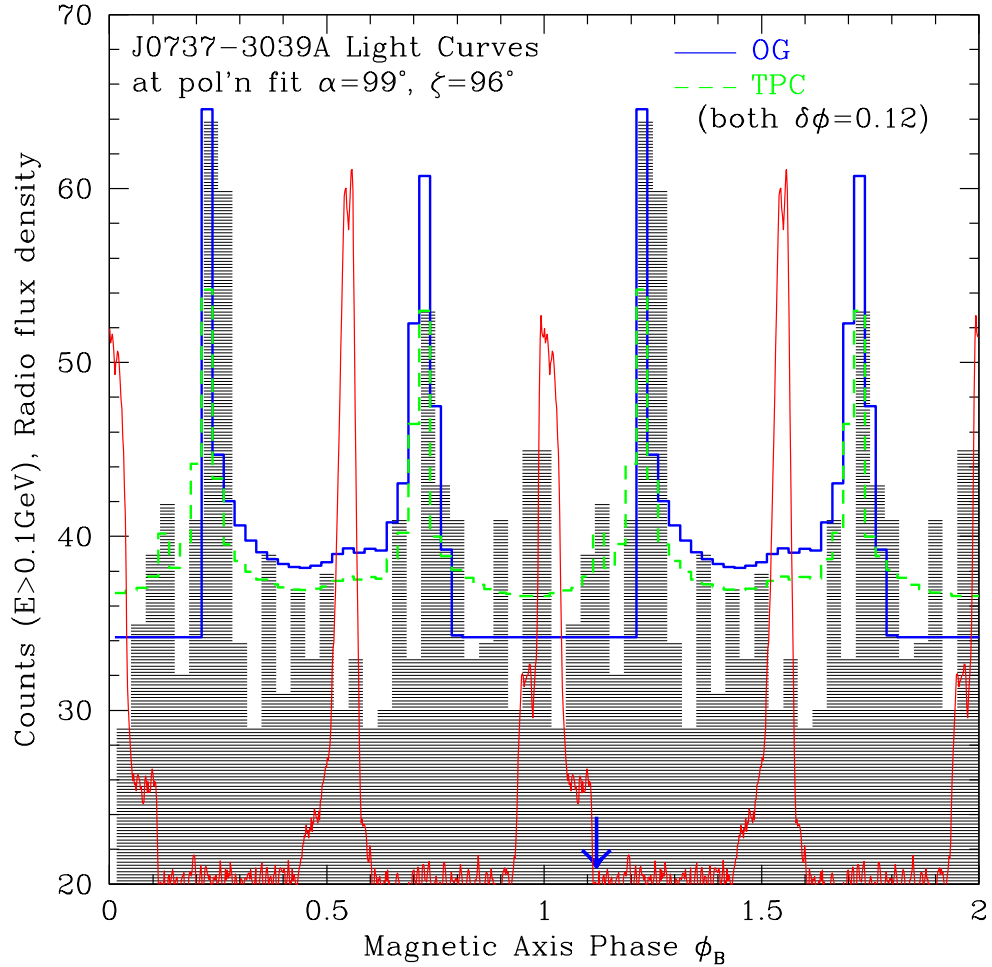


Figure 7.12: Figure taken from Guillemot et al. (2013). Light curves for PSR J0737–3039A at the α and ζ angles determined from the radio polarization study, and for the outer gap model (solid blue line) and the two-pole caustic model (dashed green line). The observed radio and γ -ray profiles are shown as a solid red line and as a shaded gray histogram, respectively. See Figure 7.10 for the definition of the magnetic axis phase ϕ_B . The blue arrow denotes the location of the magnetic axis under the outer gap and two-pole caustic geometries.

The black and green solid lines on the lower panel of Figure 7.10 are the best fit model to the blue polarization data points. The altitudes for the two components are different at $0.01R_{LC}$ for $P1$ and $0.11R_{LC}$ for $P2$. At these altitudes, The red circles indicate the open zone phase expected. Interestingly, the polarization not modeled falls outside of this phase, indicating that the polarization is from higher altitude emission or from emission within the formal closed zone and hinting at reasons for its unusual structure. Indeed, our model is then one where the central components are from the center of a hollow cone of emission where the altitude is relatively low and the wings are from the higher altitudes of the cone. Full fit parameters and errors are given in Table 7.1. The fit map of χ^2 is given in Figure 7.11.

The results of the polarization fitting were compared to γ -ray light curve modeling results. Namely, the polarization fitting produced a phase of closest approach for the surface dipole axis. Both outer gap and two-pole caustic models produced acceptable light curves in the region of best fit in the radio polarization as seen in Figure 7.12. But the model phase zero ($\phi = 0$) of the radio and γ -ray is offset by 0.1. One possible explanation is the lack of plasma effects in the modeling. For instance, Kalapotharakos et al. (2012a) found that including finite conductivity in magnetohydrodynamics simulations will cause such a lag compared to vacuum models.

In addition to polarization modeling, simultaneous fits in radio and γ -ray to the light curves was also performed resulting in similar geometric angle constrains.

7.5 Population Study: Characterizing Sub-luminous γ -Ray Pulsars Using Polarization

This section is based on work done for “Sub-luminous γ -Ray Pulsars” (Romani et al., 2011)

In the paper “Sub-luminous γ -Ray Pulsars” (Romani et al., 2011) we aimed to show that pulsars sub-luminous in the γ -rays is due to alignment using radio polarization modeling and data. The γ -ray luminosities scales with the spin-down energy as $L_\gamma \approx (\dot{E} \times 10^{33} \text{ erg/s})^{1/2}$. This is based on properties of the Goldreich-Julian

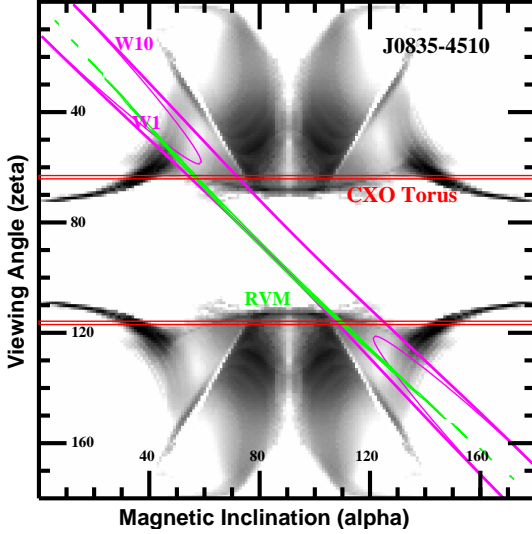


Figure 7.13: Figure taken from Romani et al. (2011). The γ -ray fit map for Vela in the α - ζ plane with radio polarization, X-ray torus, and pulse width constraints. The background gray scale shows the goodness of fit of the *Fermi* light curve to a basic outer gap model, with dark colors being better fits. Additionally, red lines mark constraints from an X-ray pulsar wind nebula torus fit, green contours mark constraints from RVM, and magenta contours mark constraints from opening angle arguments.

model ($L_\gamma \propto \dot{E}^{1/2}$, see, for example, Lyne (2006)) plus observation of pulsars (Abdo et al., 2010a). However, a number of pulsars have luminosity or limits that are more than an order of magnitude below this estimated luminosity, L_γ . The paper aims to test whether this weak luminosity is due to the pulsars beaming away from the Earth. Other explanations include the pulsars having physical properties that causes low luminosity or the estimated distance to the pulsars is drastically off and they are farther away than calculated.

Open zone arguments are utilized in this paper to constrain acceptable parameter space. The parameters W_1 and W_{10} represent the width of the radio pulse assuming that the pulse ends when the intensity falls below 1% or 10% respectively. If one definition is more appropriate for a given pulsar, it will be noted below. For more details on the relationship between the phase width and the size of the open zone,

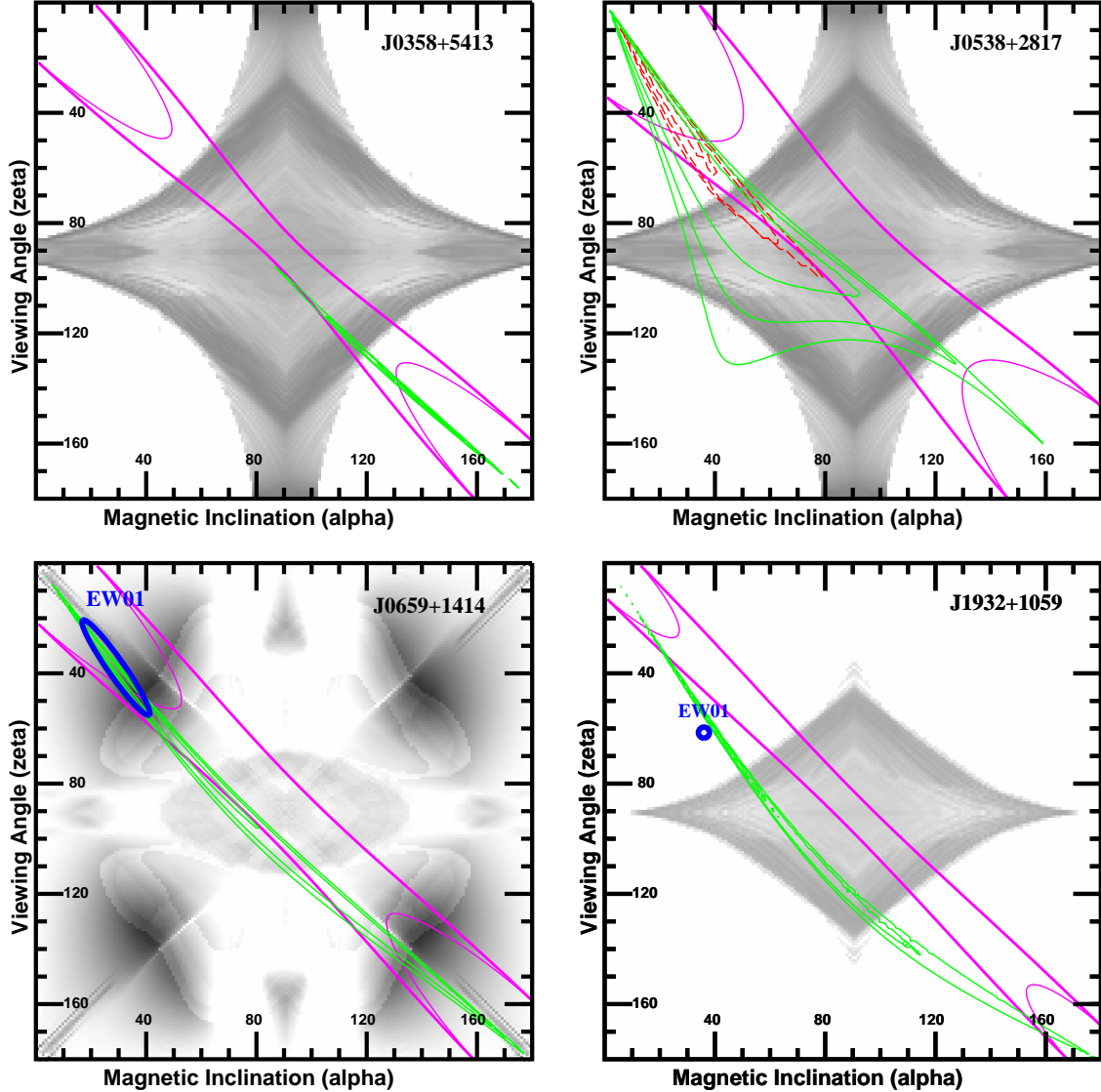


Figure 7.14: Figure taken from Romani et al. (2011). The γ -ray fit map for sub-luminous pulsars with parallax distances in the α - ζ plane with radio polarization and pulse width constraints. The backgrounds show the generic locations providing sharp outer gap pulses, except for PSR J0659+1414, where the background shows the allowed fits to the observed *Fermi* pulses, including lower altitude (two-pole caustic model) emission. “Good” fits here for the other pulsars are in white regions because of the sub-luminous nature of the pulsars. Three green contours show the loci of best RVM matches, while the bold and narrow magenta curves showed the regions allowed by emission from the static dipole open zone for our estimated emission altitude. For PSR J0659+1414 (PSR B0656+14) and PSR J1932+1059 (PSR B1929+10) the RVM fits of Everett & Weisberg (2001) are indicated. For PSR J0538+2817 the fits imply large emission altitudes, requiring a numerical magnetosphere model. The fits to the polarization geometry using such models are shown by the dashed (red) contours.

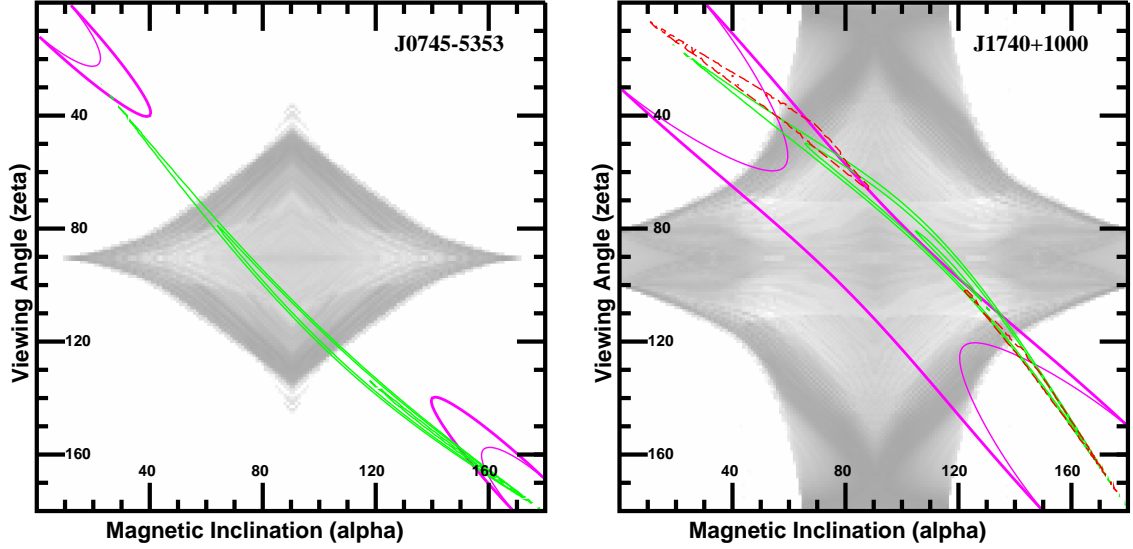


Figure 7.15: Figure taken from Romani et al. (2011). The γ -ray fit map for sub-luminous pulsars without parallax distances in the $\alpha-\zeta$ plane with radio polarization and pulse width constraints. For geometries away from the gray background, the sources are not expected to have strong outer magnetosphere γ -ray pulses. “Good” fits here are in white regions because of the sub-luminous nature of the pulsars. The PSR J1740+1000 data suggest large emission altitude requiring numerical modeling; the locus of best fits for these models is shown by the dashed (red) contours.

see Section 3.3.

Figure 7.13 is an example of the use of multi-wavelength data to strongly constrain the geometry of a pulsar. The pulsar modeled here is the Vela pulsar (PSR B0833–45 or PSR J0835–4510). The pulsar is modeled with γ -ray data, radio polarization data, opening angle constraints as well as X-ray pulsar wind nebula torus fitting (see Section 4.3.1). multi-wavelength data of Vela is used to strongly restricts the possible parameter space and similar modeling is done for the sub-luminous pulsars. The magenta contours represent limits imposed by beaming geometry. Thin magenta lines represent W_1 constant where models with a pulse width that would accommodate the data are in either corner of the fitting plane. For the W_{10} constraint, the models are limited to those within the thick magenta lines. The green and red contours show the lowest χ^2 regions for polarization model fitting.

Unfortunately, none of the other pulsars have clear X-ray pulsar wind nebula tori which are strong constraints on the parameter space. Four of the pulsars analyzed using polarization have parallax distances available (PSR J0358+5413, PSR J0538+2817, PSR J0659+1414, and PSR J1932+1059) and two do not have parallax distances available (PSR J0745–5353 and PSR J1740+1000). The fit maps of Figures 7.14 and 7.15 show regions with γ -ray model gap width of $w \approx L_\gamma/\dot{E}$. The grey background is the fit map of the γ -ray model to a generic single peak pulse except for PSR J0659+1414 for which γ -ray data is available. The darker the region, the better the fit. Note though that because the pulsars are sub-luminous, the best fit regions are those that are white regions, since no γ -rays are present for these models. Blue contours are polarization fit regions from the literature.

In the fitting results of PSR J0358+5413, the RVM favored $\alpha > 110^\circ$. Additionally, with W_1 constraint, $\alpha > 130^\circ$ and $\zeta > 140^\circ$. The W_{10} constraints are not more restrictive than the RVM fitting results. The pulsar PSR J0358+5413 could be sub-luminous but some non-sub-luminous geometries are also plausible.

For PSR J0538+2817, the acceptable parameter space given by the RVM fit is rather large as can be seen in Figure 7.14. However, the combination of the RVM contours and the W_1 and W_{10} constraints are much more restrictive. With the W_1 constraint, the possible models are confined to $\alpha < 35^\circ$ and $\zeta < 50^\circ$. The numerical finite-altitude fits are included for this pulsar on the figure in red dashed contours. These fits again favor smaller α and ζ where one would not expect outer gap emission in γ -rays. In contrast, the jet-like feature of the X-ray pulsar wind nebula does suggest $\zeta \approx 90^\circ$ but are too faint to do a formal fit with the torus model (Romani & Ng, 2003; Ng et al., 2007).

PSR J0659+1414 was previously studied in the radio polarization (Lyne & Manchester, 1988; Everett & Weisberg, 2001; Weltevrede et al., 2010a) and the results of Everett & Weisberg (2001) are included in blue on the figure. In our fits to RVM, the model favored $\alpha < 80^\circ$ but the pulsar has extended emission well beyond the main peak such that including the W_1 restriction gives $\alpha < 35^\circ$. The goodness of fit given in the figure is for a two-pole caustic γ -ray model fit to the *Fermi* Large Area Telescope data available for this pulsar. The outer gap model emission best fits

are restricted to $50^\circ < \alpha < 130^\circ$ and are well beyond the restrictions of the strongly extended emission seen in this pulsar.

The fitting of the polarization data of PSR J1932+1059 prefers $\alpha < 60^\circ$. However, the additional constraints of W_{10} prefers $\alpha < 20^\circ$ and W_1 prefers $\alpha < 15^\circ$. The RVM fitting contour from Everett & Weisberg (2001) is also included on Figure 7.14. Our analysis would then imply strongly that this pulsar is sub-luminous through geometry although this pulsar has a low \dot{E} such that the γ -ray emission may have turned off.

PSR J0745–5353 does not have a defined parallax distance and thus can not be definitively categorized as sub-luminous. From the Cordes & Lazio (2002) model, the pulsar has a distance of 0.25 kpc but a distance of 7.1 kpc from Taylor & Cordes (1993). The pulsar is sub-luminous if its distance is less than 2 kpc. In the combined restriction of RVM and W_{10} , $\alpha > 150^\circ$ and in the combined restriction of RVM and W_1 , $\alpha > 160^\circ$. Thus if PSR J0745–5353 was known to be close enough for detection, it would be a sub-luminous pulsar.

The pulsar PSR J1740+1000 also does not have a parallax distance but does have a strong dispersion measure distance (Section 3.2). Both RVM and single-altitude numerical model fitting was performed on the radio polarization position angle data. For W_{10} and RVM modeling, $\alpha < 70^\circ$ or $\alpha > 120^\circ$ is preferred. For W_1 and RVM modeling, $\alpha < 50^\circ$ or $\alpha > 140^\circ$ is preferred. For W_1 and single-altitude modeling, $\alpha < 30^\circ$ or $\alpha > 150^\circ$ is preferred. So although the pulsar could possibly not be detected due to geometry, the parameters are not restrictive enough to test the model.

In conclusion, this paper attempted to determine whether the non-detection of these pulsars in the γ -rays is due to beaming direction and high altitude emission of the outer gap model. Although the pulsars all showed evidence of being sub-luminous due to geometry, none were ruled out as low-level γ -ray emitters that will yet be detected with increased *Fermi* Large Area Telescope exposure and pulsed searches.

7.6 Conclusions

In this chapter, several papers are reviewed which take advantage of the polarization data to better understand the nature of pulsars. From the work in these papers,

we can see the important role of the polarization modeling for radio position angle measurements. Both numerical models and RVM were utilized in these studies. Often times, the rotating vector model is a helpful and easy-to-used model to interpret polarization when applied to suitable data. Additionally, we see the importance of using polarization data in connection to other wavelengths.

Chapter 8

Inward-Directed Photons

8.1 Exploring Inward-Directed Photon Emission Using Radio Polarization Data of PSR J1057–5226

This section is based on work done for “Exploring Inward-Directed Photon Emission Using Radio Polarization Data of PSR J1057–5226”

We apply a bidirectional model with both outward-directed photons and inward-directed photons to understand the complex radio polarization data of PSR J1057–5226 (PSR B1055–52). PSR J1057–5226 radio polarization data matches well to this model when one of the components of the polarization sweep is associated with inward-directed photon emission. Additionally, we discuss previous studies of PSR J1057–5226 in relation to our current study and past applications of models with inward-directed photons. We apply γ -ray models restricted by best fit parameters from the radio modeling. Although possible solutions exist, results do suggest we have not fully identified the location of the emission within the magnetosphere with the simplest γ -ray modeling assumptions.

8.1.1 Introduction

Pulsars have strong magnetic fields that are tied fundamentally to the emission observed from Earth. Charged particles follow the magnetic field lines before emitting

curvature radiation. The projected position angle of such radiation is a means of observing directly the geometry of the pulsar magnetic field and is a powerful tool for understanding the magnetosphere and the emission mechanism of the pulsar.

A large number of pulsars have S-shaped polarization position angle sweeps (versus phase). A simple analytical formula which assumes the pulsar is a vacuum point dipole predicts these S-shaped sweeps. This model is called the rotating vector model (RVM, Radhakrishnan & Cooke, 1969). Given the simplicity of the model, it works surprisingly well for quite a number of pulsar position angle data sets (i.e. Lyne & Manchester, 1988, Phillips, 1990, Everett & Weisberg, 2001).

Nevertheless, for other pulsars, the polarization does not adhere to this smooth S-shape form and has jumps and cusps that fundamentally can not be explained using such a simple model (i.e. Yan et al., 2011, Everett & Weisberg, 2001). Few studies have attempted to understand in-depth this difficult data but polarization is a powerful tool for understanding the emission of pulsars even for “messy” radio polarization sweeps. Further, pulsars with complex polarization tend to be high energy pulsars seen in the γ -rays and thus understanding these complicated polarization sweeps will contribute to understanding pulsars in multi-wavelength studies (e.g. Keith et al., 2012). Overall, developing models for this complicated and little understood polarization has great potential for elucidating the geometry and emission of the pulsars.

In a previous paper (Craig, 2014), our aim was to build on the simple rotating vector model (RVM). We numerically calculated polarization from finite altitude with and without orthogonal mode jumps (Backer et al., 1976). RVM accurately predicts only emission from the surface of the point neutron star, an altitude of zero, because of the lack of relativistic considerations. The addition of finite altitude also allows for multiple-altitude models with emission from multiple areas in the pulsar magnetosphere. The addition of multiple altitudes explains well a number of the jumps seen in the complex polarization data. (A jump in a polarization sweep for example can be seen in Figure 8.3 between the polarization associated with intensity peaks C_2 and C_3 .)

In Craig (2014), we illustrated our model by fitting the model to a number of pulsars. One of these pulsars was PSR J1057–5226. The polarization of the trailing

component of the P_1 pulse (labeled as C_3 in Figure 8.3) which appears to have a jump in the polarization when compared to the rest of the sweep was not modeled. In this current paper, this component is treated as “backward” emission. In adhering to a modified geometrically based model, this inward-directed photon emission is calculated using the field lines of the typical dipole but aimed in the opposite direction of the typical outward-directed photon. The addition of polarization from inward-directed photon emission is the natural next step for a model based on geometry and guided by data.

In this current paper, we will fit the pulsar radio polarization data and γ -ray data and argue that PSR J1057–5226 has atypical emission that makes it a particularly interesting candidate for inward-directed photon emission. Figure 8.1 illustrates the configuration of pulsar PSR J1057–5226 with bidirectional photon emission. We will discuss the formal fitting of the polarization data for PSR J1057–5226 in Section 8.1.4 along with fitting of the γ -ray data. In Section 8.1.2, we review past studies on PSR J1057–5226. In Section 8.1.3, we review previous studies that consider bidirectional emission.

8.1.2 Previous Work with PSR J1057–5226

The pulsar PSR J1057–5226 (also known as PSR B1055–52) is a relatively young pulsar ($P = 197.11\text{ms}$) with emission in the radio and γ -rays. In radio, PSR J1057–5226 exhibits two pulses with an approximate 180° separation in phase. The γ -rays have been studied using the outer gap and the two-pole caustic models (Romani & Watters, 2010). Weltevrede & Wright (2009) have studied PSR J1057–5226 in radio; they applied the RVM to the radio position angle polarization data and applied opening angle arguments to map the polar cap emission region. With these models, they were forced to conclude that some emission originates from field lines outside the formal dipole open zone cap. This cap is defined by field lines on the neutron star surface that extend outside of the light cylinder (characterized by a cylindrical distance, R_{LC} , at which particles would have to travel faster than the speed of light to co-rotate) and do not close. They also applied the analytic Blaskiewicz, Cordes, Wasserman (BCW,

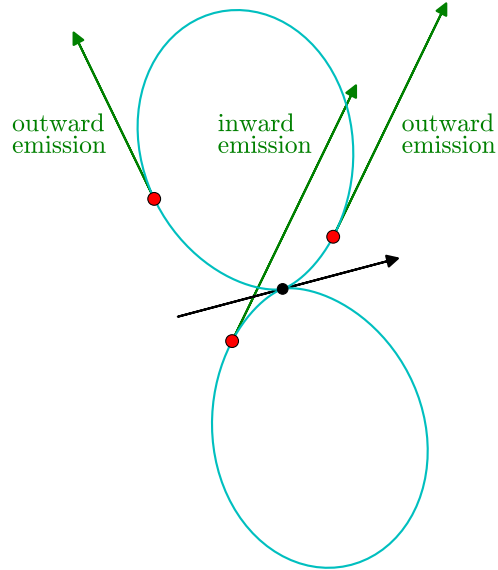


Figure 8.1: Sketch of a pulsar magnetosphere illustrating the use of inward-directed photon emission to explain unusual polarization of PSR J1057–5226. The rotation axis is vertical. Green lines are emission from various regions of the magnetosphere originating at red dots. Two regions emit the typical outward-directed photons and another region emits inward-directed photons. All three arrows have the same line of sight angle from the spin axis and thus all three will be seen by a single observer. In terms of phase, the observer will see emission from the “outward” emission on the right side of the diagram followed quickly by the “inward” emission for a counter-clockwise spinning pulsar. The pulsar will then swing around and the “outward” emission on the left side of the diagram will be in the line of sight of the observer. Thus the observer will see two pulses in the pulsar emission although one of the pulses contains both inward-directed photons and outward-directed photons each from a separate pole. This configuration is the one that is supported by polarization data for PSR J1057–5226 and the diagram is a simplified version of Figure 8.2.

Blaskiewicz et al., 1991) formulation to approximate different altitudes for the two pulses of emission.

In a previous paper (Craig, 2014), we applied a numerical geometrically-based model to an updated polarization position angle sweep of PSR J1057–5226. Such a model can accurately produce polarization sweeps of much greater heights than the simplistic BCW formulation. Craig & Romani (2012) calculated break-down altitudes to be $\sim 0.05\text{--}0.12R_{LC}$ for BCW (depending on geometric parameters and intensity models). The data could be modeled with emission originating mostly from within the open zone of the magnetosphere but at altitudes near the formal light cylinder. The data could also be modeled at lower altitudes with emission originating from well within the closed zone of the magnetosphere.

Additionally, the updated polarization position angle data used in Craig (2014) revealed an additional piece of polarization previously not noted in Weltevrede & Wright (2009). In Craig (2014), we were unable to fit this piece of polarization even with multiple altitudes and orthogonal mode jumps (Backer et al., 1976).

Weltevrede et al. (2012b), a follow-up paper to Weltevrede & Wright (2009), has a detailed analysis of the periodic modulation of PSR J1057–5226. They found that for the 20 period modulation, the two pulses of PSR J1057–5226 have a 2.5 period phase-locked delay. If the two pulses originate from separate poles, this delay can not be easily or simply explained. Either there must be some form of communication between the poles, the emission originates from a single pole, or some external factors are at play. See Weltevrede et al. (2012b) for a discussion summarizing these possibilities.

8.1.3 Previous Work in Bidirectional Emission

Bidirectional emission was suggested for pulsar radio emission in general by Dyks et al. (2005b). Bidirectional emission is emission with both an outward-directed photon component and an inward-directed photon component and is also called backward or downward emission. The inward-directed emission originates from one pole but instead of being directed outward from the neutron star, it is directed into the typical cone of emission and is therefore seen at a phase that one would expect emission from the opposite pole. In recent years, bidirectional emission has been suggested for a number of pulsars.

Figure 8.1 offers a visual representation of bidirectional emission. In the figure, the black arrow is the magnetic axis, the cyan loops are a pair of field lines, and the rotation axis is vertical (not shown). The red points represent regions where emission is produced and the green arrows represent the path of a photon traveling tangent to the field line. All three emission projections marked by the green arrows will be visible to a single observer during the rotation of the pulsar. The “outward” emission will be seen as the typical two pulses of the pulsar. The “inward” emission will be seen near in phase to the “outward” emission on right side of the diagram even though this “inward” emission originates from the opposite pole.

Dyks et al. (2005b) argued for bidirectional emission in the pulsar PSR B1822–09. The interpole component of the pulsar radio profile disappears when the precursor component of the main pole emission appears and vice versa (Gil et al., 1994). This behavior suggests some interpole communication or perhaps bidirectional behavior. In Dyks et al. (2005b), they estimated the radial distance of the emission based on phase lag between the inward-directed and outward-directed photon emission assuming both emission components come from the same region. They also estimated α (angle between rotation axis and magnetic axis) based on observing both components. Further, they argue that inward-directed photon emission components are more common than recognized because one does not always see both inward-directed and outward-directed photon emission components but only the nulling of the visible component.

PSR B0950+08, PSR B1929+10, and PSR B0437–4715 were suggested to have bidirectional emission by Dyks et al. (2005a). These three pulsars are so-called “notched” pulsars (McLaughlin & Rankin, 2004) because in radio intensity two notches of emission appear on the leading side of the main pulse, one partially embedded in the main pulse and the other several degrees before the main pulse. Wright (2004) argued for a model where an obscuration in the magnetosphere along with multiple altitudes causes the double notch emission. Dyks et al. (2005a) created a model where inward-directed photons are the source of this emission and the pulsar itself is the obstruction. In later papers however, they favor other models to explain the double notches (Dyks et al., 2007; Dyks & Rudak, 2012).

In Weltevrede et al. (2007), the interaction of the two pulses of PSR B1702–19 is explored. The pulsar radio intensity periodically brightened every 10.4 periods. The main pulse modulation lags the interpulse modulation by 0.43 periods. One explanation for this phase-locked behavior is bidirectional emission where the interpole component actually originates from inward-directed photon emission in the same region of the magnetosphere as the outward-directed photon emission of the main pulse. In the paper, the authors also discuss other possible explanations such as a single wide pole. They also discuss possible geometrical configurations needed for bidirectional emission in PSR J1057–5226 and PSR B1822–09 based on observed periodic intensity modulations of these pulsars.

Weltevrede et al. (2012a) found that the pulsar PSR J1057–5226 has a phase-locked delay of 2.5 periods between the pulses for the observed modulations that occur every 20 periods. As pointed out in Weltevrede et al. (2012a), a phase-locked delay of 2.5 periods for the pulsar PSR J1057–5226 is far too long to be simply explained by the time-of-flight delay of bidirectional emission. But as pointed out in Weltevrede et al. (2012b) such a delay could be caused by magnetospheric reflection or drift (Wright, 2003 and Melrose & Yuen, 2012). We discuss this further in Section 8.1.6.

8.1.4 Modeling Data of PSR J1057–5226

Fitting Procedure for Polarization Position Angle Data

The model used in this paper is the same finite-altitude (measured radially from the neutron star center), geometrically-based model as used in Craig (2014). Craig (2014) contains a more detailed description of the model and its nuances. The allowed range of fit altitude was $R = R_{\text{NS}}$ to $0.9R_{\text{LC}}$ where R_{NS} is the neutron star radius for PSR J1057–5226. The angles α , the angle between the spin axis and magnetic axis, and ζ , the viewing angle measured from the spin axis were held fixed in 1° intervals while all other parameters varied. The other fit parameters were the horizontal and vertical offsets ($\Delta\phi$ and $\Delta\psi$) and the altitudes (R_{C_1/C_2} , R_{C_3} , and R_{P_2}). The parameters $\Delta\phi$ and $\Delta\psi$ shift the polarization position data relative to the model horizontally and vertically. Although these parameters contain important physical information (the

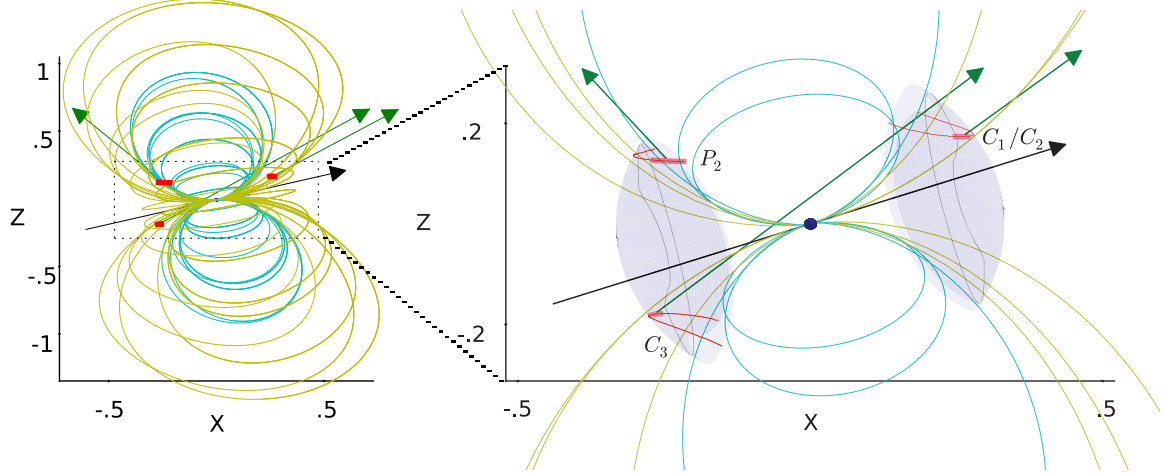


Figure 8.2: The left panel shows a visualization of the pulsar model at parameters for which χ^2 is minimized assuming a single altitude of bidirectional emission for PSR J1057–5226. The symbols C_1/C_2 , C_3 , and P_2 label the geometrical emission sites of various polarization position angle sweep pieces as seen in Figure 8.3. The regions C_1/C_2 and P_2 are assumed to originate from outward-directed photons on opposite poles while C_3 originates from inward-directed photons on the same pole as P_2 . For this particular model $\alpha = 77^\circ$. The cyan magnetic field lines are the last closed field lines with $\rho_{\text{ypt}} = 0.45R_{\text{LC}}$ and the yellow magnetic field lines are the last closed field lines with $\rho_{\text{ypt}} = 1R_{\text{LC}}$. The red lines and green arrows highlight regions of emission seen for $\zeta = 44^\circ$ and $R_{C_1/C_2} = R_{C_3} = R_{P_2} = 0.35R_{\text{LC}}$, the best fit configuration for a single-altitude model. The right panel is a close up of the pulsar with fewer magnetic field lines (yellow and cyan lines). The transparent caps represent regions of open field lines at $R = 0.35R_{\text{LC}}$ and $\rho_{\text{ypt}} = 0.45R_{\text{LC}}$. The region enclosed in the thin black line on the caps represent the region of open field lines with $\rho_{\text{ypt}} = 1R_{\text{LC}}$ (the classical vacuum cap). Thick curved red lines on the caps represent regions from which we do see emission while thin curved red lines are regions that we could see emission from for $\zeta = 44^\circ$. The rotation axis is vertical.

phase of closest approach of the magnetic axis and the absolute position angle of the magnetic axis on the plane of the sky), they are not reported here and are treated more as nuisance parameters. Additionally, phase of zero in the radio polarization model is the same as phase of zero in the γ -ray model (see Section 8.1.5). The altitudes are measured radially from the center of the pulsar and are the distance at which photons are emitted tangent to the magnetic field lines. The magnetic field line structure used here is that of a relativistic rotating point dipole given in Kaburaki (1980). A simulated annealing scheme was used to minimize χ^2 (Flannery et al., 1992) and to randomly sample the fit parameter space within 3σ of the χ^2_{min} and calculate fit error bars. We also allowed for orthogonal mode jumps.

In this paper, as in Craig (2014), we use the parameter ρ_{ypt} . This parameter is the cylindrical distance required of the last closed field line (or the y-point) for all emission seen in the data to originate from open field lines. For the classical vacuum dipole model, $\rho_{\text{ypt}} = 1R_{\text{LC}}$. In terms of emission phase, the smaller the ρ_{ypt} , the more time or phase an observer should see signal from the pulsar for any given pulsar configuration.

We will also refer to the value $\Delta\rho = \rho_{\text{ypt}} - \rho_{\text{max}}$. The value ρ_{max} is the maximum cylindrical distance of the model emission from the neutron star center (the maximum cylindrical altitude of the model; whereas, R_{C_1/C_2} , R_{C_3} , and R_{P_2} are radial distances).

In modeling PSR J1057-5226 data, we assume that radio emission identified as C_1 and C_2 in Figure 8.3 originates from the “main pulse” pole of the pulsar. Here the main pulse pole is the one that has the closest approach to the observer. The “interpulse” pole is then the pole from which the emission identified as C_3 and P_2 originates. This definition is contrary to the one used in Weltevrede & Wright (2009) in which the pulse labeled as P_1 in the current paper is the “interpulse” and P_2 is the “main pulse”. The pulse P_2 was likely chosen as the “main pulse” because it contains the peak of largest intensity. Also note that Weltevrede & Wright (2009) used a different geometric angle convention from the current paper and must be converted to make direct comparisons. See Everett & Weisberg (2001) for an explanation and the conversion formula.

Table 8.1: Fit parameters for PSR J1057–5226 (Bidirectional Emission)

DOF	(unreduced)	χ^2_{\min}	α ($^\circ$)	ζ ($^\circ$)	R_{C_1/C_2} (R_{LC})	R_{C_3} (R_{LC})	R_{P_2} (R_{LC})
3 Alt 228 – 7	406	$76^{+7(+7)}_{-3(-6)}$	$44^{+21(+24)}_{-3(-5)}$	$0.40^{+0.06(+0.08)}_{-0.21(-0.28)}$	$0.47^{+0.15(+0.21)}_{-0.36(-0.41)}$	$0.44^{+0.07(+0.17)}_{-0.35(-0.38)}$	
2 Alt 228 – 6	410	$77.4^{+1.2(1.6)}_{-4.6(-7.4)}$	$52.4^{+12.4(+15)}_{-12.2(-13.8)}$	$0.34^{+0.07(+0.09)}_{-0.14(-0.18)}$	$0.32^{+0.19(+0.25)}_{-0.17(-0.20)}$		
1 Alt 228 – 5	419	$76.6^{+0.8(+1.2)}_{-0.6(-1.0)}$	$47.6^{+5.4(+8.2)}_{-3.6(-4.8)}$	$0.35^{+0.05(+0.07)}_{-0.02(-0.03)}$			

Note. — Errors reported without (with) parentheses are for 1σ (3σ) from χ^2_{\min} .

We fit the polarization data for PSR J1057–5226 assuming that (1) the altitude for all three components (outward-directed photon emission component from the main pulse, outward-directed photon emission component from the interpulse, and inward-directed photon emission component from the interpulse) are different; (2) the altitude for the outward-directed photon emission component from the interpulse and inward-directed photon emission component from the interpulse are the same; and (3) the altitude from all three components are the same. For all fits, the polarization associated with the inward-directed photon emission is orthogonally mode jumped compared to the other components. Figures 8.2 and 8.3 both label the outward-directed photon emission component from main pulse as C_1 and C_2 , the outward-directed photon emission component from interpulse as P_2 , and the inward-directed photon emission component from interpulse as C_3 . The corresponding altitudes in the model are R_{C_1/C_2} , R_{C_3} , and R_{P_2} . The altitudes of C_1 and C_2 are assumed to be the same since the polarization sweep between the two components is smooth. Further, we will refer to the emission location of the two components as C_1/C_2 here on out.

Fitting PSR J1057–5226 with Inward-Directed Photon Constraints

In Figure 8.3, the best fit single-altitude model overlays the polarization data of PSR J1057–5226. Red data points match well to outward-directed photon model

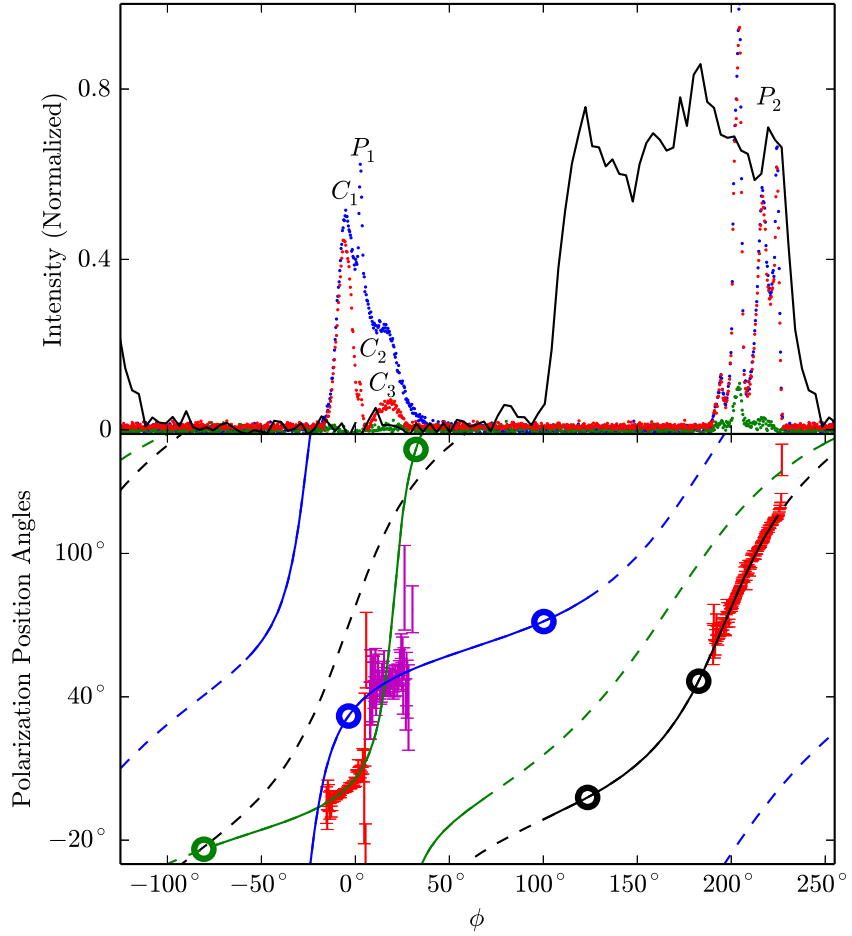


Figure 8.3: In the upper panel, blue points are total radio intensity data for 1.5GHz, red points are linear polarization intensity data and green points are circular polarization intensity data for PSR J1057–5226. Black solid line is γ -ray light curve for emission greater than 0.1 GeV. In the bottom panel, red data points with error bars are polarization position angles in the outward-directed photon emission component (and RVM fit). The magenta data points with error bars are polarization position angles included in the inward-directed photon emission component, P_2 . The model polarization comes from a fit with (unreduced) $\chi^2 = 419$ and parameters $\alpha = 77^\circ$, $\zeta = 48^\circ$, and $R_{C_1/C_2} = R_{C_3} = R_{P_2} = 0.35R_{\text{LC}}$. The green and black lines are the model polarization for outward-directed photon emission but from opposite poles. The blue line is the model polarization of an inward-directed photon emission component from the same pole as the black line. Empty circles mark limiting phase of emission from open field lines with $\rho_{\text{ypt}} = 1R_{\text{LC}}$. Solid lines mark allowed emission phase for an effective open zone with $\rho_{\text{ypt}} = 0.45R_{\text{LC}}$ which is required for the model phase to cover all of the emission phase in the data. Phase of zero is the point of closest encounter to the magnetic axis in the model.

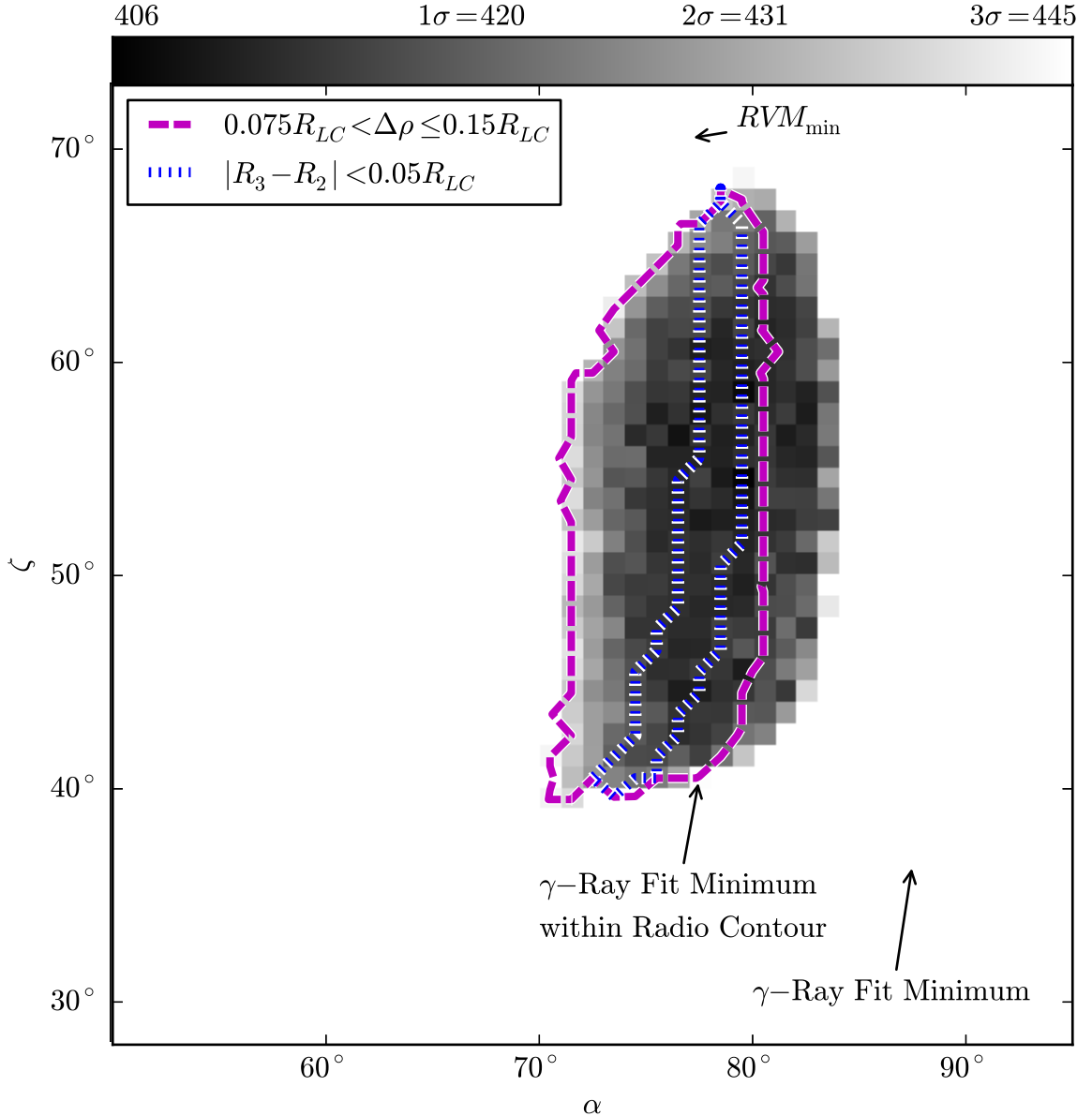


Figure 8.4: Map of (unreduced) χ^2 in the α - ζ plane for a three-altitude fit to the polarization data of PSR J1057–5226. Blue contour shows the 3σ region above χ^2_{\min} for emission from the same pole (one outward-directed and one inward-directed) with similar altitudes (R_{C_3} and R_{P_2}). The magenta contour shows the 3σ region above χ^2_{\min} for largest $\Delta\rho$ (the cylindrical distance from the largest emission distance to ρ_{ypt}).

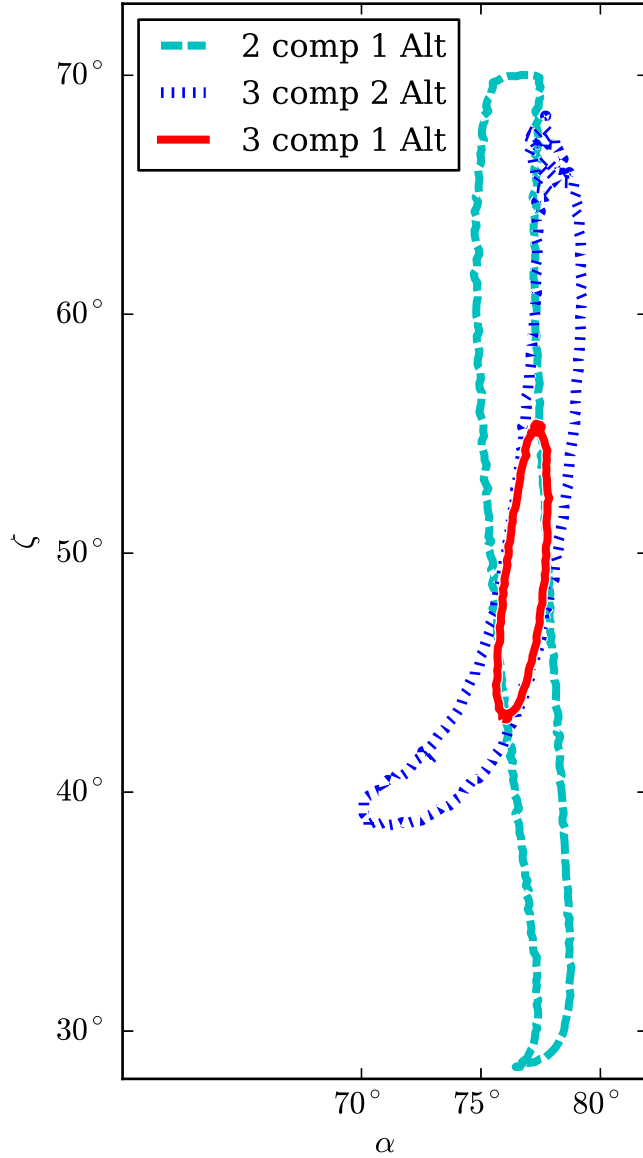


Figure 8.5: Contours of 3σ region above χ^2_{\min} for three different fits to the polarization data for PSR J1057–5226 in the α - ζ plane. Cyan contour is the 3σ contour for fitting the two outward-directed photon emission components (red data points with error bars only, as seen in Figure 8.2) with a single altitude ($R_{C_1/C_2} = R_{P_2}$). The blue contour is the 3σ contour for the fit with both the two outward-directed photon emission components and the one inward-directed photon emission component with a single altitude for C_1/C_2 components and another for the C_3 and P_2 components as labeled on Figure 8.2 ($R_{C_3} = R_{P_2}$). The red contour is the 3σ contour for a single-altitude fit such that $R_{C_1/C_2} = R_{C_3} = R_{P_2}$ with inward-directed photon emission for component C_3 . By assuming a single altitude, allowed parameter space is strongly constrained. Even with a two-altitude fit, α is strongly constrained.

Table 8.2: Measured Parameters for PSR J1057–5226 (Bidirectional Emission)

	$\Delta\rho$ (R_{LC})	ρ_{\max} (R_{LC})	ρ_{ypt} (R_{LC})
3 Alt	$0.12^{+0.02(+0.02)}_{-0.12(-0.12)}$	$0.39^{+0.08(+0.16)}_{-0.21(-0.26)}$	$0.51^{+0.07(+0.14)}_{-0.35(-0.48)}$
2 Alt	$0.12^{+0.01(+0.02)}_{-0.05(-0.06)}$	$0.29^{+0.16(+0.22)}_{-0.11(-0.15)}$	$0.41^{+0.17(+0.23)}_{-0.15(-0.16)}$
1 Alt	$0.12^{+0.01(+0.01)}_{-0.01(-0.01)}$	$0.34^{+0.02(+0.03)}_{-0.03(-0.05)}$	$0.46^{+0.02(+0.03)}_{-0.03(-0.05)}$

Note. — Errors reported without (with) parentheses are for 1σ (3σ) from χ^2_{\min} .

polarization. This polarization (outward only) also matches reasonable well to the RVM model, $\chi^2 = 325$ (unreduced, Degrees of Freedom = DOF = $166 - 4$). The best fit RVM model is labeled on Figure 8.4. The RVM fit is problematic because it requires emission from well within the closed zone of the pulsar magnetosphere (Weltevrede & Wright, 2009). Craig (2014) fit the red points (in Figure 8.3) with a finite-altitude model and found even better fits with altitudes either far from the neutron star or within the closed zone and fits in between these extremes. Unfortunately, this model was unable to model the data points in magenta. In the current paper, we explored the possibility that the magenta points originate from inward-directed photon emission.

Figure 8.4 shows the (unreduced) χ^2 surface in the $\alpha - \zeta$ plane for position angle data modeled using a three-altitude model with inward-directed photon emission for component C_3 . The lowest (unreduced) χ^2 was 406 with DOF = $228 - 7$. Table 8.1 shows best fit parameters as well as 1σ and 3σ error bars for those parameters. The blue contour of Figure 8.4 is the 3σ from χ^2_{\min} contour for models with similar R_{C_3} and R_{P_2} . Since component C_3 and P_2 are from the same pole, it is not unreasonable to assume they are from similar heights. The magenta contour is the 3σ from χ^2_{\min} contour of models with the largest $\Delta\rho$ (see Section 8.1.4 for definitions). Models with larger $\Delta\rho$ are more trustworthy since field lines close to the y-point will be distorted in manners not accounted for in our vacuum dipole model. The component P_2 drives this parameter to such small values while components C_1/C_2 and C_3 for the most part originate well away from the y-point cylindrical distance. Figure 8.3 illustrates this point well. Empty circles on the figure mark the expected phase of emission for the classical dipole open zone ($\rho_{ypt} = 1R_{LC}$). For this particular set of fit parameters

C_1/C_2 and C_3 data are both well within the classical open zone while P_2 data is entirely outside of this phase range.

Figure 8.5 shows the 3σ from χ^2_{\min} contour in the $\alpha - \zeta$ plane of a variety of fitting schemes. The cyan contour is the 3σ area in the $\alpha - \zeta$ plane of a fit done with only C_1/C_2 and P_2 data and a single altitude. These are the outward-directed photon emission components. The blue contour represents the fit with all three components but with different altitudes for the different poles (C_3 and P_2 have the same altitude, similar to the blue contour on Figure 8.4). The fit represented with the blue and cyan contours both have large ranges of acceptable ζ . The red contour is the 3σ from χ^2_{\min} area for a fit with a single altitude, $R_{C_1/C_2} = R_{C_3} = R_{P_2}$. Not surprisingly, this is roughly the overlap of the cyan and blue contours. Further, unlike the blue and cyan contours, the red contour (representing the assumption of a single altitude) greatly restricts the possible ζ range.

Table 8.1 compares fit parameters assuming one, two, and three altitudes. χ^2_{\min} did not drastically change by adding new free parameters (additional altitudes) nor did the best fit parameters shift drastically. Table 8.2 shows parameters that can be measured from the model fitting. Again these measured parameters remain the same for different numbers of altitudes although the allowed range of the parameters decreases with fewer fit altitudes.

Fitting PSR J1057–5226 with Outward-Directed Photon Emission

We will briefly discuss fit results of simulations with only outward-directed photon emission. We fit with a three-altitude model assuming that the emission for C_1/C_2 , C_3 , and P_2 all originated from photons directed away from the neutron star center. The lowest (unreduced) $\chi^2_{\min} = 435$ (DOF = 228 – 7). For this fit, $\alpha = 79^\circ$, $\zeta = 35^\circ$, $R_{C_1/C_2} = .54R_{LC}$, $R_{C_3} = .86R_{LC}$, and $R_{P_2} = .5R_{LC}$. The χ^2_{\min} is just inside the 3σ contours of the three-altitude fit assuming an inward-directed photon emission component; the χ^2 increases significantly within a couple of degrees of this χ^2_{\min} at $\alpha = 79^\circ$, $\zeta = 35^\circ$. Statistically, the bidirectional model is better suited to the data over a larger region of parameter space and it is visually more satisfying.

Visualizing the Pulsar Configuration

Figure 8.2 shows one possible configuration of the pulsar with inward-directed photon emission for component C_3 and that produces position angle polarization sweeps similar to the data (see Section 8.1.4 for more details on the fitting procedure). This particular configuration produces the best fit χ^2 assuming emission from a single altitude ($R_{C_1/C_2} = R_{C_3} = R_{P_2}$).

In the figure, the yellow field lines are last closed field lines with $\rho_{\text{ypt}} = 1R_{\text{LC}}$, and the cyan field lines are those with $\rho_{\text{ypt}} = 0.45R_{\text{LC}}$. For all emission from the P_2 component to originate from open field lines, $\rho_{\text{ypt}} = 0.45R_{\text{LC}}$. The grey areas in Figure 8.2 are the open field line caps at an altitude of $0.35R_{\text{LC}}$ and $\rho_{\text{ypt}} = 0.45R_{\text{LC}}$. The black lines on the caps are the boundary of the caps if $\rho_{\text{ypt}} = 1R_{\text{LC}}$. Note that the yellow field lines touch the black line boundary while the cyan field lines touch the grey cap boundary.

The red curves on the caps indicate the emission locations visible at $\zeta = 48^\circ$. Thicker (curved) red lines indicate regions of signal in the data for this given configuration (see Figure 8.3). The thick (curved) red line for P_2 goes to the edge of the grey cap; as discussed earlier, P_2 is the component that controls ρ_{ypt} . The large phase of emission requires a low ρ_{ypt} or a high altitude to accommodate the P_2 emission. In previous fitting that included only polarization data from C_1/C_2 and P_2 , we could find a few solutions with $\rho_{\text{ypt}} = 1R_{\text{LC}}$ (the classical dipole open cone of emission) within the 3σ contour from χ^2_{min} ; but with the addition of fitting C_3 data, these fits are no longer probable.

Green arrows from the curves indicate the direction of emission. The arrow from C_3 emission goes into the pulsar magnetosphere. Locations of C_3 and P_2 emission are on opposite sides of the same pole. This is necessary geometrically in order for the inward-directed and outward-directed photon emission to be visible from the same ζ .

8.1.5 Combining γ -Ray Fitting with Radio Polarization Model

One striking feature of the PSR J1057 – 5226 γ -ray data is the overlap in phase with the radio data. The upper panel of Figure 8.3 shows the γ -ray light curve in black

over the radio emission. The γ -ray light curve lines up with the P_2 pulse suggesting that both could be coming from similar locations in the magnetosphere. This is an unusual feature for pulsar emission and may give evidence to the seemingly unusual emission from the P_2 component.

γ -Ray Model Method

The γ -ray data was obtained from the *Fermi* LAT pulsar catalog (Abdo et al., 2010b, 2013). The data is from energies greater than 0.1 GeV. The γ -ray model is based on Romani & Watters (2010). The outer gap model has emission originating from inside the effective light cylinder (ρ_{ypt}) and beyond the null charge surface ($\mathbf{B} \cdot \boldsymbol{\Omega} = 0$). We use the same emissivity function ($e^{-[(s-2s_{\text{NC},\min}-1)/0.1]^2}$ for beyond a path length of $1+2s_{\text{NC},\min}$ and constant below, where s is the path length, $s_{\text{NC},\min}$ is the minimum path length of field lines at a given fraction of the polar cap, and units are in terms of R_{LC}) as Romani & Watters (2010). Emission was allowed for a range of effective w values from .01 to .12 where w is the fraction of the radial distance from the pole on the polar cap. Here we use an “effective” w in that the polar cap defined by the open field lines will shift based on ρ_{ypt} . A Gaussian width was applied to a given w slice of 0.02 (again similar to Romani & Watters, 2010).

γ -Ray Model Results

We limited our parameter space to α , ζ , $\Delta\phi$, and ρ_{ypt} within 3σ of the χ^2_{min} of the radio modeling results. Additionally, ρ_{ypt} obtained in the radio polarization fitting is an *upper* limit and the lower limit is set by the geometrical location of the radio emission with the largest cylindrical distance from the spin axis. We focused on fitting with only maximum ρ_{ypt} since smaller y-point distances revert the model to essentially a simple dipole. This in turn eliminates the caustics and box-like sides of the emission which are clearly seen in the data (see Figures 8.6 and 8.7 for data). In general, models with smaller ρ_{ypt} yield worse fits because of this. Further, fits with larger ζ ($\gtrsim 55^\circ$) tended to have smaller required ρ_{ypt} (from radio fits) and poorer χ^2 values due to this.

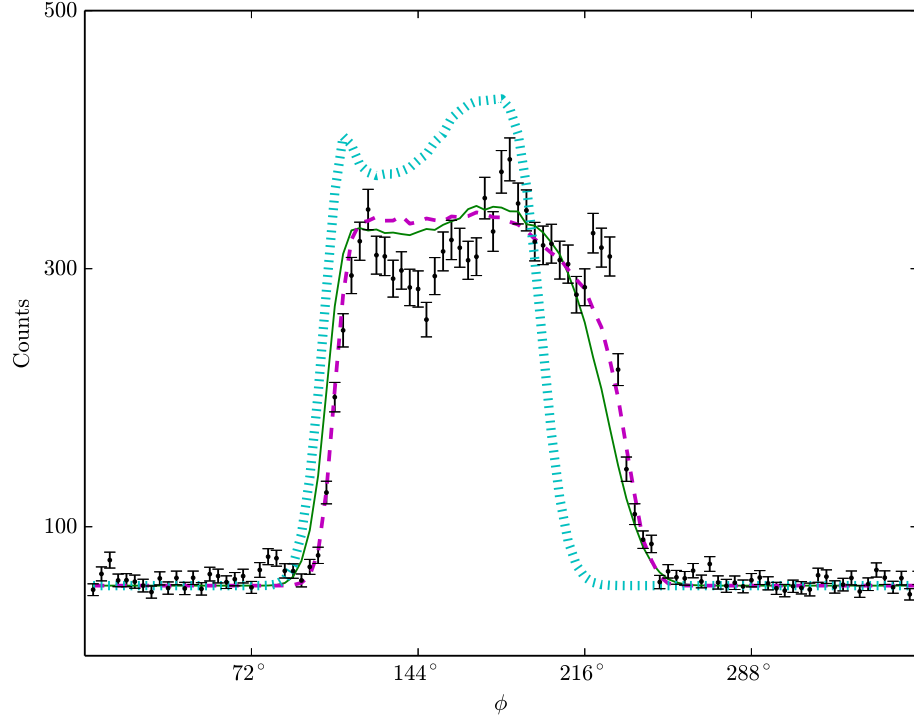


Figure 8.6: Black data points with error bars are γ -ray data for energy greater than 0.1 GeV. The magenta line is the best fit γ -ray light curve using extrapolated parameters. The green line is the best fit γ -ray light curve using parameters only within the 3σ from χ^2_{\min} space of the radio fit results. The cyan line is the best fit γ -ray light curve using the parameters at the best radio fit for a single-altitude model.

With this relatively simple γ -ray model and the radio fit restrictions, the best fit model is $\alpha = 77^\circ$, $\zeta = 40^\circ$, $w = 0.04$, with unreduced $\chi^2_{\min} = 695$. The degrees of freedom for the γ -ray fits are $\text{DOF} = 100 - 1$ since only w is being fit. Here the χ^2_{\min} in radio is 445 right at the 3σ cut off of the fits.

Admittedly, the γ -ray model is not exact, neglecting important plasma physics that can affect the field line structure, particularly at high altitudes, in addition to making simplistic assumptions about γ -ray production locations. Further, having the minimum χ^2 region for the γ -ray model close to the minimum in polarization is encouraging even if they do not exactly overlap and still indicates some real features

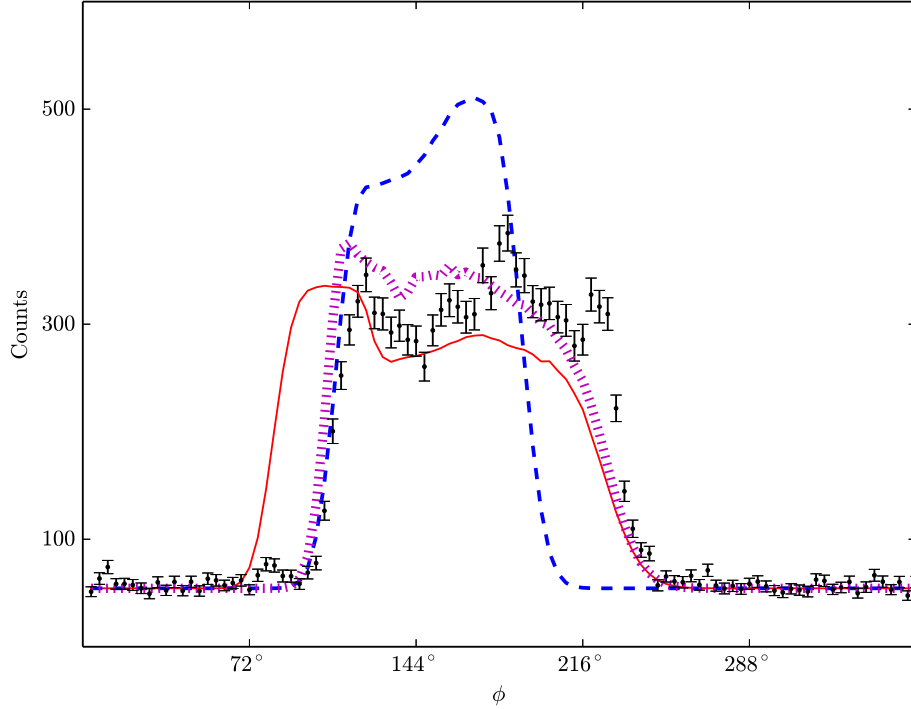


Figure 8.7: Black data points with error bars are γ -ray data for energy greater than 0.1 GeV. The blue line and red line are γ -ray light curves using the parameters at the best radio fit for a single-altitude model and $w = 0.15$ and $w = 0.06$. The magenta line is a γ -ray light curve from a model that illuminates field lines between $w = 0.15$ and $w = 0.06$ from one end of the light curve to the other. This model illustrates that better model light curves are possible in regions of the best fit radio models but they would require modifications to the prescription of illuminated field lines.

are being captured by the model. Since the minimum χ^2 of the γ -ray model is right at the 3σ edge of the χ^2 surface of the radio polarization fit, we are interested in the behavior of the γ -ray model beyond this region. Calculating χ^2 values of the γ -ray model using radio fit model values is not sensible since radio models beyond 3σ do not contain real information and are poor matches to the data. Instead, we expanded the allowed region around this fit space for the radio model within 3σ of χ^2_{\min} by extrapolating parameters using simple piece-wise linear fitting.

The lowest local unreduced χ^2 is 322 with $\alpha = 87^\circ$, $\zeta = 36^\circ$, $w = 0.02$ for fits

in the extrapolated region. Decreasing ζ further resulted in the worsening of χ^2 . Unfortunately the unreduced χ^2 for the radio is 3400, far beyond what would be statistically acceptable and visually unsatisfactory.

On Figure 8.4 is a marking for the lowest χ^2 from the γ -ray fitting both within the 3σ radio fit contour and without the contour. Ideally, the best fit γ -ray model would fall within the best fit parameter space of the polarization radio model. But considering the uncertainties of the γ -ray model, the lowest local γ -ray χ^2 is not dramatically far from χ^2 minimum area of the radio polarization fit. From this information we can conclude that a joint fit between radio and γ -ray data would fall around $\zeta \sim 40^\circ$.

Figure 8.6 shows the best fit light curves for within the 3σ contour of the radio results (green) and the local minimum fit in the γ -ray just beyond this contour (magenta). Both appear relatively flat compared to the data. Also plotted in the same figure in cyan is the best fit light curve at $\alpha = 77^\circ$, $\zeta = 48^\circ$ (unreduced $\chi^2 = 5000$, $\text{DOF} = 100 - 1$), the best fit values in the radio polarization for the single-altitude model. The model light curves are normalized to the total counts.

The *position* of the pulse using this γ -ray model matches the light curve position; the morphology of the peaks within the pulse are not matched. If w is not constant, models much more suited for the single-altitude polarization fit space in terms of pulse width are obtainable. Whether this would improve the morphology is unclear but certainly possible. At the moment, a prescription for a w that is variable is unclear.

To illustrate this point, we produced a light curve which varied between $w = 0.06$ and $w = 0.15$ (linearly with respect to magnetic ϕ). This light curve is plotted in Figure 8.7 over the data. The curve is not fit to the data but is meant simply as an illustration; undoubtedly, using a different prescription for field line illumination or slightly different α and ζ could result in better fits to the data in the 3σ parameters space of the radio data. But without a clear and physically motivated prescription, any curves would be purely ungrounded speculation. Also plotted in Figure 8.7 are light curves with constant $w = 0.06$ (solid, red) and $w = 0.15$ (dashed, blue).

We can therefore conclude that the γ -ray fitting favors smaller ζ but perhaps not quite as strongly as may be suggested by models where field lines of a single w

are illuminated. Either way, results suggest a lower ζ than that of RVM ($\alpha = 77^\circ$, $\zeta = 70^\circ$, ignoring the C_3 component) which is consistent with bidirectional, finite-altitude radio polarization fitting.

8.1.6 Discussion and Conclusions

Comparison to Weltevrede et al. (2007)

The bidirectional model of PSR J1057–5226 presented in Weltevrede et al. (2007) (Figure 12) is different from the one presented in the current paper. The configuration for PSR J1057–5226 is very similar to the one given for PSR B1702–19 in the same paper. Our particular configuration was motivated by the shape of the polarization curve while the configuration of Weltevrede et al. (2007) was motivated by modulations in the intensity. First, the model of Weltevrede et al. (2007) Figure 12 divides the emission of the pulse P_2 into a modulated and an unmodulated component. The paper Weltevrede et al. (2012b) does support P_2 having several different modulations among the peaks. Yet the polarization of P_2 is smooth and connected between the various components and thus the emission is very likely to come from the same location in the magnetosphere. Second, the model of Weltevrede et al. (2007) has the emission from the pulse we label as P_1 from a single location in the magnetosphere whereas in the model presented here the P_1 pulse is split into outward-directed photon emission and inward-directed photon emission. The motivation here was again driven by the polarization sweep. A clear disconnect exists between the polarization of components C_1/C_2 and the component C_3 . Considering these two pieces of polarization are from the same pole, whether the emission was from outward-directed photons (as discussed in Section 8.1.4) or from inward-directed photons (with and without multiple altitudes and orthogonal mode jumps), did not yield appropriate models. The best fit model with the pulse P_1 emitted wholly from inward-directed photons and P_2 emitted from outward-directed photons had an unreduced χ^2 of 786.

On the other hand, the polarization of C_1/C_2 and P_2 are well-defined with small error bars while the polarization of C_3 has larger error bars and is generally more noisy. It is then natural to assume that the emission of C_1/C_2 and P_2 is typical,

outward-directed photon emission and the emission of C_3 is unusual. Further, the emission of component C_3 is located after the phase of emission of components C_1/C_2 , the location where emission from inward-directed photons of the opposite pole would appear. Thus the model configuration used in this paper was a natural choice before any formal fitting was performed.

Comparison to Weltevrede & Wright (2009)

As noted earlier, Weltevrede & Wright (2009) analyzed polarization data of PSR J1057–5226. They use the RVM to calculate polarization sweeps. The magnetic field lines are simple vacuum dipole (RVM) but they included retardation and aberration effects to calculate the height estimations from BCW. In addition, they use pulse width arguments to calculate emission height. They estimate the altitude of emission from both poles is $0.07R_{LC}$. At this altitude, the polarization sweeps will not be drastically distorted (Craig & Romani, 2012) and RVM is appropriate to use assuming this altitude. Also at this altitude, the magnetic field lines in the numerical model will be essentially the same as RVM. Further, at low altitudes, polarization position angles for inward-directed photons and outward-directed photons will be similar. The polarization of VII as labeled in Weltevrede & Wright (2009) (corresponding to C_3 in the current paper) is unlikely to have strongly influenced the RVM polarization fitting since there are few data points for C_3 and these data points have larger error bars compared to the rest of the polarization sweep (as can be noted from Figure 2 of Weltevrede & Wright, 2009). With these considerations and if the numerical model used in the current paper were applied to the data of Weltevrede & Wright (2009) with a low altitude constraint, the polar cap map of Figure 7 in Weltevrede & Wright (2009) would be similar. The difference would be that the VII line section (the inward-directed photon emission) would be located in the upper left quadrant and on the same pole as the I-II-III-IV line section of the diagram.

In Weltevrede & Wright (2009), they describe the last closed field lines needed for the emission to originate from open field lines in terms of a footprint parameter. This footprint parameter is a measure of the cap size on the neutron star surface. In addition, for their favored configuration, they state that the last closed field line closes

at a distance of a quarter of a light cylinder radius (e.g. $\rho_{\text{ypt}} = 0.25R_{\text{LC}}$). For our best fit single-altitude models $\rho_{\text{ypt}} \sim 0.46R_{\text{LC}}$ and $R \sim 0.35R_{\text{LC}}$. The favored altitude of Weltevrede & Wright (2009) is $0.07R_{\text{LC}}$. Roughly, the model presented here is a natural extension of the Weltevrede & Wright (2009) model that allows larger finite altitude. Because our model allows larger altitudes, the needed ρ_{ypt} is consistently higher. Our $\Delta\rho_{\text{ypt}}$ (the cylindrical distance between the maximum emission distance and the effective light cylinder) is $\sim 0.12R_{\text{LC}}$. For Weltevrede & Wright (2009), we can estimate $\Delta\rho_{\text{ypt}}$ as $0.25 - 0.07 = 0.18R_{\text{LC}}$ which again is roughly consistent with the numerical model.

Comparison to Weltevrede et al. (2012b)

In Weltevrede et al. (2007), the authors argued for a bidirectional model for PSR B1702–19 based on phase locked modulation and include a schematic of a possible PSR J1057–5226 bidirectional model. However, in Weltevrede et al. (2012b), bidirectional emission models are avoided presumably because the phase locked modulation delay is too large for the simple time of flight delay for bidirectional emission from the same location in the magnetosphere. The model relies on emission from the exact same location in the magnetosphere for both inward-directed and outward-directed photons. For our model, the emission is from the same pole but on opposite sides of the pole. Thus a larger difference in modulation delay time may not be reasonable.

Further, the modulation reported in Weltevrede et al. (2012b) are present mostly in the peaks we label as C_1 and C_2 . These peaks (labeled as V and VI in Weltevrede et al., 2012b) are modeled as forward-directed photon emission. The trailing edge of the pulse (mostly the peak labeled as C_3 in the current paper and VII in Weltevrede et al., 2012b) does not participate in the $2.5P$ modulation. If the phase-locked modulation was connected to the bidirectional emission model presented here, the peak C_3 (modeled as originating from the inward-directed photons) should modulate with the P_2 peak.

Finally, the modulation in C_1 and C_2 and the lack of modulation in C_3 indicates that C_1 and C_2 are distinct from C_3 . This supports the bidirectional model since C_1 and C_2 come from the opposite pole compared to C_3 . In this model we would not

expect emission from these different peaks to modulate with one another.

Summary

The position angle polarization data for PSR J1057–5226 is inconsistent with the typical geometrically-based polarization model, RVM. Based on the data, RVM was modified to include orthogonal mode jumps, multiple finite altitude, and bidirectional emission. With these modifications, the produced polarization position angle sweeps are consistent with the data. Assuming a single altitude of emission greatly restricts the acceptable parameter space. The data still requires the y-point further in than the classical light cylinder distance but this atypical behavior may lend hints to the bidirectional nature of PSR J1057–5226.

Further, γ -ray modeling with a model of the simplest outer gap formulation is possible. The γ -ray models favor the smallest ζ values when restricted by radio model fitting parameters within 3σ of χ^2_{\min} . These models do capture the overall shape of the pulse but a more precise fit will likely require better understanding of the location of the γ -ray emission. Additionally, in our current model, we neglect plasma effects which might be important at the altitudes that are modeled here. Further, PSR J1057–5226 has unusual modulation patterns in its intensity. Surely, these modulation hold tantalizing keys to the pulsar emission and indicate atypical behavior; yet we are unable to incorporate these modulations in our model.

In brief, bidirectional emission is consistent with both radio and γ -ray data and is an exciting possibility for the unusual emission of the pulsar PSR J1057–5226.

We greatly thank S. Johnston for supplying radio data for PSR J1057–5226 (2012, private correspondence) and Roger W. Romani for valuable discussion. This work has been supported by the Stanford Office of the Vice Provost of Graduate Education DARE Doctoral Fellowship Program to H.A.C.

8.2 Exploring Inward-Directed Photon Emission Using Radio Polarization Data of PSR J1705–1906

This section is based on work done for private corresponds in relation to “Six Faint γ -Ray Pulsars Seen with the Fermi Large Area Telescope. Towards a Sample Blending into the Background” (Hou et al., 2014).

In the previous section, we discussed extensively the application of a bidirectional model to the data of PSR J1057–5226. We additionally applied the bidirectional model to the polarization position angle data of PSR J1705–1906 and will discuss the results in this section along with giving an overview of past studies of this pulsar. Overall, the results of the analysis of PSR J1705–1906 are not as compelling or conclusive as those of PSR J1057–5226 but are nevertheless reported here for completion.

8.2.1 Past Studies

The pulsar PSR J1705–1906 (PSR B1702–19) has been identified by Weltevrede et al. (2007) as a possible candidate for bidirectional emission. The second component of the main pulse (as labeled by Weltevrede et al. (2007) and the pulse with the highest intensity) and the interpulse have a phase locked delay. The main pulse modulation lags that of the interpulse by 0.43 rotation period, around the 0.5 rotation period expected from a geometric delay. These modulations occur approximately every 10.4 rotation periods.

Weltevrede et al. (2007) explored evidence of two-pole emission in the polarization data. As Weltevrede et al. (2007) noted, a U-shape in the interpulse polarization data is difficult to model and they fit the polarization data to the rotating vector model (RVM) both including and excluding this difficult section. They further restrict their fits using beaming radius and width of emission phase arguments. They also discuss a single wide cone model. For the RVM, emission from a single wide cone, from both poles, and from a single pole with bidirectional photons will have the same polarization sweep due to the lack of relativistic and sweep-back effects. In order to

create a single wide cone model they restrict ϕ (the location in phase of model phase zero) to vary between 125° and 215° . Fits with these constraints yield χ^2 far worse than those of a two pole model.

Further, Weltevrede et al. (2007) examined the inner and outer cone model of Gil (1985). With radius beam arguments, they estimate the difference in emission height between the two emission regions for this model to be 900 km ($0.064R_{LC}$) which should correspond to a difference in phase of 7° (see Section 3.3 for beaming model details). Any difference in phase between the interpulse and main pulse is much smaller and they therefore ruled out this model.

Finally for bidirectional emission, we would again expect a delay in phase for any configuration other than the simplest configuration. This is not seen in the data. The difference between the centroid of the interpulse and the minimum between the two main pulse components is nearly 180° . Alternatively, the phase difference between the two *modulating* components is 176° . Again using radius beam arguments and time delay arguments, Weltevrede et al. (2007) gave emission height estimates.

8.2.2 Polarization Analysis

Here we present our own analysis of the 1.408 GHz polarization data (Gould & Lyne, 1998) using the multiple-altitude model with bidirectional photon emission. Similar to Weltevrede et al. (2007), three scenarios are examined: emission from two poles emitting only forward-directed photons, emission from a single wide pole emitting only forward-directed photons, and emission from a single pole with bidirectional photons (both inward- and outward-directed). For the latter case, the peak identified as the interpulse is assumed to originate from inward-directed photons.

Figure 8.8 shows fit results for pulsar PSR J1705–1906 for the typical configuration with emission from two separate poles for the two different pulses. Figure 8.9 shows fit results for a configuration where emission originates from a single wide pole. Figure 8.10 shows fit results for a configuration where polarization of the “main pulse” as identified by Weltevrede et al. (2007) originates from outward-directed photons and

“interpulse” polarization originates from the same pole but from inward-directed photons. Also shown on the graphs are contours for high and low altitude cuts, classical open zone constraints ($\rho_{\text{ypt}} = 1R_{\text{LC}}$), and restricted y-point lowering constraints in which emission is allowed from the closed zone. Overall, the results are not very constraining. All three fits have $\chi^2_{\text{min}} \sim 60$ for $\text{DOF} = 22 - 5$. Also note that only a single altitude was applied for all components of the polarization sweep. Allowing for multiple altitudes would make the fitting even less constraining. The long, thin contour along the diagonal of the graphs is the RVM fit. For the RVM fitting, $\chi^2_{\text{min}} = 65$ such that the use of finite altitudes is not well justified statistically.

Although γ -ray fitting is not formally performed, Hou et al. (2014) notes using results from Watters & Romani (2011) some constraints to the fit parameters. They conclude that $\alpha > 50^\circ$ and $\zeta < 60^\circ$ although this too is not very constraining. Overall, better data is likely needed to make more meaningful conclusions about PSR J1705–1906 and the possibility of inward-directed photon emission.

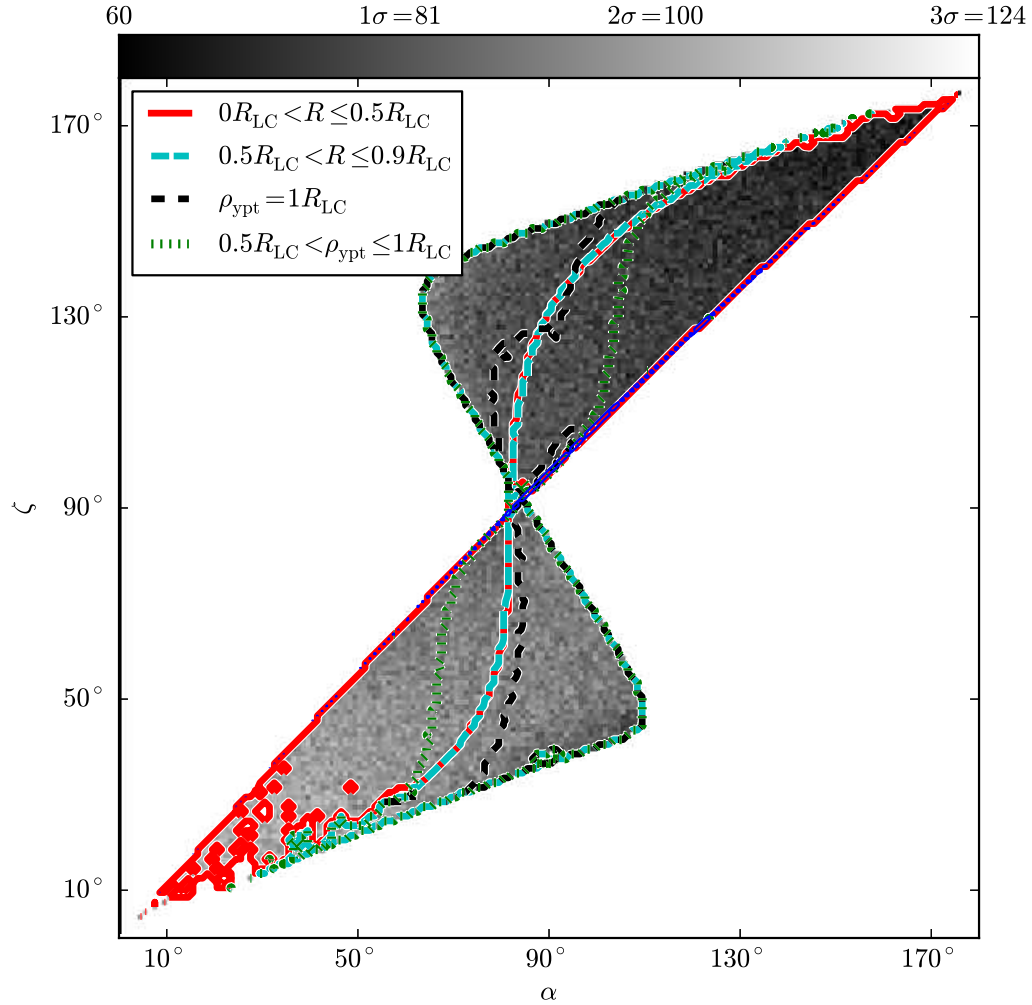


Figure 8.8: The χ^2 map in the α - ζ plane for fitting polarization sweep data from PSR J1705–1906 to a model with only outward-directed photon emission from two poles. The data fits reasonable well on a wide variety of α and ζ although large α and ζ are favored. Red contours are those fits within 3σ of the χ^2_{\min} with smaller altitudes of emission and cyan contours are those fits within 3σ of the χ^2_{\min} with larger altitudes of emission. Black contours are those fits within 3σ of the χ^2_{\min} and assume only the classical open field line emission. Green contours, on the other hand, allow for ρ_{ypt} as low as $0.5R_{\text{LC}}$.

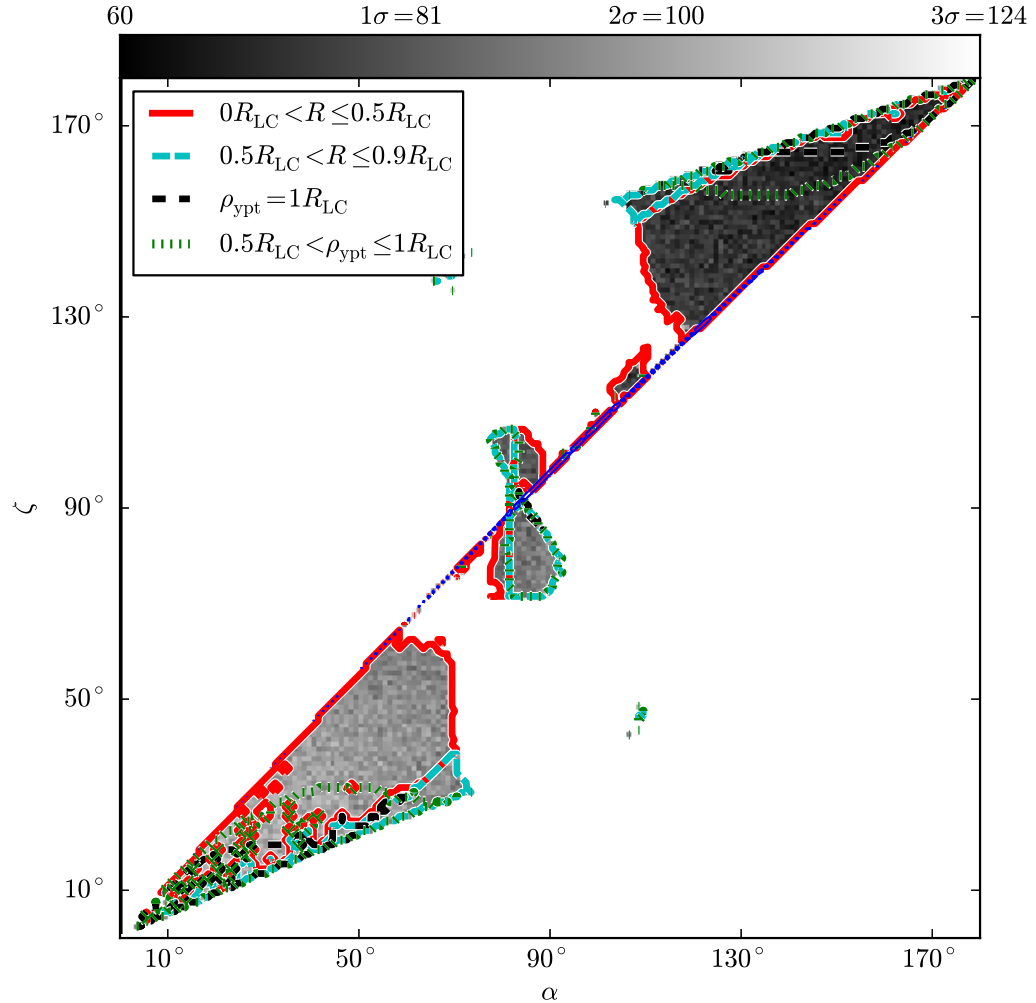


Figure 8.9: The χ^2 map in the α - ζ plane for fitting polarization sweep data from PSR J1705–1906 to a model with only outward-directed photon emission from a single pole. The data fits reasonable well on a wide variety of α and ζ although large α and ζ are favored. The region is also more constrained compared to the two-pole fit. Red contours are those fits within 3σ of the χ^2_{\min} with smaller altitudes of emission and cyan contours are those fits within 3σ of the χ^2_{\min} with larger altitudes of emission. Black contours are those fits within 3σ of the χ^2_{\min} and assume only the classical open field line emission. Green contours, on the other hand, allow for ρ_{ypt} as low as $0.5R_{\text{LC}}$.

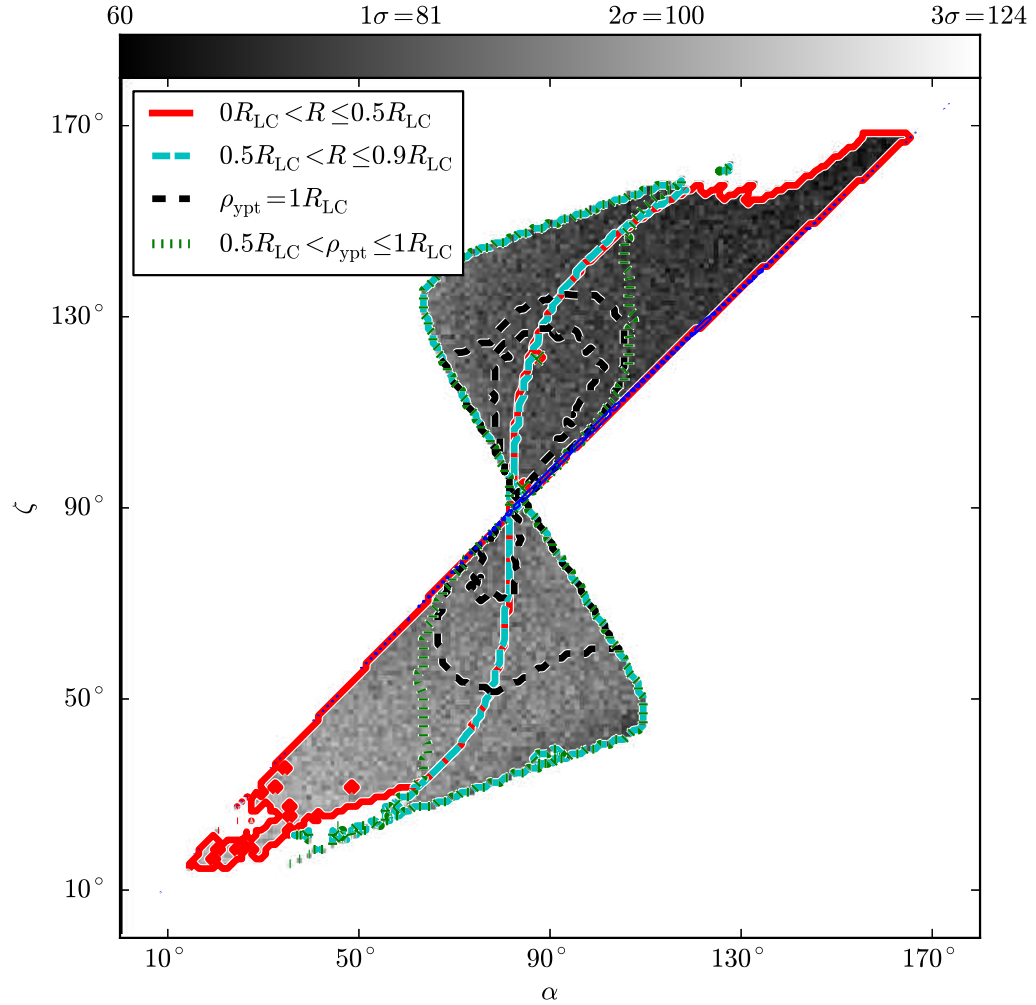


Figure 8.10: The χ^2 map in the α - ζ plane for fitting polarization sweep data from PSR J1705–1906 to a model with bidirectional photons from a single pole. Again, the data fits reasonable well on a wide variety of α and ζ . Large α and ζ are favored although not as large as those for the previous two fitting schemes (all outward-directed emission and single pole emission). Red contours are those fits within 3σ of the χ^2_{\min} with smaller altitudes of emission and cyan contours are those fits within 3σ of the χ^2_{\min} with larger altitudes of emission. Black contours are those fits within 3σ of the χ^2_{\min} and assume only the classical open field line emission. Green contours, on the other hand, allow for ρ_{ypt} as low as $0.5R_{LC}$.

Chapter 9

Outlook and Perspective

9.1 Next Steps

In this thesis, we brought a fresh perspective on the modeling of polarization of pulsars and questioned the current modeling assumptions. Although the work presented here is an improvement on our understanding of polarization, the need to go still further is continuously present. To understand all the data, the model needs a fundamental change. Although we did a fair job in explaining the polarization presented here, there is still a wealth of pulsar polarization data that has not been analyzed and will likely not be understood with the model revisions presented here alone.

The data that was available for analysis was limited. Often times, only a single frequency was available for analysis or the frequency with the most data or smallest error bars was analyzed. The frequency maps to the altitude (Cordes, 1978) such that different frequency originate at different altitudes. But this mapping was never tested due to inadequate data. As this is a multi-altitude model, having not applied this model to multi-frequency data within radio is a blatant shortcoming of this thesis. Further, the data was averaged over many periods, averaging out potentially interesting features. For instance the polarization of PSR J1057–5336 and PSR J1705–1906 have periodic nulling as discussed in Chapter 8 which is related to bidirectional emission; it is possible that analyzing the polarization data at different times in this cycle

may yield further insights. Arguably, a population study is needed to fully understand the nature of the polarization data from pulsars instead of focusing so much on individual sweeps.

Throughout the analysis, a single altitude of emission for each component of the polarization was used. The use of a single-altitude model cannot produce the sharp intensity peaks seen in the radio light curve. In the γ -ray emission, these sharp peaks in the intensity are called caustic peaks and are caused by overlapping of emission from a range of altitudes. In the outer gap model of γ -ray emission, these caustic peaks naturally arise from tracing emission from a single field line transversing through the magnetosphere, away from the pulsar. In the radio model, a single altitude assumption will not result in sharp peaks. A multiple-altitude model would not be hard to implement with emission for a single component originating over many altitudes but the prescription of such an assumption is unclear, thus we assumed the simplest model of just a single altitude.

Scattering effects sometimes appear in the polarization for pulsars where interstellar scattering is low. For instance, in the paper Karastergiou (2009), the author argues a combination of mode jumps and interstellar scattering can produce the complex polarization sweeps seen in the pulsar data. The pulsar polarization sweep that the author uses as the example to which this model is applicable is the data of PSR B0355+54 (PSR J0358+5413). In reality the scattering time constant for this pulsar is small compared to the amount of scattering needed to cause the amount of smoothing seen in the polarization sweep and particularly between the supposed mode jumps. We also saw more scattering in PSR J1420–6048 than could be explained by the given scattering time constant (Section 6.5.5). Although we did not formally report the fitting results of PSR J1600–3050 (Yan et al., 2011), in preliminary fitting, increasing the scattering time constant did improve the χ^2 significantly. But compared to the time constant needed (Cordes & Lazio, 2002) such fits were unphysical considering the interstellar scattering. This could indicate internal scattering in the magnetosphere (Braje & Romani, 2001) although such claims would require further investigation and another set of revisions to the current model.

Our model is based on the vacuum dipole. This model is acceptable at low altitude

but in some cases, high altitude limits in the fitting of the model to the data were explored. At high altitudes, plasma effects become important and a force-free model would be more appropriate.

Spitkovsky (2006) first used a time-dependent numerical code to calculate non-axisymmetric magnetic fields of a force-free model. The plasma filled, force-free models that require magnetohydrodynamic simulations are used for modeling light curves of high altitude emission in the γ -rays (Contopoulos & Kalapotharakos, 2010; Bai & Spitkovsky, 2010).

The time-dependent Maxwell equations are given as

$$\frac{\partial \mathbf{B}}{\partial t} = -\nabla \times \mathbf{E} \quad (9.1)$$

and

$$\frac{\partial \mathbf{E}}{\partial t} = -\nabla \times \mathbf{B} - 4\pi \mathbf{J}. \quad (9.2)$$

And with the force free assumption, we get

$$\mathbf{J} = \frac{1}{4\pi B^2} [(\nabla \cdot \mathbf{E}) \mathbf{E} \times \mathbf{B} + (\mathbf{B} \cdot \nabla \times \mathbf{B} - \mathbf{E} \cdot \nabla \times \mathbf{E}) \mathbf{B}]. \quad (9.3)$$

In the simulations, the above equations are integrated forward in time (Yee et al., 1966) until a steady state is obtained.

Harding et al. (2011) modeled γ -ray light curves using both vacuum and force-free simulations and compared to data. They found that data actually favored the vacuum models. Pulsar γ -ray emission in these models originate from outer gaps in the plasma-filled magnetosphere but this study suggests that field lines resemble more the vacuum models, hinting that the true solution needs properties of both.

Recent work by Kalapotharakos et al. (2012a,b, 2014) has explored models that bridge between vacuum and force-free magnetospheres using a finite conductivity. One way of obtaining such a model is by expressing \mathbf{J} as

$$\mathbf{J} = \frac{\nabla \cdot \mathbf{E}}{4\pi} \frac{\mathbf{E} \times \mathbf{B}}{B^2} + \sigma \mathbf{E}_{||}. \quad (9.4)$$

The conductivity σ can be varied from 0 to ∞ to range between the two standard magnetosphere approximations. The focus of these papers was again on γ -ray light curves. For instance, Kalapotharakos et al. (2012a) used this model to synthesize a population study of γ -ray pulsars. But such a model is appropriate for high-altitude radio emission. Producing polarization sweeps from such a model is sure to bring new insights to the magnetospheric emission far from the neutron star.

9.2 Summary of Conclusions

The current state-of-the-art, well-used analysis tool for understanding pulsar polarization is the RVM formulation. Using the simplest model for analysis is not intrinsically wrong. Indeed, when faced with a choice, the simplest model and assumptions often are the most likely to quickly and clearly give insights into a physical problem. Yet, in this thesis we have shown again and again the need for a better model to extract all of the information from the magnetic field lines of pulsars. In the end, the simple RVM does not work for complex polarization and for polarization from emission high in the magnetosphere. This polarization contains helpful information about the magnetic field lines which in turn tells us about the orientation of the pulsar and the region of emission. To extract this information, model assumptions must be revisited.

The limits of the analytical models of pulsar polarization including RVM and beyond were explored. Through comparison to numerical models, we conclude that the typical models are accurate for low altitude emission but approximations quickly break down at higher altitudes.

Next, in our analysis of complex polarization sweeps from high energy pulsars, we included relativistic and sweep-back effects (Romani & Watters, 2010), interstellar scattering (Cronyn, 1970), and orthogonal mode jumps (Backer et al., 1976). But more importantly, finite altitudes and multiple altitudes were used to explain a number of jumps in the polarization data. The possibility of bidirectional emission from a couple of promising pulsars was explored. Overall, there is evidence of high altitude emission in the radio from the practical application of the model to the available data.

This thesis work is significant because there are no widely-accepted alternatives

to simple analytical modeling of pulsar polarization position angles. The analytical model does not account for effects of the pulsar rotational motion. The simple analytic models work well for a large number of the known pulsars but fails for young pulsars and millisecond pulsars which often have complicated polarization. By making physically motivated models guided by the data, we have been working to increase the understanding of pulsars emission mechanism and geometry and to explain discrepancies between data and previous models.

This thesis has laid the groundwork for future endeavors in extracting knowledge from pulsar polarization data. It is not an end in itself but a step beyond the well-established but insufficient polarization models. Significant steps are still needed to fully understand the polarization but we have pushed the field in the right direction to further this pursuit.

Bibliography

- Abdo, A., Ackermann, M., Ajello, M., et al. 2010a, *The Astrophysical Journal Supplement Series*, 187, 460
- Abdo, A., Ajello, M., Allafort, A., et al. 2013, *The Astrophysical Journal Supplement Series*, 208, 17
- Abdo, A. A., Ajello, M., Antolini, E., et al. 2010b, *The Astrophysical Journal*, 720, 26
- Arons, J. 2006, in IAU Joint Discussion, Vol. 2, 39
- Baade, W., & Zwicky, F. 1934, *Proceedings of the National Academy of Sciences of the United States of America*, 20, 254
- Backer, D., Rankin, J. M., & Campbell, D. 1976, *Nature*, 263, 202
- Bai, X.-N., & Spitkovsky, A. 2010, *The Astrophysical Journal*, 715, 1282
- Becker, W. 2009, *Neutron stars and pulsars*, Vol. 357 (Springer)
- Blaskiewicz, M., Cordes, J., & Wasserman, I. 1991, *The Astrophysical Journal*, 370, 643
- Braje, T. M., & Romani, R. W. 2001, *The Astrophysical Journal*, 550, 392
- Breton, R. P., Kaspi, V. M., Kramer, M., et al. 2008, *Science*, 321, 104
- Burgay, M., D'Amico, N., Possenti, A., et al. 2003, *Nature*, 426, 531

- Colpi, M., Turolla, R., Zane, S., & Treves, A. 1998, *The Astrophysical Journal*, 501, 252
- Contopoulos, I., & Kalapotharakos, C. 2010, *Monthly Notices of the Royal Astronomical Society*, 404, 767
- Cordes, J. M. 1978, *The Astrophysical Journal*, 222, 1006
- Cordes, J. M., & Lazio, T. J. W. 2002, arXiv preprint astro-ph/0207156
- Craig, H. 2014, *The Astrophysical Journal*, 790, 102
- Craig, H., & Romani, R. W. 2012, *The Astrophysical Journal*, 755, 137
- Cronyn, W. M. 1970, *The Astrophysical Journal*, 161, 755
- Davis Jr, L., & Greenstein, J. L. 1951, *The Astrophysical Journal*, 114, 206
- Den Hartog, P. R., Kerr, M., Kuiper, L., et al. in prep.
- Dyks, J. 2008, *Monthly Notices of the Royal Astronomical Society*, 391, 859
- Dyks, J., Frkackowiak, M., Slowikowska, A., Rudak, B., & Zhang, B. 2005a, *The Astrophysical Journal*, 633, 1101
- Dyks, J., & Harding, A. K. 2004, *The Astrophysical Journal*, 614, 869
- Dyks, J., & Rudak, B. 2003, *The Astrophysical Journal*, 598, 1201
- . 2012, *Monthly Notices of the Royal Astronomical Society*, 420, 3403
- Dyks, J., Rudak, B., & Rankin, J. M. 2007, *Astronomy & Astrophysics*, 465, 981
- Dyks, J., Zhang, B., & Gil, J. 2005b, *The Astrophysical Journal Letters*, 626, L45
- Everett, J., & Weisberg, J. 2001, *The Astrophysical Journal*, 553, 341
- Ferdman, R., Stairs, I., Kramer, M., et al. 2013, *The Astrophysical Journal*, 767, 85

- Flannery, B. P., Press, W. H., Teukolsky, S. A., & Vetterling, W. 1992, Press Syndicate of the University of Cambridge, New York
- Foster, R., Ray, P., Cadwell, B., et al. 1997, in Bulletin of the American Astronomical Society, Vol. 29, 1392
- Gaensler, B. M., & Slane, P. O. 2006, *Annu. Rev. Astron. Astrophys.*, 44, 17
- Gil, J. 1985, *The Astrophysical Journal*, 299, 154
- Gil, J., Jessner, A., Kijak, J., et al. 1994, *Astronomy and Astrophysics*, 282, 45
- Gold, T. 1968, *Nature*, 218, 731
- Gould, D., & Lyne, A. 1998, *Monthly Notices of the Royal Astronomical Society*, 301, 235
- Guillemot, L., Kramer, M., Johnson, T., et al. 2013, *The Astrophysical Journal*, 768, 169
- Hall, J. S. 1949, *Science*, 109, 166
- Harding, A. K., DeCesar, M. E., Miller, M. C., Kalapotharakos, C., & Contopoulos, I. 2011, arXiv preprint arXiv:1111.0828
- Harding, A. K., & Muslimov, A. G. 2011, *The Astrophysical Journal*, 743, 181
- Hessels, J. W., Ransom, S. M., Stairs, I. H., et al. 2006, *Science*, 311, 1901
- Hibschman, J. A., & Arons, J. 2001, *The Astrophysical Journal*, 546, 382
- Hiltner, W. 1949, *Science*, 109, 165
- Hobbs, G., Lyne, A., Kramer, M., Martin, C., & Jordan, C. 2004, *Monthly Notices of the Royal Astronomical Society*, 353, 1311
- Hou, X., Smith, D., Guillemot, L., et al. 2014, *Astronomy & Astrophysics*, 570, A44

- Johnston, S., & Weisberg, J. M. 2006, Monthly Notices of the Royal Astronomical Society, 368, 1856
- Kaburaki, O. 1980, Astrophysics and Space Science, 67, 3
- Kalapotharakos, C., Harding, A. K., & Kazanas, D. 2014, The Astrophysical Journal Letters, 793, 97
- Kalapotharakos, C., Harding, A. K., Kazanas, D., & Contopoulos, I. 2012a, The Astrophysical Journal Letters, 754, L1
- Kalapotharakos, C., Kazanas, D., Harding, A., & Contopoulos, I. 2012b, The Astrophysical Journal, 749, 2
- Karastergiou, A. 2009, Monthly Notices of the Royal Astronomical Society: Letters, 392, L60
- Karastergiou, A., & Johnston, S. 2007, Monthly Notices of the Royal Astronomical Society, 380, 1678
- Karastergiou, A., Johnston, S., & Manchester, R. 2005, Monthly Notices of the Royal Astronomical Society, 359, 481
- Keith, M., Johnston, S., Bailes, M., et al. 2012, Monthly Notices of the Royal Astronomical Society, 419, 1752
- Kerr, M., Camilo, F., Johnson, T., et al. 2012, The Astrophysical Journal Letters, 748, L2
- Kraus, J. D. 1986, Cygnus-Quasar Books, Powell, Ohio, 7
- Lang, K. R. 1971, Pulse broadening due to angular scattering in the interstellar medium., Tech. rep., Cornell-Sydney Univ. Astronomy Center, Arecibo, Puerto Rico
- Li, X., & Han, J. 2003, Astronomy & Astrophysics, 410, 253

- Lyne, A., & Manchester, R. 1988, Monthly Notices of the Royal Astronomical Society, 234, 477
- Lyne, A., Burgay, M., Kramer, M., et al. 2004, Science, 303, 1153
- Lyne, A. G. 2006, Pulsar Astronomy, Vol. 38 (Cambridge University Press)
- McLaughlin, M. A., & Rankin, J. M. 2004, Monthly Notices of the Royal Astronomical Society, 351, 808
- Melrose, D., & Yuen, R. 2012, The Astrophysical Journal, 745, 169
- Moffett, D. A., & Hankins, T. H. 1996, The Astrophysical Journal, 468, 779
- Ng, C.-Y., & Romani, R. W. 2004, The Astrophysical Journal, 601, 479
- . 2008, The Astrophysical Journal, 673, 411
- Ng, C.-Y., Romani, R. W., Brisken, W. F., Chatterjee, S., & Kramer, M. 2007, The Astrophysical Journal, 654, 487
- Pacini, F. 1967
- . 1968, Nature, 219, 145
- Parent, D., Kerr, M., Den Hartog, P., et al. 2011, The Astrophysical Journal, 743, 170
- Pelling, R., Paciesas, W., Peterson, L. E., et al. 1987, The Astrophysical Journal, 319, 416
- Phillips, J. 1990, The Astrophysical Journal, 361, L57
- Podsiadlowski, P., Dewi, J., Lesaffre, P., et al. 2005, Monthly Notices of the Royal Astronomical Society, 361, 1243
- Radhakrishnan, V., & Cooke, D. 1969, Astrophysical Letters, 3, 225

- Ray, P., Cadwell, B., Lazio, T., et al. 1999, in Bulletin of the American Astronomical Society, Vol. 31, 903
- Roberts, M. S., Romani, R. W., & Johnston, S. 2001, The Astrophysical Journal Letters, 561, L187
- Rohlfs, K., & Wilson, T. 2000, Tools of Radio Astronomy (Astronomy and astrophysics library)
- Romani, R., Kerr, M., Craig, H., et al. 2011, The Astrophysical Journal, 738, 114
- Romani, R. W., Filippenko, A. V., Silverman, J. M., et al. 2012, The Astrophysical Journal Letters, 760, L36
- Romani, R. W., & Ng, C.-Y. 2003, The Astrophysical Journal Letters, 585, L41
- Romani, R. W., & Watters, K. P. 2010, The Astrophysical Journal, 714, 810
- Spitkovsky, A. 2006, The Astrophysical Journal Letters, 648, L51
- Stinebring, D., Cordes, J., Rankin, J., Weisberg, J., & Boriakoff, V. 1984, The Astrophysical Journal Supplement Series, 55, 247
- Taylor, J. H., & Cordes, J. 1993, The Astrophysical Journal, 411, 674
- Theureau, G., Parent, D., Cognard, I., et al. 2011, Astronomy and Astrophysics-Les Ulis, 525, 848
- Van Etten, A. A. 2012, PhD thesis, Stanford University
- Watters, K. P., & Romani, R. W. 2011, *Astrophys.J.*, 727, 123
- Weltevrede, P., Johnston, S., & Espinoza, C. M. 2011, Monthly Notices of the Royal Astronomical Society, 411, 1917
- Weltevrede, P., & Wright, G. 2009, Monthly Notices of the Royal Astronomical Society, 395, 2117

- Weltevrede, P., Wright, G., & Johnston, S. 2012a, in Astronomical Society of the Pacific Conference Series, Vol. 466, 47
- Weltevrede, P., Wright, G., & Johnston, S. 2012b, Monthly Notices of the Royal Astronomical Society, 424, 843
- Weltevrede, P., Wright, G., & Stappers, B. 2007, Astronomy & Astrophysics, 467, 1163
- Weltevrede, P., Abdo, A. A., Ackermann, M., et al. 2010a, The Astrophysical Journal, 708, 1426
- Weltevrede, P., Johnston, S., Manchester, R., et al. 2010b, Publications of the Astronomical Society of Australia, 27, 64
- Williamson, I. P. 1972, Monthly Notices of the Royal Astronomical Society, 157, 55
- . 1973, Monthly Notices of the Royal Astronomical Society, 163, 345
- Wright, G. 2003, Monthly Notices of the Royal Astronomical Society, 344, 1041
- Wright, G. A. 2004, Monthly Notices of the Royal Astronomical Society, 351, 813
- Yan, W., Manchester, R., van Straten, W., et al. 2011, Monthly Notices of the Royal Astronomical Society, 414, 2087
- Yee, K. S., et al. 1966, IEEE Trans. Antennas Propag, 14, 302